Commissioning of an intense broad band source of terahertz radiation and terahertz exposure of biological molecules

Thesis submitted in accordance with the requirements of the University of Liverpool for the degree of Doctor in Philosophy

by

Gareth Michael Holder

Department of Physics

September 2011

To Steve, Michele and Samantha

Control the controllables

Abstract

This thesis discusses the commissioning of the most intense broadband source of terahertz (THz) radiation in Europe, at ALICE (Accelerators and Lasers In Combined Experiments), and the first to be equipped with a Tissue Culture Facility (TCF). The commissioning of the THz transport system is discussed in a chronological manner with experimental results compared with theoretical models to improve understanding of the ALICE accelerator and transport the THz radiation to the TCF. This was first achieved in March 2011. The studies explain some of the complex issues that had to be resolved and the development of a new front end extraction system to maximize the transport efficiency of the beam line. The THz beam line at ALICE has the huge potential to test the long debated and very controversial Frohlich hypothesis concerning the mechanism of biological organisation. ALICE's time structure results in high peak power, low average power THz radiation.

One of the initial studies on cells performed at the ALICE THz beam line is discussed with a number of subsidiary studies performed to clarify the results. A study of THz exposure of Zebra fish embryos provides very interesting results, however at present, it is not possible to state whether the THz radiation has an effect on the growth of Zebra fish embryos due to a number of complications, which are all discussed. The results suggest a possible new hypothesis, where the effects of THz radiation are dependent on whether a biological system enters an arrested state. In this state, the embryo has no ability to fix any damages caused by the THz radiation.

The final section of this thesis covers a study of conformational changes of a biological sugar, heparin. Heparin is a structural analogue for Heparan Sulfate which is the most abundant molecule found on a cell surface and plays a crucial role in all reactions and general structure of the extra cellular matrix (ECM). The Reflection Anisotropy Spectroscopy studies suggest that some of the cation forms of heparin dry into a film with an anisotropic direction. The THz radiation results, although not thoroughly understood suggest that THz can distinguish between heparin cation forms due to their differences in conformation. This technique has the long term

potential to monitor conformational change and could contribute to the understanding their reaction with other ECM molecules.

Acknowledgements

I would firstly like to thank Prof. Peter Weightman for the opportunity to work in his research group. His enthusiasm and passion are contagious and his support and compelling stories will never be forgotten. He is an inspiration.

I must also thank Dr. Mark Surman, of Daresbury, whose support and friendship have been key in surviving the late nights and long shifts at ALICE. Throughout the last 4 years we have shared frustrations and celebrations and it has been a thoroughly enjoyable time.

There are also a number of other key people, that without them, the successful work at ALICE would not have been possible, Paul Harrison, John Kervin and all the ASTEC staff at Daresbury including Dr. Yuri Saveliev, Dr. Stephen Hill, Mark Roper, Dr. Peter Williams and Dr. Susan Smith. Mark Roper performed the beam propagation models, and Peter Williams worked on the bunch compression model discussed in the thesis. I am grateful to them all and it has been fantastic to work with such a talented group of people.

I am also grateful for the knowledge and skill of Dr. Ed Yates, Dr. Caroline Smith, Dr. Rachel Williams, Dr. Amy Schofield, and Dr. Trevor Farrell. I would also like to thank Dr. Catherine Turner who maintained and monitored the Zebra fish embryos. I have been fortunate to work with some fantastic fellow PhD students who must also be thanked for support both in work and socially, Dr. Nick Almond, Dr. Andrew Bowfield, Dr. Chris Mansley, James Convery and Elizabeth Barritt. A special thanks to Andrew who shared some fun times at ANKA, from experiments to long table tennis sessions.

Some of the most important people have been friends that have helped me turn off and recharge batteries at times, or just listen to my frustrations. Neil Jones, Peter Nugent, Andrew Rose and John McCall, whether it is through nights in the pub talking about bands and jeans, or soul searching football discussion, I am very grateful. I must also thank the Xavs, a great bunch of lads, where the game of cricket is only bettered by the social nights afterwards. The support shown by all through a difficult time at work and personally has been very overwhelming and an enormous help.

The challenges of the last four years would have been infinitely more difficult, were it not for a very special person, Samantha Ingham. Her love, patience and support have been endless, during the good and bad times, both through work and personally. I am endlessly grateful to her. As one adventure ends, another begins.

Finally, none of this work would have been possible, nor would I have even been in the position to take on such an opportunity were it not for my parents and family. Their support and unquestioned confidence in my ability has been vital. I am so grateful to my mum and dad, my mum, a best friend and the bravest lady I know, and my dad, driven, successful, supportive and my hero. I owe so much to them both.

Acronyms

Angular dependant Reflection Anisotropy Spectroscopy	**ADRAS**
Accelerators and lasers in Combined Experiments	**ALICE**
Angstrom Source Karslruhe	**ANKA**
Backward Wave Oscillator	**BWO**
Circular Dichroism	**CD**
Continuous Wave	**CW**
Density of States	**DOS**
Direct Current	**DC**
Difference Frequency Generation	**DFG**
Difference Mixing Generation	**DMG**
Dioxyribonucleic Acid	**DNA**
Extra Cellular Matrix	**ECM**
Enzyme Linked Immunosorbent Assay	**ELISA**
Electro Optical Rectification	**EOR**
Electron Paramagnetic Resonance	**EPR**
Energy Recovery Linac	**ERL**
Energy Recovery Linac Prototype	**ERLP**
Fluorescence Resonance Energy Transfer	**FRET**
Full Width Half Maximum	**FWHM**
Fourier Transform Infrared	**FTIR**
Glycoamunoglycans	**GAG's**
Helium Neon	**HeNe**
Hours Past Fertilization	**hpf**
High performance liquid chromatography	**HPLC**
Heparan Sulfate	**HS**
Infrared	**IR**
Jefferson Laboratory	**JLAB**
New Light Source	**NLS**
Nuclear Magnetic Resonance	**NMR**
Optical Rotary Dispersion	**ORD**
Polyethylene	**PE**
Photoelestic Modulator	**PEM**

Photoelectron Spectroscopy	**PES**
Pop in Dump	**PID**
Polarising Light Microscopy	**PLM**
Quantum Cascade Lasers	**QCL**
Quartz Crystal Microbalance Dissipation	**QCM-D**
Reflection Anisotropy	**RA**
Reflection Anisotropy Spectroscopy	**RAS**
Radio Frequency	**RF**
Ribonucleic Acid	**RNA**
Root Mean Squared	**RMS**
Synchrotron Radiation Circular Dichroism	**SRCD**
Synchrotron Radiation Source	**SRS**
Synchrotron Radiation Wave	**SRW**
Switch Mirror	**SWM**
Tissue Culture Facility	**TCF**
Time Domain Spectroscopy	**TDS**
Terahertz	**THz**
Thermolumenescent Detectors	**TLD's**
Polymethylpentene	**TPM/TPX**
Ultra High Vacuum	**UHV**
Ultra Violet	**UV**
Ultra Violet visible spectroscopy	**UV-Vis**
X-ray Photoelectron Spectroscopy	**XPS**

Contents

Chapter 1. Introduction

There follows a brief introduction as to the importance and aims of the research undertaken along with its relevance within a wider context.

In September 1994 a class entered the physics class room for the last lesson of their first day at secondary school. Written on the black board was "Physics is everything and everything is physics." The class was asked by their teacher to write down this phrase on the inside cover of their new physics exercise books before then being asked to come up with examples that might prove this wrong. Many hands went up, and in turn, despite the students best efforts to get one over their new teacher and show off to their new classmates, were proven to be wrong. Each proposal was rejected by the teacher who managed to explain in a way all in the class understood how physics was an important part of whatever was proposed. I don't remember much else from that specific lesson, but I will always remember that introduction to physics and its role in everything that surrounds us.

The question "how" is one of the most fascinating questions we can ask. To answer it requires a great understanding and vast knowledge of the area. Asking "how" always results in the most interesting answers and only when you can answer this question confidently do you truely understand what it is you are talking about. The other remarkable question is simply "why". It is these questions that force the requirement for research in science.

With the current economic climate, scientists face great and difficult challenges. Research that aims to answer the most important questions in security, health, climate change, nanotechnology and energy technologies are likely to see the greater success in grant applications. These areas of interest have considerable political significance, security, health, climate change and energy technologies carry great public interest and with that added pressure for successful research to produce answers.

Terahertz (THz) radiation has the potential to provide useful information in a number of these important scientific areas. It has great potential security benefits due to its properties as it can penetrate through many opaque materials *e.g.* clothing for use in full body scanners to detect hidden weapons and dangerous objects. THz radiation is also energy equivalent to the free energy avaliable at room temperature, with many theoretical studies debating the potential importance of vibration modes, in the THz range, in biological organisation. It has however been difficult to test these long argued theories due to the difficulty in generating high peak power THz radiation. If THz vibration modes do play a role in biological organisation it could reveal a large amount of information on DNA synthesis and replication, cell-cell

interactions, cancer development and the secrets that drive photosynthesis, the most efficient method to turn sun light into usable energy.

The questions of why DNA replicates in such a manner, or why molecules align in such a way is one that requires an extensive study? A lot is already known about these systems, however the ultimate questions of "how" and "why" still need further research to allow a confident and assured answer to be provided. The final few paragraphs of Newton's "Principia" are shown in figure 1.1.

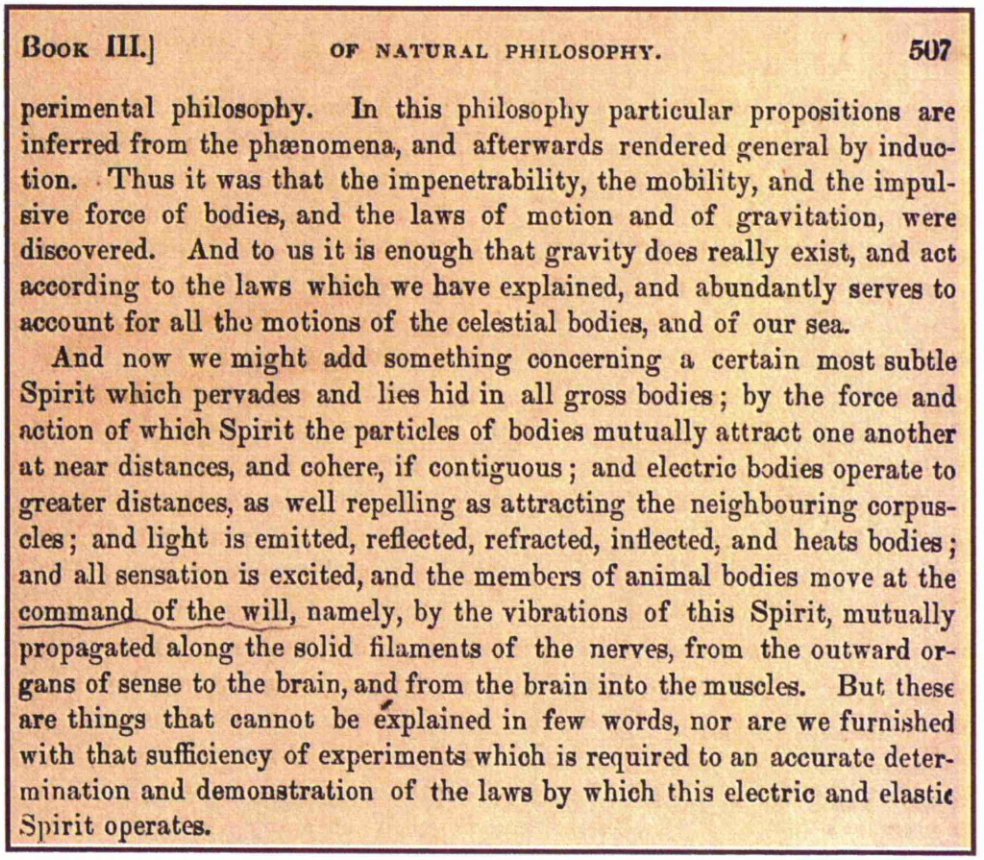

BOOK III.] OF NATURAL PHILOSOPHY. 507

perimental philosophy. In this philosophy particular propositions are inferred from the phænomena, and afterwards rendered general by induction. Thus it was that the impenetrability, the mobility, and the impulsive force of bodies, and the laws of motion and of gravitation, were discovered. And to us it is enough that gravity does really exist, and act according to the laws which we have explained, and abundantly serves to account for all the motions of the celestial bodies, and of our sea.

And now we might add something concerning a certain most subtle Spirit which pervades and lies hid in all gross bodies; by the force and action of which Spirit the particles of bodies mutually attract one another at near distances, and cohere, if contiguous; and electric bodies operate to greater distances, as well repelling as attracting the neighbouring corpuscles; and light is emitted, reflected, refracted, inflected, and heats bodies; and all sensation is excited, and the members of animal bodies move at the command of the will, namely, by the vibrations of this Spirit, mutually propagated along the solid filaments of the nerves, from the outward organs of sense to the brain, and from the brain into the muscles. But these are things that cannot be explained in few words, nor are we furnished with that sufficiency of experiments which is required to an accurate determination and demonstration of the laws by which this electric and elastic Spirit operates.

Figure 1.1 Final few paragraphs of Newton's Principia

In a presentation by Martyn Chamberlain [1] he suggested that the unexplainable "spirit" Newton refers to, which is involved in everything that makes bodies, whether it's the mutually attraction of particles at near distances or the materials vibrational properties, and how these vibrations go from the brain to muscles could well be THz vibrational modes? A long range mode, that could allow for long range ordering? This elixir of life that without it, life as we know it would not be able to exist?

The complexity of biological systems is remarkable, yet within this complexity is near perfect organisation. The level of organisation spans a number of

length scales with short and long range signaling. One example of the great level of complexity with a great level of organization are proteins. Proteins are a vital part of the living organism. There are more than 100,000 proteins in the human body constructed of only 20 different amino acids, which all have the same basic structure. The sequence of amino acids determines the primary structure of a protein, with a protein of 300 amino acids being produced in just over a minute. The linear protein then becomes coiled and folds as interactions between amino acids along the protein chain producing secondary and tertiary structures that contain the proteins functional regions. The proteins structure is vital to its function. With proteins having so many functions within the human body the efficiency and accuracy in protein building is vital. This all takes place numerous times a day in every cell and on very small time scales. Understanding this tertiary structure is not possible from knowledge of the amino acid sequence and therefore these folds and alterations, which involve hydrogen (H)-bonding, in 3D structure needs further research to understand them. A further remarkable trait of proteins is their ability to find the right conformation to ensure they react in the required way. If this process was not driven by some force, which is yet unknown, it would have to be random. This is simply not possible, as described by Cyrus Levinthal in 1969 when he stated that even with a protein consisting of only 100 amino acids, and only allowing for each unit to flex in one of two different conformations, the protein could theoretically adopt up to 10^{30} different orientations. He suggested that even if the protein could attempt 100 billion different conformations a second, it would still require 100 billion years to try all the possibilities [2].

Consequently protein folding must be driven by some kind of force, it is not a chemical interaction with the breaking or forming of bonds, the energies involved must be at available room temperature (free energy at room temperature = 6 THz) and it must affect long range ordering. Therefore it is possible that THz radiation could probe these long-range modes and present an insight to the complexity behind proteins and molecular organization. There are limitations with THz radiation that must be overcome, one example of this is that THz radiation is highly absorbed by water, and this therefore results in difficulties performing succesful biological studies. The high peak power THz radiation generated at ALICE has the potential to limit the affect of THz radiation attenuation of water, however the presence of water will still affect experimental design. The timing structure of ALICE will also allow

experiments to be performed without potential heating affects from the THz radiation. It is important to ensure any affects are caused through THz radiation, rather than thermal modes. Thermal modes would be expected to increase entropy, rather than provide modes of vibration for ordering and organization. A further limitation of THz radiation is any spectral information is likely to feature broad features due to the high number of IR active modes in this region of the spectrum. For many years there has been extensive debate over the potential in the THz region, however it is only now that such a controversial subject in physics and biology can finally be probed. It is therefore considered that THz radiation has the potential to enhance understanding in a number of scientific areas providing research with a global impact.

1.1 Thesis Aims

This thesis discusses work to commision an intense broad band THz radiation source at the ALICE accelerator in Daresbury. This is the only THz radiation beam line of its type to have a Tissue Culture Facility (TCF) built to explore the affects of THz radiation on living cells cultivated in their ideal conditions. THz radiation is introduced and the potential of THz radiation studies in biology are discussed. This is followed by initial THz exposure experiments on an ideal biological cell system performed at ALICE. The final section presents a study performed to improve understanding on a crucial molecule in the extra cellular matrix including THz spectroscopy.

1.2 Thesis Layout

Chapter 2 – Experimental Techniques and Equipment

The detectors used in the commissioning of the THz radiation beam line at ALICE are discussed. The chapter also includes an overview of the techniques used in the study of the conformation of Heparin.

Chapter 3 – THz Radiation and its Importance in Biology

THz radiation is introduced with an overview of a number of techniques that have been used in the past for THz radiation studies leading to those that are currently used and those that may provide a future for THz research of biological molecules.

Chapter 4 – Commissioning of the THz Beam Line at ALICE

An overview of the ALICE accelerator is presented including a number of the principles behind its running and the generation of THz radiation. The THz beam line is described and the successful commissioning is reviewed in a chronological order leading to the successful transmission of THz radiation to the diagnostics room and TCF.

Chapter 5 – Initial THz Exposure Experiments on Zebra Fish

One of the initial cell studies performed at ALICE is explained. A number of the issues and difficulties with performing the experiments in the accelerator hall are discussed with a number of interesting conclusions gained from a thorough experimental programme on a model cell system.

Chapter 6 – Conformational Study of Heparin

A comprehensive study of heparin, a model compound for heparan sulfate, which is found in the extracellular matrix (ECM). Heparan sulfates interact with proteins and are the most dominant molecule on the cell surface. Heparin shares similar characteristics and is far more abundant making it a suitable structural analogue. The aim is to determine whether the molecules have any inherent propensity to form self-ordered structures and the effects that changes in cation binding cause. A number of complementary spectroscopic techniques are employed.

Chapter 7 – Conclusions

The section provides a brief summary of the work discussed in this thesis as well as suggestions for future work in this area.

1.3 References

[1] M. Chamberlain. Looking at Biological systems with Terahertz Radiation, *NPL Terahertz Workshop*, Durham University, (2009, 17th December).

[2] J. Pietzsch, *The importance of protein folding.* "online" (2004) http://www.nature.com/horizon/proteinfolding/background/importance.html (Assessed: 13/11/2010).

Chapter 2. Experimental and Detectors

The aim of this chapter is to present the detectors and experimental techniques used in this thesis.

Three types of detector were used during the commissioning of the THz beamline at ALICE; a liquid helium filled bolometer, a Golay cell based power meter (large area detector) and a number of different pyroelectric detectors. The bolometer was situated in the diagnostics room on the Martin Pupplet FTIR (Fourrier Transform Infrared) spectrometer. The large area detector and the pyroelectric detectors were mobile and used in every step of the commissioning process.

2.1 Detectors

2.1.1 Liquid Helium Filled Bolometer

A bolometer can be used at submillimeter wavelengths and is the most sensitive detector available. It is made of an absorbing element connected to a heat sink, which rises in temperature when exposed to radiation, with the temperature relative to the heat sink being monitored. It requires a modulated source and the detectors have varying response times and the ability to return back to a normal temperature. The sensitivity is achieved by cooling the bolometer with liquid helium while the vessel is held under pressure. The great advantage, its sensitivity, comes at a price, the bolometer is immobile and unsuitable for spatial mapping of the output from the diamond window.

Figure 2.1. A liquid helium filled bolometer [1].

The bolometer requires regular maintenance. It is battery powered, so required battery changes every few days. The liquid helium must be replenished every 24 hours, with the liquid nitrogen refreshed every 12 hours. The initial set up can take up to 12 hours.

2.1.2 The Golay Cell (Large Area Detector)

The power meter or large area detector is a Golay cell. A Golay cell detector is a photo-acoustic detector. It contains a sealed gas filled absorbing chamber with a thin absorbing film that absorbs the radiation, warming the gas in the chamber, and therefore changing the pressure that is monitored by a microphone section. The signal is then sent through a preamplifier to an oscilloscope. The power meter used in the ALICE study has a large active area. This is an important property as it is able to capture all the radiation emitted from the diamond window, or at the end of the copper pipe. It is sensitive to the energy per pulse train, and can be calibrated by inputting a known electrical signal into the film and measuring the output signal. It is also important to take into account the transmission of the chamber window. The calibration indicated that for every 1 μJ of radiation absorbed results in a 1 mV signal. This allows for a measureable value that can be compared with the theoretical values based on the simulation discussed in chapter 4. Figure 2.2 shows the power meter used in the ALICE studies.

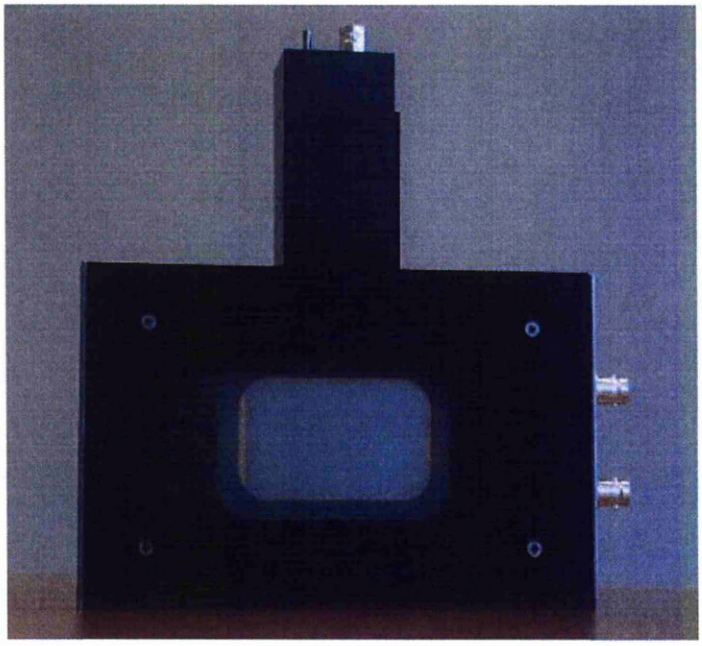

Figure 2.2. Picture of the Golay cell used at ALICE with the large active area clearly shown in the centre of the mirror. The active area is 60x40mm. [2].

2.1.3 Pyroelectric Detector

A pyroelectric detector is very sensitive and can operate at room temperature. It has a good broad flat spectral response across most of the electromagnetic spectrum. A pyroelectric detector, although not as sensitive as a Golay cell, it has a far quicker

response time and therefore can be used in a large range of operating temperatures. It is also easy to transport as it is small in size and does not require an AC power supply, since it can run on batteries and can also be used with or without a window [3].

The detector has a thin $LiTaO_3$ ferroelecric crystal which is coupled with conductive electrodes into a circuit. The crystal produces a thermal effect where its instantaneous polarization is a function of the rate of temperature change within the crystal. Therefore when radiation is absorbed by the crystal the temperature changes, and this can be calibrated to give a measure of power received [3]. Figure 2.3 shows the pyroelectric detector used in the ALICE study, the casing and the detector element depressed inside the casing can be seen.

Figure 2.3. The pyroelectric detector showing the active detector element inside the detector casing. Size ~ 200x120mm.

Another advantage of the use of the pyroelectric detector, in this study, is the ability to combine it with a variety of filters that are available at Daresbury laboratory due to the aperture size. Figure 2.4 shows the polythene window adaption to the pyroelectric detector, allowing a filter to be placed between the polythene window and the detector element, the filter is shown, half in the holder to distinguish it from the assembly.

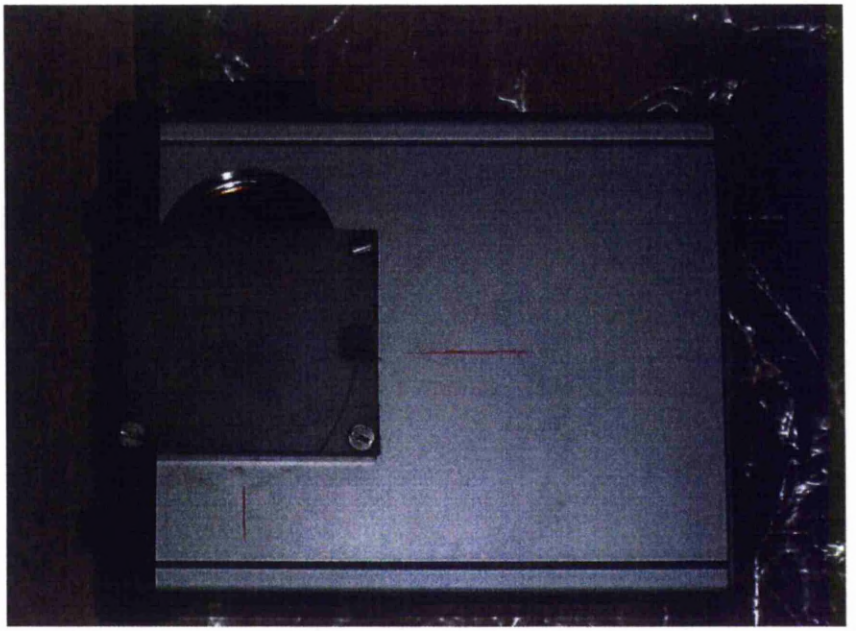

Figure 2.4. The pyroelectric detector with a polythene window and a filter set behind it.

2.1.4 Microwave Sources

There are two microwave sources, both emit 140 GHz, at the University of Liverpool that are used for testing detectors and components. These are, a backward wave oscillator CW (continuous wave) source (in the radio frequency [RF] sense), that has a continuous pulse at ~ 37 mW and a pulsed source with a pulse height power of 3 W lasting 80 ns. The pulse rate can be varied from single pulse to 50 kHz.

2.2 Fourier Transform Infrared Spectroscopy (FTIR)

Infrared Spectroscopy is a commonly used technique for identifying the chemical groups of a compound. When IR (infrared) light interacts with a functional group in a sample it causes the bond to either stretch, contract and/or bend. This gives rise to an absorption spectrum for each functional group independent of changes in temperature, pressure, sampling or change in compound structure, *e.g.* a carbonyl stretch will be seen at the same frequency in the spectrum whether the compound is a ketone or an aldehyde [4].

The region of 4000-1300 cm^{-1} is of great use to scientists as many of the chemical functional groups have characteristic peaks in this range. The spectral range below 1300 cm^{-1} is described as the "fingerprint region" (1300-900 cm^{-1}). It is a very difficult region to interpret due to the complex interaction of vibrational modes that take place at these wavelengths. However every organic compound has its own unique absorption spectra in this region, hence "fingerprint".

In FTIR the infrared spectra are obtained in the form of an interferogram which contains information on all the IR frequencies within the source. The IR spectrum is then obtained from a Fourier Transform of the interferogram converting the results in the time domain into a spectrum in the frequency domain.

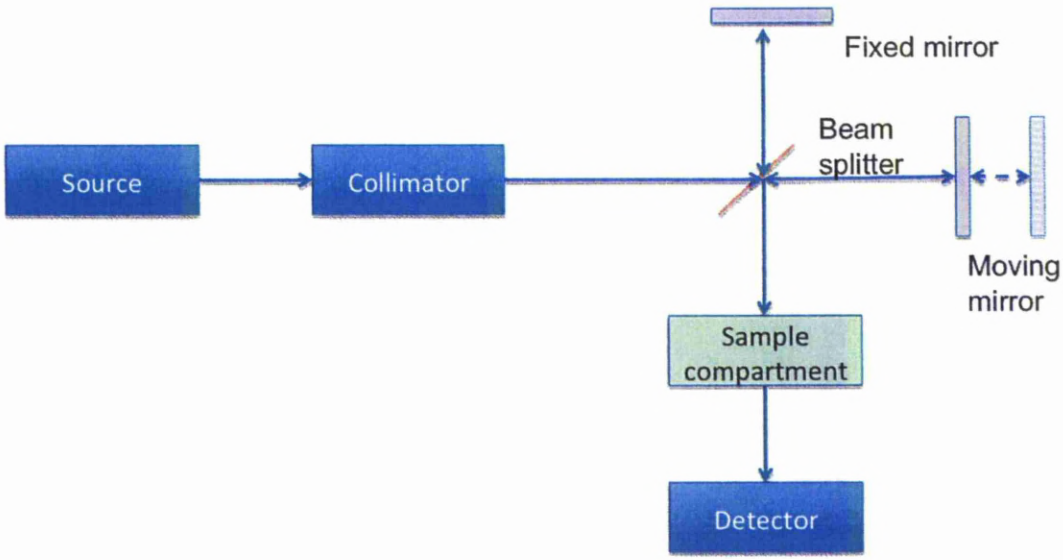

Figure 2.5. A schematic of an interferometer, adapted from [5].

Figure 2.5 shows a schematic of how a Michelson interferometer works, a broad source of collimated light enters the interferometer and passes through a beam splitter. This reflects 50 % of the light towards a mirror in a fixed position, while the other 50 % is directed to a mirror that can move towards and away from the beamsplitter. The two beams of light reflect off their respective mirrors and are recombined as they return to the beamsplitter producing an interferogram, when the two beams "interfere" with each other. The distance of the path for the beam travelling to the fixed mirror does not change, however the other path is constantly changing, due to the movement of the mirror. The interferogram then passes through a sample compartment where absorption/transmission or reflectance measurements can be performed before the light is directed to a detector. A Fourier transform of the detected interferogram results in a frequency spectrum of the sample [5]. The Martin Pupplett interferometer based at ALICE has a similar setup as to that shown in figure 2.5, however the beam splitter is a wire grid polarizer and the mirrors are roof top mirrors which change the polarization of the light by 90 degrees.

FTIR differs over dispersive methods in that (1) no slits are required, so the throughput (*i.e.* intensity of light transmitted to the detector) is higher and the signal to noise at the detector is increased and (2) all the wavelengths are sampled simultaneously. Lengthening the distance of travel of the scanning mirror increases the spectral resolution. To improve the spectral resolution in a dispersive method requires larger and larger sized grating. A FTIR scan can be performed in under a second, however, the results are usually generated from a number of scans, and an average taken. For example at ANKA (Angstrom Source Karslruhe) the results (discussed in chapter 6) were obtained from an average of 256 scans taken over a 5 minute period.

2.3 Reflection Anisotropy Spectroscopy (RAS)

Reflection Anisotropy Spectroscopy (RAS) is an optical probe that was first developed by Aspnes and co-workers [6,7] to study the properties of semiconductor surfaces and monitor semiconductor growth. To date, the majority of the published work involving RAS has used the technique to monitor the anisotropy of single crystal surfaces. They have been performed under UHV conditions and the results have been combined with surface techniques including, low energy electron diffraction (LEED), scanning tunnelling microscopy (STM) and X-ray photoelectron spectroscopy (XPS), allowing the ability to understand the atomic and electronic structure and morphology of the surfaces probed. However the Liverpool group have monitored the changes in anisotropy of biological molecules at surfaces. Understanding how biological molecules align is very important, and this is discussed further in the heparin chapter (chapter 6). The technique does have limitations however, it does not provide any structural information of the molecule, and the interpretation of the spectra requires a good understanding of the molecule or system being analysed.

While RAS has some similarities to spectroscopic ellipsometry it differs in recording the intensity of near normal incident light at near normal reflection from a surface and also employs a photoelastic modulator (PEM). Since it is an optical probe, it has a number of advantages over other surface science techniques. These include, its ability to be used in both Ultra High Vacuum (UHV) and a variety of ambient conditions, and it is non-destructive to the samples it analyses.

Optical probes are generally strongly influenced by the optical response of the bulk specimen due to the light penetrating into many atomic layers of the material. RAS is a microscopic probe of macroscopic anisotropy. The signal arises from optical transitions on a local atomic or molecular scale but they only add to give a net signal if there is macroscopic anisotropy. The geometry of the RAS experiment is chosen so as to yield an optical probe of a surface provided that the structure of the specimen satisfies certain conditions. For a cubic structure the RAS contribution from the bulk cancels by symmetry and the RAS will yield the optical response of the surface provided the surface has a C_2 axis of symmetry. For a perfectly amorphous material the bulk RAS signal will also cancel by symmetry and RAS will be an optical probe of the surface that may or not yield a non-zero signal depending on the symmetry of the surface. However if the bulk is not truly amorphous but is made up of anisotropic domains then the RAS will be a sum of the contributions from these domains that may or may not cancel out. In the simplest case in which the optical signal arises from a single dipole transition located in a plane at right angles to the direction of the incident light then a rotation of the specimen through an angle θ in the plane of the dipole, a technique termed azimuthally dependant RAS (ADRAS) [8], will yield an ADRAS signal that varies in intensity as $\cos 2\theta$. If the dipole orientation is not in the azimuthal plane then the angular variation of the ADRAS signal will be more complicated and if there are several dipole transitions with different orientations the ADRAS signal will be the superposition of these signals.

RAS is able to achieve surface sensitivity by measuring the difference in reflectance (Δr) of normal incidence linearly polarised light between two orthogonal directions in the surface plane (r_x,r_y) normalised to the mean reflectance (r) shown in equation 2.1

$$\frac{\Delta r}{r} = \frac{2(r_x - r_y)}{r_x + r_y} \qquad \{2.1\}$$

where r_x and r_y are the reflection coefficients of the surface directions.

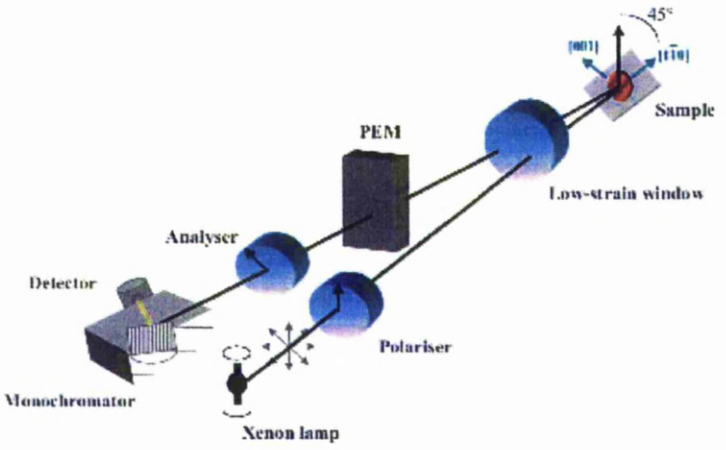

Figure 2.6. Schematic of the basic components of the RA spectrometer [9].

The individual components of the RA spectrometer are shown in figure 2.6. The mirrors are not show in the schematic, but are placed before and after the polariser and analyser to facilitate control over the position of the beam of light. A brief description of each of the components will follow.

The high intensity source of light is provided by a 75 Watt Super-Quiet 9 short arc xenon discharge lamp. It functions by means of an arc discharge when high voltages are applied across the anode to a high performance cathode in a xenon gas environment. This results in a reliable and stable output of a continuous spectrum in the IR to UV range (1.5-5.5 eV). Concave mirrors are used to produce a parallel beam of focused light from the incident diverging light emitted by the Xe-lamp and refocus the light reflected from the sample surface onto the monochromator entry slit, after it has passed through the photoeleastic modulator and analyser. The mirrors are coated with aluminum on glass, with a thin silica coating preventing mechanical abrasion. The polariser in the RAS equipment at The University of Liverpool makes use of a Rochon type prism that is very efficient for transmitting light in the UV region. Rochon prisms are beam splitting polarisers that consist of two attached quartz prisms that separate the ordinary and extraordinary polarized beams which are polarized perpendicular to each other. It is important to align the equipment so that the two beams which exit the polariser do not overlap. The light then reflects off the surface and passes through the PEM, which is crucial to maintain the surface specificity. The PEM is a tunable wave-plate which modulates the polarisation ellipse of the light reflected from the surface by exploiting the stress-induced

birefringence of the material. This ensures the collection of both the real and imaginary elements of the light wave by driving a quartz piezoelectric transducer at 50 kHz, the natural resonant frequency of the coupled fused silica optical element. The light passing through the PEM can be considered to have two orthonormal components polarised parallel and perpendicular to the modulation axis of the PEM. The PEM introduces an oscillating birefringence into the centre of the optical element and acts solely on the parallel component, therefore compressing the silica resulting in the component polarised parallel to the axis of modulation travelling faster than the perpendicular component and vice versa when the silica is stretched. This results in the retardation of one component in relation to the other; this is a phase modulation which is dependant on the polarisation state.

Once the light has passed through the PEM, it passes through the analyser. The purpose of the analyser is to convert the phase modulated signal from the PEM into an amplitude modulated signal which will be detected. This signal then passes through the monochromator that splits the light into its constituent wavelengths via a grating controlled by a computer controlled stepper motor. The final component shown in figure 2.6 is the detector, which is located immediately behind the exit slit of the monochromater and is a photomultiplier tube. It measures the intensity of light and converts the intensity modulated waveform into current. A full spectral scan can be performed in roughly 5 minutes. A full review of the technique can be found in Weightman *et al.* [9].

2.4 References

[1] F. Low, *About Bolomers*. "online" (2010). http://www.infraredlaboratories.com/About_Bolometers.html (Assessed: 16/04/2010).

[2] T. Keating, *Absolute THz Power-Energy Meters*. "online" (2008). http://www.terahertz.co.uk/index.php?option=com_content&view=article&id=140&Itemid=443 (Assessed 05/04/2010).

[3] D. Dooley, *Measuring THz radiation...choose pyroelectric detector or Golay cell*. "online" (2009) Paper Application note 1011 Rev.A. http://www.spectrumdetector.com/pdf/applicationNotes/1011.pdf (Assessed 09/11/10).

[4] R.J. Bell, *Introductory Fourier Transform Spectroscopy*. New York: Academic Press (1972).

[5] L. O'Leary, *Introduction to Fourier Transform Infrared Spectrometry*. "online" (2001) http://mmrc.caltech.edu/FTIR/FTIRintro.pdf (Assessed 09/11/10).

[6] D. Aspnes and A. Studna, *Phys. Rev. Lett.* **54**, 1956 (1985).

[7] M. Williams and D. Aspnes, *Phys. Rev. Lett.* **41,** 1667 (1978).

[8] B.F. Macdonald, J.S Law and R.J. Cole, *Appl. Phys.* **93**, 3320 (2003).

[9] P. Weightman, D.S. Martin, J.R. Cole, T. Farrell, *Rep. Prog. Phys*. **68,** 1251 (2005).

Chapter 3. Terahertz

This chapter introduces THz radiation, previous methods of generation and discusses its potential importance in biology.

In the last ten years biological studies in the THz region have increased as many of the difficulties in producing THz radiation are being overcome. There are many unanswered questions about the importance of THz radiation in understanding biological structure and organization as well as understanding its effects on human tissue. To enable experiments to be completed sources of high peak power and low average power are required in order to minimize potential thermal effects. In this chapter, THz radiation will be introduced, with a brief summary of how it has been previously generated followed by a look at its potential importance in biology.

3.1 Introduction to THz Radiation

The THz region of the electromagnetic spectrum is situated between the infrared and microwave regions. It is sometimes called T rays, T-light, Terahertz light, far infrared or submillimeter radiation. Despite THz radiation being energetically equivalent to many physical, chemical and biological interactions and processes, it has been a frequency range that has been very difficult to probe [1].

The phrase "terahertz gap" has been used to describe the region of the electromagnetic spectrum between photonics and electronics consequently illustrating the difficulty in generating THz radiation. In photonics a normal black body at 1400 K source produces only nanowatts of power over the THz range, while in electronics, the power generated from oscillators decreases with increasing frequency. As a result the THz region has remained relatively un-studied.

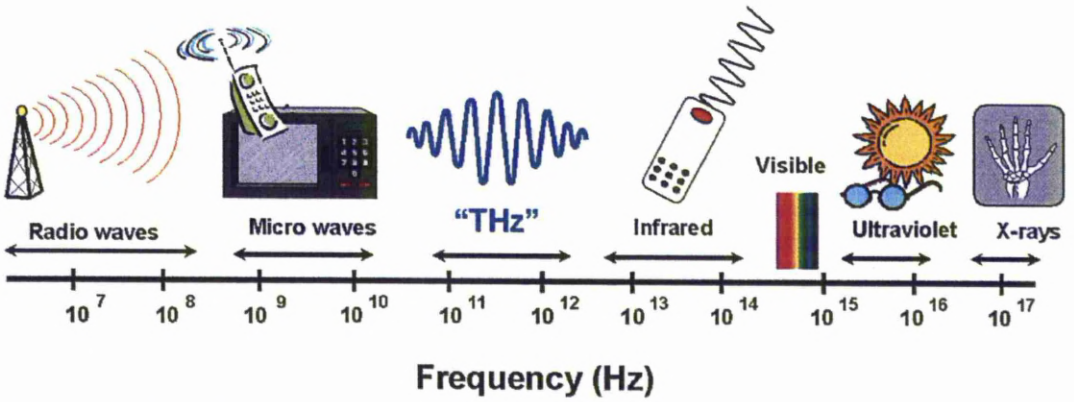

Figure 3.1. The electromagnetic specturm, showing the THz region. [http://www.sp.phy.cam.ac.uk/SPWeb/research/thzcamera/THzSpectrum2.gif]

The THz region of the spectrum is generally considered to cover wavelengths in the range 1 millimeter to 1 micrometer. THz radiation is non ionising and can

penetrate paper, clothing, wood, brick, plastics and other materials, however it is unable to pass through water or metal. It is these properties that have made it a very desirable radiation source due to its potential in a number of key applications within a variety of fields. One such potential application is its ability to identify materials such as biological warfare agents, concealed weapons, food contaminants or use as a medical diagnostic tool.

THz spectroscopy has played an important role in numerous scientific areas for a number of years including, radio astronomy, physical chemistry, atmospheric research and plasma research [2]. THz has also been used in chemistry to monitor the molecular structure and dynamics of CO (carbon monoxide), O_3 (ozone), ClO (chlorine monoxide) and H_2O for use in atmospheric studies [3]. Radio astronomers have monitored the THz emission from clouds of molecules in space to understand their chemical constituents, investigating their structure, temperature and internal motions [4,5]. There are a number of potential biological and medical uses for THz radiation that include, label free DNA analysis, early detection of skin cancer, bone density measurements, mammography and other medical diagnosis. While in security there are many potential uses, some of which are in development and others are used now, examples include; the detection of concealed weapons, spectrographic scanning of explosive gases and liquids, detection of voids in materials (also useful in the manufacturing process industry) and passenger screening. Further scientific development of THz radiation sources could provide extra sensitivity to environmental studies, molecular signature spectroscopy and potentially the molecular organization of life.

Due to the strong absorption of THz radiation by the hydrogen bonding network of water, there is a requirement for more powerful sources of THz radiation to allow experiments on biological systems, where water plays a vital function, to be performed.

3.2 History of THz Generation

THz radiation was first detected close to 100 years ago [7] however it is only in the past 10 years that great strides have been made in developing suitable THz sources for investigation into biological systems.

A number of different methods of generating THz radiation have been utilised over the last 40 years, and some of the more popular ones will be briefly

discussed. A more complete review of recent activity in the THz field by Plusquellic *et al.* [8] has outlined the various techniques and systems studied by different groups.

3.2.1 Laser Driven THz Emitters

The most widely used THz sources currently in use are laser driven THz emitters (some known as Difference Frequency Generation/mixing DFG DFM). These emit THz by the method of frequency down-conversion from the optical region. They are common sources for use with THz time domain spectroscopy (THz TDS). There are two main techniques that are developed from this principle to generate THz radiation.

The first involves shining a femtosecond laser (commonly Ti:Sapphire) onto a gap between closely spaced electrodes in a GaAs crystal photoconductor. This generates carriers which are accelerated by an applied bias field, resulting in a current which is coupled to an RF antenna through a stripline and generates a broadband THz source where the THz frequencies correspond to the Fourier transform of the initial laser pulse time profile [7,9].

Electro optical rectification (EOR) works by applying a sub picosecond laser pulse to a crystal with a large second-order susceptibility, *e.g.* ZnTe [10]. This results in a non-linear response of the crystal, where photomixing occurs. This produces a time varying polarisation that in turn produces THz emission. Photomixing involves two lasers interacting spatially (mixing) and focussed onto a photomixer device which produces a modulation of conductivity at the THz frequency which is emitted, after being converted into a current, from a pair of antenna [7].

These techniques usually generate THz radiation between 0.2-2 THz though the upper limit can be raised and is dependent on the laser input parameters. However average powers are limited to a maximum of 100's of μW and peak signals in the nJ range at a maximum. A major drawback and limitation of this technique is the input lasers, which can become relatively expensive, dependant on spectral requirement, potentially doubling in price [7].

3.2.2 Gas Lasers

Far infrared lasers have been used to generate THz radiation since the 1960's. They are optically pumped lasers that excite the vibrational levels of gas molecules at mbar pressure ranges. This then emits THz radiation at a specific frequency, dependent on conditions. Gas lasers are tunable between 0.3-5 THz, however they

have a limited power. These lasers are commercially available and are still considered suitable sources in certain aspects of THz research, including plasma diagnostics [11].

3.2.3 Quantum Cascade Lasers

Quantum cascade lasers (QCL) have been developed in the last ten years with their use in the range of 1-5 THz. The radiation can be generated in pulsed and continuous wave forms. They work by having electrons injected into a periodic structure of a super lattice under electrical bias. They then undertake intersubband transitions with THz photon emission produced by the resonant tunnelling through multiple wells, a cascade process. However they mainly have to be used at cryogenic temperatures in order to stop the thermal repopulation of the upper level at these wavelengths, and they are relatively weak sources. It is hopeful that in the future longer wavelengths will be able to be achieved [7].

3.2.4 Free Electron Based Sources

There are a number of free electron based sources, which include travelling wave tubes, Klystrons and backward wave oscillators (BWO). These sources are used in the microwave region and it is possible for them to generate radiation up to 1 THz. BWO's, like the microwave sources used and described in the chapter 2, are a slow wave device which generate electrons that spiral through a corrugated structure in an axial magnetic field, interacting with the first spatial harmonic of the backward wave producing radiation. The generated radiation has powers from 1-100 mW in the spectral range of 30 GHz to 1.2 THz [7].

3.2.5 Accelerator Sources

In the last ten years the introduction of accelerator sources of THz radiation have become possible due to improvements in accelerator RF resulting in the ability to produce short bunches, and therefore coherent radiation in the THz frequency. Motz [12] described the production of coherent radiation in 1951. He showed that in a uniform electron beam the contribution of individual electrons from the bunch to the radiation field are in a random phase, and therefore the power of the total field is equal to the N (N being number of electrons) times the the electric field of the electrons. However if the electrons are bunched within a distance that is comparable to that of the wavelength of radiation being emitted, their fields will add up in phase,

resulting in coherent radiation with a power level several orders of magnitude higher than that of non coherent radiation (N^2 the electric field of the electrons). This is the principle behind the high peak power THz radiation generated at ALICE, which will be discussed in chapter 4.

Free electron lasers use this coherent enhancement of short bunches, and the first FEL (Free Electron Laser) to provide THz radiation was the UCSB-FEL which produced radiation that was tuneable in the range of 120 GHz - 4.8 THz at power levels of 500 W – 5 kW with pulse durations of 1-20 μs at a machine rep rate of 1 Hz. At this time there are a number of FEL's that produce radiation in the IR to far IR region, with the THz FEL at Novosibirsk providing 100 W of power at a range of 120-180 μm by 2004 and in 2007 it was reported to produce an average power of 400 W at a range of 120-230 μm [13]. Such is the potential of FEL's that a European group of researches, EUROFEL, meet annually to discuss and share project designs. The aim is that each member of the group will produce a FEL that will cover the spectral ranges required for a number of experiments, and allow access to the research community [7].

There are also table top FEL systems where all the components that are in a FEL are compressed into a distance of around 3 m. These sources are highly tuneable and can generate up to 1.5 kW of power at their peak frequency. Other table top sources include black body sources, however these are known to have weak powers, as mentioned previously [7].

Accelerators have in more recent years been used to generate THz radiation by bending magnet radiation. JLAB (Jefferson Laboratory) is an example of this; they have an accelerator that is an Energy Recovery Linac (ERL). It is a photo injected energy recovery superconducting Linac, and generates THz radiation using conventional bending magnet radiation. Initial experiments performed at JLAB generated 100 W of CW radiation at 0.1-3 THz. Now they are able to generate powers up to the 2 kW range. Experiments at JLAB have shown that the generation of THz in this way can be very beneficial once coherent enhancement is achieved. They established experimentally that when the bunch length is longer than that of the wavelength of light being emitted, the total power would be the number of electrons N multiplied by the energy of one electron. However once the bunch length is shorter than that of the wavelength of light being emitted, coherent enhancement results in

the total power being N^2 multiplied by the electron energy. At JLAB there are in the order of 10^9 electrons per bunch, so this enhancement can make a very large difference. The electron bunches are shortened by the ability to place an "energy chirp" on the bunch and being compression in a magnetic compression chicane [14]. The ALICE accelerator at Daresbury laboratory produces THz in the same way and this process will be discussed further in chapter 4.

A more complex study of THz technology, including some techniques not covered here, can be found in Siegel [15].

3.3 Terahertz in Biology

THz radiation has the potential to reveal important information about the long range molecular organisation of biological systems. Since biological molecules have evolved at room temperature, their functional behavior must exploit the molecular motions that can be driven by the release of free energy at room temperature. These molecular motions (H-bonds and Van der Waals forces) are in the terahertz region of the electromagnetic spectrum since kT (free energy) at room temperature is ~ 6 THz. Therefore, it is possible that, the understanding of the complexity of molecular organization could lie in vibrations in the THz region as argued many years ago by Frohlich [16]. THz radiation has the potential to produce thermal affects in biological systems, with thermal affects known to increase entropy, and disorder. Therefore, key questions to further understand whether THz modes play a crucial role in Biology are; Do THz modes distribute and use free energy released by molecular interactions? Do these modes live long enough to organise the processes important to life? Is quantum coherence important at the molecular level in cells? What modes of vibration drive cell division, or DNA copying?

These vibrational modes must be available at room temperature and so it is possible that these molecular motions will also be in the THz region of the electromagnetic spectrum. Is it merely coincidental that so little is understood of the way molecules have self-organised throughout evolution at room temperature, and we have been unable to probe this region of the electromagnetic spectrum? Experimental results are scarce and theory gives us two contrasting possible answers. Frohlich [16] suggests that the answer to these questions is no. He proposed that metabolic processes could stimulate coherent excitations in biological systems, and showed that the natural frequency of cell membranes is ~ 1 THz (10^{12} Hz). He also

suggested that interaction with water is important. However Adair [17] argued that THz modes dissipate energy into adjacent modes in ~ 10 psec (10^{-11} sec), he proposed that this would be due to dampening of the absorbed energy, and estimated that even in considerably weaker dampened systems, than would be expected there would still be no effect. Mingaleev disagrees with Adair's suggestion that dampening will result in no THz effect and suggests that despite "viscous dampening" these important effects are still possible and could play a part in the kinetics of conformational phase transitions of semi flexible biopolymers in solution [18].

Frohlich proposed that THz modes could play a vital role in the long-range interaction of biological molecules. Many biological polymer systems contain basic repeating sub-units (proteins with chains of amino acids) and each can contain complex structures which allow them to carry long-lived non linear excitations [19,20]. These excitations can interact through the long range Coulomb forces establishing a branch (or many branches) of longitudinal electric modes where the frequency is expected to be 10^{11}-10^{12} Hz (0.1-1 THz). Energy could be stored via the long chains through non linear excitations and Frohlich suggested that if energy were to be inserted or removed from one of the components of a branch, then the electric modes of the whole branch would be affected through long range interaction [16]. This could be important in protein folding, DNA replication and other crucial biological processes.

The rate of energy supplied to the system was also considered to be important by Frohlich. He theorized that if the rate of energy supply was sufficiently large, the energy could be channelled into a single mode, which then presents a strongly excited coherent longitudinal electric vibration. This single mode would exhibit long-range phase correlations. If the energy supply was sufficiently high this could result in an instability within the molecule [16].

The energy of the chemical bonds that make up biological molecules can be anything from 100-800 kJ/mol with Hydrogen bonds between 2-161 kJ/mol depending on the system, for reference these energies should be compared with 7.9 KJ/mol for bulk water (dipole-dipole interactions are between 0.5-2 KJ/mol). 1 THz is roughly 0.4 kJ/mol, (6 THz = 2.4 kJ/mol and 12 THz = 5 kJ/mol). The calculation is shown below.

$$E = h\nu = 1 \times 10^{12}\ \text{Hz} \times 6.64 \times 10^{-34}\ \text{Js}$$

$$E = 6.64 \times 10^{-22} J/photon$$

The next step is to change the energy units from J/photon to kJ/mol.

$$E = 6.64 \times 10^{-22}\ J/photon \times N_A$$

where N_A is the Avogadro constant (6.6022×10^{23}).

$$E = 6.64 \times 10^{-22}\ J/photon \times 6.022 \times 10^{23}$$
$$E = 400\ J/mol = 0.4\ kJ/mol$$

Therefore it can be considered that THz frequencies could possibly affect long range ordering of Van der Waals forces (3-10 THz) and hydrogen bonding within systems. This results in THz radiaion having the potential to interrogate vibrational modes that extend across long portions of biological framework with length scales extending over 10's of Angstroms. This combined with the energies corresponding to Van der Waals forces and hydrogen bonding means that it can probe the inter and intra molecular bonding with the THz modes causing all of the atoms within a structure to vibrate [10].

Due to the ability of THz radiation to probe long range order, it has the potential to probe conformational structure of biological polymers, which are fundamental to their activity. Non-linear excitations could cause local softening of a polymer structure, with the rigidity of the structure decreasing as the amplitude of excitation of non-linear modes increases. Mingaleev *et al.* [18] suggested that once the amplitude of the excitation increases above a threshold value, the effective binding rigidity would become negative causing instability within the chain. A further increase of non-linear excitation could result in the collapse of the instability causing a chain to coil [18]. These long range modes, interrogated by THz radiation will extend over large portions of the molecular framework, with length scales reaching into the tens of Angstroms and so it is hoped will be able to exploit these possible instabilities [21]. This is vitally important in research into RNA/DNA and proteins in further understanding the transformations in secondary and tertiary structures of the molecules. To show an example of the complexity of biological structures, the structure of a protein is described below; it is split into four types, primary, secondary, tertiary and quaternary. The primary structure is considered to be a chain of amino acids that make up the protein, without an allowance for spatial arrangements. The secondary structure takes the side chains into consideration giving

the protein its structure, the alpha helix, beta sheet and random coil backbone, which are built with peptides and always have a similar geometry. When this secondary structure starts to fold into loops, turns and spirals it forms a tertiary structure. This folding is generally driven by a change in conditions or by a chemical change in structure *e.g.* hydrogen bonding. This structure is vital to the function of a protein. The quaternary structure is made up of a number of subunit peptide chains, however not all proteins have this fourth type of structure *e.g.* those that exist as monomers [22,23].

A further potential area for THz radiation is to explore the time structure of biological processes, that are vital to life. THz frequencies give access to times set in the sub picosecond domain and therefore could provide suitable analysis on biological process pathways [2].

3.4 THz Radiation Experiments of Biological Molecules

The modes that drive cell division, DNA copying *etc*, must be avaliable at room temperature, where evolution has taken place, and so it is likely that the molecular motions are in the THz region. Any affect on the DNA is going to have important implications for all cell processes and mechanisms.

One of the earliest studies of the effect of THz on DNA frequencies was reported by Lindsay and Powell [24] who observed a mode in DNA films at 0.36 THz while further work by Powell *et al.* [25] detailed four vibrational bands near 1.89, 2.49, 3.00 and 3.30 THz on FTIR measurements of free-standing, unorientated films of polycrystalline DNA in the range 1.20 – 15 THz. Wittlin *et al.* [26] probed highly orientated films of DNA salts (Na and Li) in the range 0.09 – 13.50 THz as a function of temperature (5 – 300 K). Five vibrational modes were identified including the lowest frequency modes at 1.35 THz for Li-DNA and 1.23 THz for Na-DNA. These modes were found to red-shift with hydration. The reason for the use of dried films is in order to limit the attenuation of THz by water.

A number of studies by Globus and co-workers [27,28] have utilised FTIR to produce high resolution THz spectra typically in the range 0.30 – 0.75 THz to investigate randomly and partially orientated semi-dry 50 – 300 mm thick DNA films [27], 1 – 250 mm thick dried films of known sequences of single-stranded RNA potassium salts and double-stranded RNA sodium salts [28]. Transmission spectra of liquid and solid films of ss/ds (single-stranded/double-stranded) salmon

and herring DNA sodium salts were also taken [29], the absorption coefficients and refractive indices from reflection and transmission studies of ss/ds salmon and herring DNA for dried film samples [30] and salmon and herring DNA sodium salts suspended in water or buffer solution [30]. The dried samples were typically produced either to be free standing or applied to a near transparent substrate. These studies are consistent in reporting the sensitivity of the system to sample preparation, sample thickness, sample orientation, water content and in particular, drying conditions. THz transmission intensity variations of between 0.5 – 2 % are typically reported at overall transmission levels of ~ 90 % and were interpreted as evidence of high density IR-active modes [27]. The absorption of THz radiation by ss-DNA was shown to be ~ 20 % higher and to be distinguishable from ds-DNA by the presence of different spectral features [21, 29-30]. Globus *et al.* [21] also observed these spectral features to sharpen and increase in intensity for samples suspended in solution. The authors conclude that the occurrence of numerous resonances due to long wavelength vibrational modes within biological molecules are intrinsic properties of biological material [21].

A further study [31] used THz–TDS in the range 0.10 – 4.00 THz on bulk, free standing and spots of two artificial RNA single strands composed of polyadenylic acid (poly-A) and polycytidylic acid (poly-C). Poly-C was found to absorb more and have a 10 % larger refractive index than poly-A for the bulk samples consequently permitting an easy distinction between the two. There were no sharp spectral features recorded for either bulk samples, free standing thin films or for the spots. The results of Ref. 31 contradict those of Globus *et al.* [27,28] who noted sharp and structured absorption of RNA polymers. Jepsen *et al.* [31] explain that a large number of IR-active modes are expected in this region, which results in an adsorption profile without defined features. For bulk samples it is obvious that these modes will be highly sensitive to the local environment where neighboring molecules result in weak intermolecular interactions.

A THz–TDS study by Markelz *et al.* [32] presented the THz absorption spectra of lyophilised powder samples of calf thymus DNA, bovine serum albumin (BSA) and type I collagen in the range 0.06–2.00 THz. For each of these molecules, broadband absorption spectra increasing as a function of frequency were observed, suggesting that large densities of long wavelength collective modes of vibration are IR active in this region. DNA was investigated under different conditions of relative

humidity to study the hydration dependence of the THz response and a difference between the spectra were recorded at relative humidity levels of < 5 %, 43 % and 70 %. The authors noted that DNA is expected to have varying conformations dependent upon the level of hydration therefore displaying the sensitivity of THz to dynamic changes in biomolecular structure. THz–TDS has also been used to study DNA hybridisation [33,34] and large differences were reported in the THz absorption following hybridisation of ss-DNA.

Numerous THz experiments on proteins and other biological polymer molecules have been performed with the THz spectra being very sensitive to conformational structure of the molecules. Walther *et al.* [35] suggested that due to the vibrational modes in the THz region corresponding with intermolecular modes, internal motion and lattice vibrations in crystalline samples, that the THz spectra would provide a vital insight into conformational changes and were able to present spectral differences of compounds despite only very small changes in the molecules molecular conformation. Research by Qu *et al.* [36] monitored the THz spectra of proteins and concluded that they could distinguish between conformational differences in proteins even if the secondary and tertiary structures of the protein were very similar. Balu *et al.* [37] observed the THz spectra of two proteins with a very similar conformational structure and found that they responded in a similar way to THz modes of vibration confirming the importance of the THz region in understanding and detecting conformational affects in proteonomics. Taday *et al.* [38] also reported this high sensitivity to conformation of biomolecule explaining its potential importance in the pharmaceutical industry due to the high dependance on conformation. Two papers by Hellwig *et al.* [39-40] suggests the THz spectra is a result of the hydrogen bonding network with a H-bonding continuim between 300-50 cm^{-1} (9-1.5 THz). They monitored the FIR and MIR while making changes to the structure and monitored the difference in both regions resulting in a conclusion that it would be possible to show the rearrangement of a protein during a reaction and therefore track the mechnism. In the second paper they suggested that the broadness of the peaks in this continuum were dependent on the polarizability of the H-bonding features, although further reporting that because of the complexity of the number of vibrational modes it was not possible to perform these experiments and distinguish similar conformational changes in different proteins.

Other research has concentrated on understanding the effects of THz modes on biological systems. Despite this research the controversy behind the effects of THz radiation on biological systems is still as strong as it was when Frohlich made his original hypothesis over 40 years ago. There have been a number of studies performed in the past both in *vivo* and in *vitro* with conflicting results. Studies have shown significant effects on increased genomic instability [41], reduction in enzyme activity [42] and increased anxiety in mice [43]. Homenko *et al.* [42] also suggest that THz radiation could affect protein binding recognition which could result in major disruption to cellular processes and development.

However there are studies that suggest there are no effects from THz radiation [44-46]. A major international research project known as the "THz bridge" project, focussed on the THz induced genotoxicity (damage to the genetic information). It concluded that under some specific conditions of exposure a genotoxic affect took place as well as alterations to the permeability of membranes. Conversely other studies within the same project, that monitored the chromosome damage and cell cycle dynamics showed no effects from THz radiation [47]. Bock *et al.* [48] suggested that extended exposure to broad spectrum THz radiation results in specific changes to cellular functions closely related to DNA-directed gene transcription. They found that 89 % of genes were not affected by the radiation however a small amount were activated while an equal amount were repressed. It was suggested that THz radiation could be a potential tool for cellular reprogramming. A recent theoretical study by Alexandrov *et al.* [49] suggests that a THz radiation exposure may significantly affect the natural dynamics of DNA by producing spatially localised opening of a dampened and driven DNA chain, due to linear instabiliteis leading to dynamic dimerisation. They believed that this response would be highly specific to THz frequency and could influence a number of molecular processess which would affect gene expression and DNA replication. The investigation by Mingaleev *et al.* [50] argues that the bending in a semi-flexible biopolymer curved chain acts as an effective trap for THz modes. However, even though nonlinear instability may occur, it is required to occur in the presence of significantly fluctuating amplitude, which in biological systems is generated thermally. It is therefore rare for a fluctuation with sufficiently large amplitude to occur in the presence of a THz field, especially if the power is small. It is thought that at ALICE, with the ability to perform these experiments with a higher peak

power, it would potentially result in large fluctuating amplitude that would be able to trap a nonlinear localised instability in the region of the THz spectrum, where previous investigations have identified specific vibrational modes. This could ultimately lead to the creation of localised permanent openings in ds-DNA chains and/or denaturing itself. Hence excitations will propagate along the chain rather than being damped in lateral directions. These experiments are yet to be performed so this hypothesis is currently untested, however this will be discussed further in the Zebra fish exposure chapter.

3.5 Conclusions

It is clear that the role of THz radiation in biology, while still in its infancy, is very controversial. The spectral properties of a number of biological molecules have been performed, however a more thorough understanding of the effects of THz modes on biological systems is still required. All papers published in this area, whether they believe THz radiation to play a crucial role in biological organisation or not, agree that further investigation in this area is required and the key to understanding the role of THz radiation is to perform experiments with intense THz sources. The major technique used to probe the THz response of biological molecules has been Fourier transform reflection/transmission spectroscopy (THz–FTIR) [18,24-30] although a number of other studies have used time resolved THz spectroscopy (THz–TDS) [32-34,38]. Most of these previous studies have used low intensity laboratory sources.

ALICE is an ideal source for this programme since it generates high peak power with low average power THz radiation. This is important for biological experiments as it limits any effects due to temperature change. The high peak power source will also allow experiments to be performed with the molecules in water, allowing to closely monitor the protein conformation while in the presence of small amounts of water, or look at the affect of THz on cells, discussed in chapter 5. The lack of defined features in the THz region is not an issue in the experiments performed in this thesis. This is because the experiments performed in chapter 5 are simple exposure experiments where no spectral information is collected. In chapter 6, the heparin chapter, where the THz radiation is used in an attempt to understand the long range conformation of the molecule, rather than attempting to find specific features. Therefore it will allow experiments to be performed that will probe this long discussed area.

3.6 References

[1] G.P. Williams, *Rep. Prog. Phys.* **69,** 301 (2006).

[2] T.W, Crowe, T, Globus, D.L Woodlard, and J.L. Hesler, *Phil. Trans. R. Soc. Lond. A.* **362**, 365 (2004).

[3] F.C. De Lucia, 2002 *IEEE Microwave Theory and Techniques Society International Microwave Symposium Digest.* **3**, 1579. New York: IEEE Press..(2002)

[4] J.M. Payne, *Proc. IEEE.* 77, 993 (1989).

[5] T.G. Phillip and J. Keene, *Proc. IEEE.* **80**, 1662 (1992).

[6] A.R. Orlando and G.P. Gallerano, *J. Infrared. Millim. Te.* **30,** 1308 (2009).

[7] G.P. Gallerano and S. Biedron, *Overview of Terahertz radiation sources*, Proceedings of the 2004 FEL conference, 216-221 (2004).

[8] D.F. Plusquellic, K. Siegrist , E.J. Heilweil and O. Esenturk, *Chem. Phys. Chem.* **8**, 2412 (2007).

[9] D.H. Auston, K.P. Cheung, J.A. Valdmanis and D.A. Kleinman, *Phys. Rev. Lett.* **53**, 1555 (1984).

[10] Z. Jiang and X.C. Zhang, *IEEE. T. Microw. Theory.* **47**, 2644. (1999).

[11] J. Faist, F. Capasso, D.L. Siyco, C. Sirori, A.L. Hutchinson and A.Y. Cho, *Science.* **246**, 553 (1994).

[12] H. Motz, *J. Appl. Phys.* **22**, 527 (1951).

[13] E.J. Minehara, *Nucl. Instrum. Meth. A.* **575**, 54 (2002).

[14] G.L. Carr, M.C. Martin, W.R. McKinney, K. Jordan, G.R. Neil and G.P. Williams, *J. Biol. Phys.* **29**, 319 (2003).

[15] S.A. Ponchak, *IEEE T Microw. Theory.* **50**, 1101 (2002).

[16] H. Fröhlich, *Int. J. Quantum Chem.* **2**, 641 (1968).

[17] R.K. Adair, *Biophys. J.* **82**, 1147 (2002).

[18] S.F. Mingaleev, Y.B. Gaididei, P.L. Christiansen, and Y.S. Kivshar, *Europhys Letts.* **59**, 403 (2002).

[19] A. Xie, L. Meer, W. Hoff, and R.H. Austin *Phys. Rev. Lett.* **23**, 5435 (2000).

[20] M. Peyrard and J. Farago, *Physica A.* **288**, 199 (2000).

[21] T. Globus, D.L. Woolard, T. Crowe, T. Khromova, B. Gelmont, and J. Hesler, *J. Phys.* **39**, 3405 (2006).

[22] J. Voet and D. Voet, *Biochemistry 2nd ed.*, John Wiley and Sons, INC, New York (1995).

[23] D. Elliot and W.H. Elliott, *Biochemistry and Molecular Biology 4th ed.*, Oxford University Press, New York (2009).

[24] S.M. Lindsay and J. Powell, *Structure and Dynamics: Nucleic Acids and Proteins*, edited by Clementi, and R. H Sarma. Adenine, New York, (1983).

[25] J.W. Powell, G.S. Edwards, L. Genzel, F. Kremer, A. Wittlin and W. Peticolas, *Phys. Rev. A.* **35**, 3929 (1987).

[26] A. Wittlin, L.Genzel, F. Kremer, S. Heseler and A. Poglitsch, *Phys. Rev. A.* **34**, 493 (1986).

[27] T. Globus, D.L. Wooloard, A.C. Samuels, B.L. Gelmont, J. Hesler, T.W. Crowe and M. Bykhovskaia, *J. Appl. Phys.* **91**, 6105 (2002).

[28] T. Globus, M. Bykhovskaia, D. Woodlard and B. Gelmont, *J. Phys. D.* **36**, 1314 (2003).

[29] T. Globus, R. Parthasarathy, T. Khromova, D. Woolard, N. Swami, A.J. Gatesman and J. Waldman, *Proc. SPIE-Int. Soc. Opt. Eng.* **5584**, 44 (2004).

[30] R. Parthasarathy, T. Globus, T. Khromova, N. Swami, D. Woolard, *Appl. Phys. Lett.* **87**, 113901 (2005).

[31] B.M. Fischer, M. Hoffmann, H. Helm, R. Wilk, F. Rutz, T. Kleine-Ostmann, M. Koch and P.U. Jepsen, *Opt. Express.* **13**, 5205 (2005).

[32] A.G. Markelz, A. Roitberg, and E.J Heilweil, *Chem. Phys. Lett.* **320**, 42 (2000).

[33] M. Brucherseifer, M. Nagel, P.H. Bolivar, H. Kurz, A. Bosserhoff, and R. Buttner, *Appl. Phys. Lett.* **77**, 4049 (2000).

[34] M. Nagel, F. Richter, P.H. Haring-Bolivar and H. Kurz, *Phys. Med. Biol.* **48**, 3625 (2003).

[35] M. Walther, P. Plochocka, B. Fischer, H. Helm and P. Uhd Jepsen, *Biopolymers.* **67**, 310 (2002).

[36] Y.G. Qu, H. Chen, X.C Qin, L.Wang, L.B Li, and T.Y. Kuang, *Sci. China. Ser. C: Life. Sci.* **50**, 350 (2007).

[37] R. Balu, H. Zhang, E. Zukowski, J.Y. Chen, A.G. Markelz, and S.K. Gregurick, *Biophys. J.* **94**, 3217 (2008).

[38] P.F. Taday, I.V. Bradley, D.D. Arnone and M. Pepper, *J. Pharm. Sci-us.* **92**, 831 (2003).

[39] Y.E. Khoury, R. Hielscher, A. Trivella, and P. Hellwig, *IRMMW-THz* .1948 (2010).

[40] Y.E. Khoury, R. Hielscher, A. Trivella and P. Hellwig. *IRMMW-THz 2010.35th Internation Conference on Infrared Millimeter and Terahertz Waves,* 5612698. (2010).

[41] A. Korenstein-Ilan, A. Barbul P. Hasin A. Eliran A. Gover and R. Korenstein, *Radiat. Res.* **170**, 224 (2008).

[42] A. Homenko, B. Kapilevich, R. Kornstein, and M.A. Firer, *Bioelectromagnetics* **30**, 167 (2009).

[43] N.P. Bondar, I.L. Kovalenko D.F. Avgustinovich, A.G. Khamoyan, and N.N. Kudryavtseva, *Bul. Exp. Biol. Med.* **145**, 401(2008).

[44] R.H. Clothier and N. Bourne, *J. Biol. Phys.* **29**, 179 (2003).

[45] M.R. Scarfi, M. Romano, R. Di Pietro, O. Zeni, A. Doria, G.P. Gallerano, E. Giovenale, G. Messina, A. Lai, G. Campurra, D. Coniglio and M. D'Arienzo, *J. Biol. Phys.* **29**, 171 (2003).

[46] O. Zeni, G.P. Gallerano, A. Perrotta, M. Romano, A. Sannino, M. Sarti, M. D'Arienzo, A. Doria, E. Giovenale, A. Lai, G. Messina and M.R. Scarfi, *Health Phys.* **92**, 349 (2007).

[47] A. Doria, G.P. Gallerano, E. Giovenale, G. Messina, A. Lai, A. Ramundo-Orlando, V. Sposato, M. D'Arienzo, A. Perrotta, M. Romano, M. Sarti, M.R. Scarfi, Spassovsky and O. Zeni, *Infrared. Phys. Techn.* **45**, 339 (2004).

[48] J. Bock, Y. Fukuyo, S. Kang, M.L Phipps, L.B Alexandrov, K. Rasmussen, A.R. Bishop, E.D. Rosen, J.S. Martinez, H.T. Chen, G. Rodriguez, B.S. Alexandrov and A. Usheva, *Plos. One.* **5**, 1 (2010).

[49] B.S. Alexandrov, V. Gelev, A.R. Bishop, A. Usheva A. and K. Rasmussen, *Phys. Lett. A.* **374**, 1214 (2010).

[50] S.F Mingaleev, Y.B. Gaididei, P.L. Christiansen Y.S and Kivshar, *Europhys. Lett.* **59**, 403 (2002).

Chapter 4. ALICE

This chapter introduces the Energy Recovery Linac accelerator, ALICE, and details the commissioning of the THz beam line concluding in the successful transport of THz radiation to the TCF.

This chapter covers the work performed on the ALICE accelerator. This work involved the commissioning of the THz beam line at ALICE where THz is generated in the same manner that it is generated at JLAB and discussed in the previous chapter. The ALICE accelerator will be discussed and a chronological timeline of the commissioning of the beam line will be given together with comparisons with the experimental data and theoretical considerations.

The energy recovery linac prototype (ERLP) at STFC Daresbury Laboratory, now named ALICE, an acronym that stands for Accelerators and Lasers in Combined Experiments, is a prototype of a new design of fourth generation light sources featuring an Energy Recovery Linac and is the first of its type to be built in Europe. The ALICE accelerator can produce short intense bunches of electrons to provide a variety of sources which can be used on their own, or in combination with synchronized lasers [1]. The Liverpool group are interested in the potential of ALICE to generate high peak power, low average power THz radiation, which has considerable potential for research in biology. The high peak power, low average power THz radiation generated by ALICE is central for further research into biological systems as it limits any effects due to temperature change, while being strong enough to probe systems in their normal surroundings, water. Therefore it will allow experiments to be performed that will advance this important field.

4.1 A Brief History of Synchrotrons

A synchrotron is an accelerator that accelerates charged particles to very high energies through a magnetic field in combination with a high-frequency electrostatic field and circulates these electrons through an electron transport system.

Synchrotrons work on the basic principle that when electrons are accelerated to the total radiated power they radiate when deflected by a magnetic field, with their relativistic power shown in Larmor equation {4.1}. This property has been taken advantage of all over the world for many years, resulting in the creation of a number of light sources that produce what is known as synchrotron light, or synchrotron radiation.

$$\text{Relativistic Power (W)} == \frac{e^2 v^4 \gamma^4}{6\pi\varepsilon_0 c^3 r^2} \qquad \{4.1\}$$

where e is electric charge (C), v is velocity (m/s), c is the speed of light ($2.998\text{x}10^8$ m/s) and ε_0 is the permittivity of free space ($8.854\text{x}10^{-12}$ F/m or C^2/Jm), γ is the

particle acceleration ranging from 100 to several 1000 (this is due to the rest mass being 0.5 MeV while accelerators have beams, typically, between 10-1000 MeV), and r is the bending radius (m).

The first known light source generated from accelerating electrons to their relativistic energies was developed parasitically on an electron synchrotron. The parasitic generation is classed as 1st generation light sources, they were mainly particle physics machines that were adapted to allow light generation to take place. These were replaced by 2nd generation sources, which had a storage ring where the electron beam was circulated and stored [2].

3rd Generation sources are similar to the 2nd Generation sources, in the fact they have a storage ring with electrons injected at specific times, however they are not completely circular unlike 2nd Generation sources, as they have stretches of straights allowing for wigglers and undulators to be installed. The electron beams also have a lower emittance due to the use of complex insertion devices [1].

Equation 4.1 is calculated for one electron, however in accelerators electrons travel in bunches. As the electron bunches circulate round a machine there are beam losses, which can be corrected by the use of RF (radio frequency) cavities. The RF cavities also control bunch length and as a result the RF plays a vital role in ALICE, which is a 4th generation light source. Unlike 3rd generation light sources, where electrons travel around a storage ring many thousands of times a second, at ALICE the electron bunch only traverses the beam transport system once. In 3rd generation sources the electron bunches lengthen over time eventually reaching an equilibrium state [2].

This enables 4th generation light sources to generate short bunches of high intensity electrons which can be used for Free Electron Lasers (FEL's) and THz radiation. Having the potential to create short bunches allows high peak power sources of radiation of varying wavelengths with a comprehensive tenability and timing structure.

4.2 The ALICE Accelerator

ALICE produces intense, short electron bunches when an intensely powerful multi terra-Watt laser bombards the semiconducting surface of the gun. The bunches of electrons are then accelerated by superconducting RF cavities to 35 MeV, travelling

at close to the speed of light, before being compressed in a chicane which results in the production of intense short pulses of radiation in the THz region of the spectrum.

The compression of the bunch will lead to coherent emission, sometimes described as multiparticle coherence, which was briefly described in chapter 3. It occurs when the length of the electron bunch, generating the radiation, becomes shorter than the wavelength of light being emitted. This produces far higher intensity radiation than conventional synchrotron radiation and is important for biological experiments.

A tissue culture facility has been built on the ALICE THz beam line, a world first which will allow cells to be cultivated and maintained in a suitable environment and allow the effects of THz radiation to be closely monitored using a number of assays and experiments simultaneously.

During ALICE's lifetime it will enable scientists to probe in minute detail, biological, chemical and physical processes at the atomic level, which could assist in the development and improvement in a number of scientific areas, from cancer research to designing more efficient solar cells. Understanding how the machine runs will allow scientists to investigate and overcome scientific challenges standing between them and future generations of accelerators, such as the NLS (New Light Source) project being designed and discussed in the UK [1].

4.2.1 ALICE – The Electron Beam Line and Generation of THz

The ALICE electron beam line consists of a highly efficient photocathode gun, superconducting linacs and a bunch compressor, as shown in the schematic diagram in figure 4.1. ALICE operates in an energy recovery mode whereby the electron bunch only circulates the beam transport system once and returns to the superconducting cavity (linac) out of phase with the RF and returns the majority of its energy to the accelerating cavities for use in accelerating subsequent bunches. This energy recovery means that the electron beam (generated 20 times a second) can be safely dumped without a high amount of induced radioactivity. It also results in less RF power required to drive the linac. This is less important when working with short trains, however the long train mode, which is used for the generation of THz radiation, the RF cavity's load would be significantly greater which is not possible with the current set up. Energy recovery was first demonstrated in late 2008 [3].

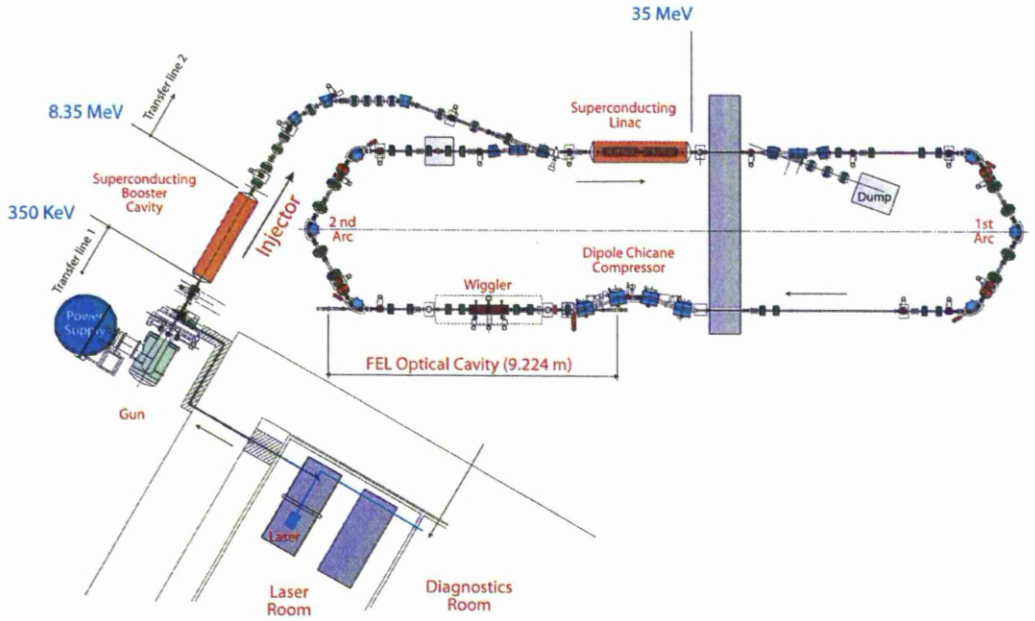

Figure 4.1. This shows the layout of the ALICE accelerator from above.

ALICE was designed with a beam energy of 35 MeV. Initial energy recovery was demonstrated at 20.8 MeV. Conditioning the RF cavities has allowed the accelerating gradients to be increased, so that the linacs first produced beams of 30 MeV in the summer of 2009, this is important for both THz generation and the FEL.

A variety of pulse structures from single bunch to 100 microsecond long trains can be generated, some of which are illustrated in figure 4.2. The design specification is 80 pC bunch charge with 100 microsecond long trains. 80 pC has been achieved in single bunch mode, however due to issues with the accelerator RF, 40 pC was the maximum bunch charge obtained in long bunch trains as of December 2010.

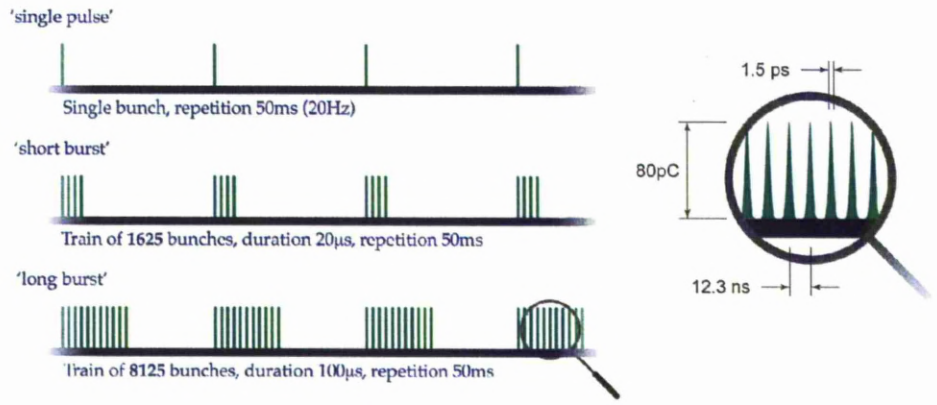

Figure 4.2. The various pulse structures possible at ALICE.

The Alice accelerator's short pulsed light sources are:

- mid infrared FEL, tunable from 4 to 12 microns,
- X-rays produced by Compton scattering a synchronised TW laser from the bunches,
- THz from coherent enhancement.

The electron bunches are generated when a laser pulse hits a DC photoelectron gun generating and accelerating short (typical length of several ps) electron bunches to 350 keV. As these bunches are accelerated there is an energy variation within the bunch, consequently as they travel towards the first linac (labeled booster in figure 4.1) the bunches would lengthen further, with the electrons at the front of the bunch travelling faster than those at the back (note they are not at relativistic speeds at this point). To correct this there is a "buncher" prior to the booster, which accepts the bunch at "zero cross" where the bunchers RF slows the front electrons and accelerates those at the back, thus shortening the bunch.

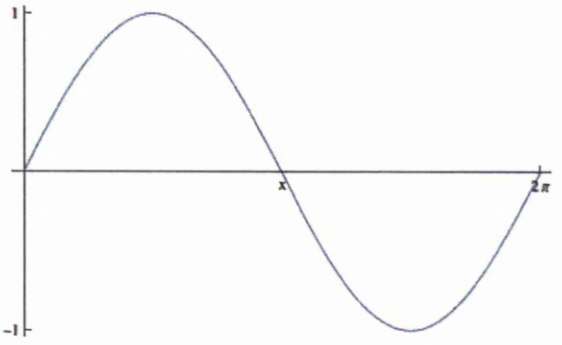

Figure 4.3. Phase of the RF, from Linac cavities and the buncher.

Figure 4.3 shows the RF phase, that is present in both linac cavities and the buncher. This is a sine wave with the amplitude being the amount of acceleration the cavity or buncher gives the electrons within the bunch. By "zero crossing" the electron beam with the buncher phase (x) the electron bunch enters so the centre of the bunch receives no acceleration from the RF cavity. The electrons moving faster at the front of the bunch will receive a slight deceleration, while those at the back of the bunch will be accelerated, compressing the bunch in longitudinal space and normalizes the speed of the electrons within the bunch. The electron bunch then enters the booster linac, which accelerates the electrons to 8.35 MeV, which is close to relativistic speeds. The booster phase can be changed to produce the best and most suitable bunch conditions.

The electron bunch then leaves the injection line and is bent by the magnets into the main linac which increases the beam energy to a maximum of 35 MeV. The electron bunches enter the linac with the accelerating phase chosen so that a specific energy chirp is placed on the bunch, allowing it to be compressed longitudinally in the magnetic bunch compression chicane resulting in the generation of THz radiation. This compression is vital as it allows for the coherent enhancement of THz production (this will be discussed further in next section). The machine timing structure means that the peak power is accompanied by a low average power making it the perfect system for biological exploitation as mentioned in chapter 3.

The electron bunch, now with a length of < 1 ps passes through an undulator (FEL) allowing, 5 μm laser generation, before returning via arc 2 to the main linac, at a specific time so it enters out of phase (with respect to the linac accelerating phase). The electron bunch is therefore decelerated, expelling its energy to the electromagnetic field inside the linacs RF cavities, thus producing energy recovery. The beam exiting the linac for the second time is now back to the 8.35 MeV and is bent by the magnet downstream of the linac (smaller energy beams are deflected more by magnets) to the 8.35 MeV beam dump.

4.2.2 Bunch Compression

The bunch compression is essential for the production of high power THz radiation. Figure 4.4 shows the theoretically calculated onset of coherent enhancement under the original specifications designed for ALICE, 35 MeV beam energy, 80 pC bunch

charge, 100 μsecs train length, 0.6 ps RMS (Root Mean Square) bunch length and a machine rep rate of 20 Hz. For further information on the theoretical calculation see "The THz radiation model of ALICE" section.

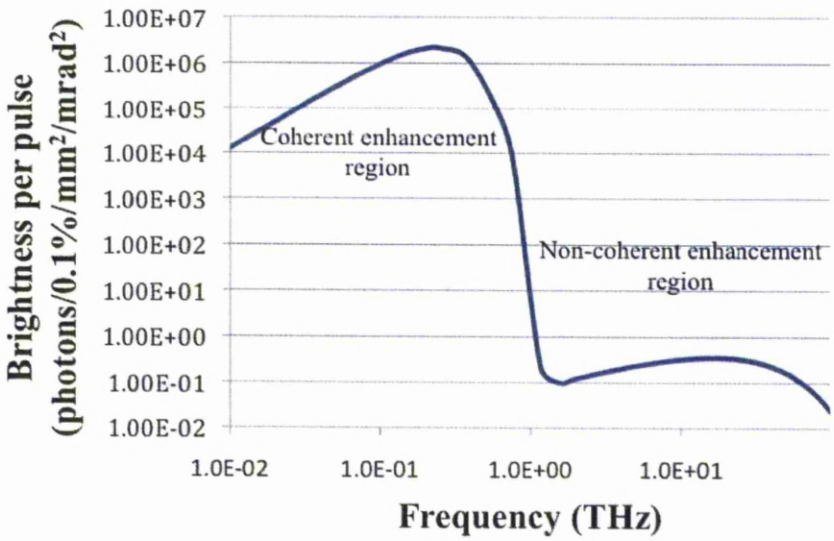

Figure 4.4. Importance of coherent enhancement on production of THz radiation.

The onset of coherent enhancement of THz radiation is directly proportional to the bunch length. Figure 4.4 shows the coherent enhancement with a RMS bunch length of 0.6 ps. If the bunch length was longer, the enhancement would shift to higher frequency, and shorter bunch lengths would shift the onset of enhancement to a lower frequency.

The bunch compression occurs in the magnetic bunch compression chicane. Once the electron bunch has passed through the booster all the electrons in the bunch will be travelling at relativistic speeds. To maximize the possible compression in the chicane the main linac is set up in such a way to give the electron bunch an "energy chirp". To generate an "energy chirp" on the electron bunch the phase of the linac is set so that it is off crest, between 11-15°. Cresting the linac ensures that the electron bunch arrives at the same time as the main linacs RF is at its highest positive value, the dotted line in figure 4.5.

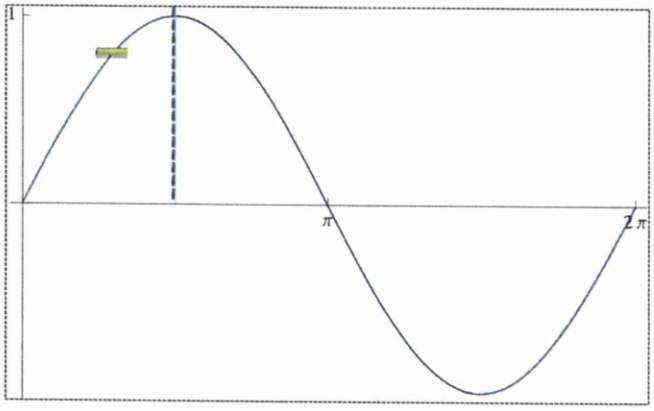

Figure 4.5. A figure to show the sine function of the Linac RF; the dotted line shows the on crest position, while the green box represents the electron bunch off phase.

When the electron bunch arrives at the linac, earlier than the RF crest, as shown by the green rectangle in figure 4.5, but exaggerated for ease of explanation, the front electrons of the bunch receive a lower energy, than the electrons at the back of the bunch. As the electrons are travelling at relativistic speeds it is energy that changes, but not speed since the main linac does not accelerate the electrons; this is described as giving the bunch an "energy chirp".

The "energy chirp" is important in optimising the bunch compression in the compression chicane. The electrons at the front of the bunch with, lower energy are deflected more by the magnets in the chicane and therefore take a longer path through the chicane than those at the back of the bunch with higher energy, which are deflected less by the magnets in the chicane, thus taking the shortest route. This results in the maximum bunch compression at the fourth dipole, of the compression chicane, where the THz emission will be at its maximum.

4.2.3 The THz Radiation Beam Transport System

The THz beam transport system transports the THz radiation from the diamond window, of the ALICE accelerator, to the diagnostic room and then to the tissue culture facility. It is important to note that the building was not specifically built to house ALICE and this has resulted in a lack of flexibility of the positioning of the optics to direct the THz radiation.

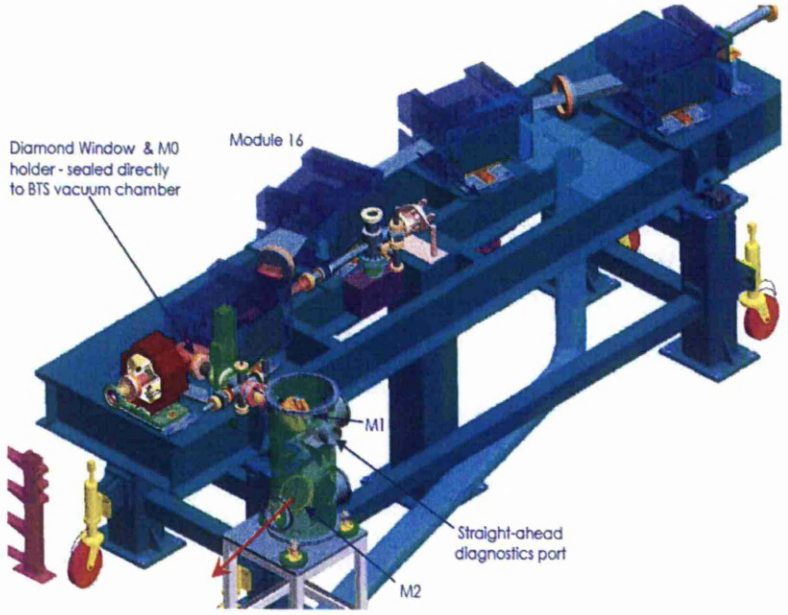

Figure 4.6. ALICE beam line chicane, with diamond window and start of THz beam transport system.

The THz radiation is collected from the chicane by the mirror M0 which is positioned just inside the accelerator, at a pressure of 10^{-9} mbar. M0 is a 50 mm diameter flat mirror that accepts up to 70 mRAD of the THz fan, as shown in figure 4.8. Figure 4.7 illustrates the final section of the compression chicane with the diamond window and mirror M0 indicated. The THz radiation is then transmitted through the 36 mm diamond wedged window, indicated in the diagram to the start of the THz beam line, which has a rough vacuum of 10^{-2} mbar.

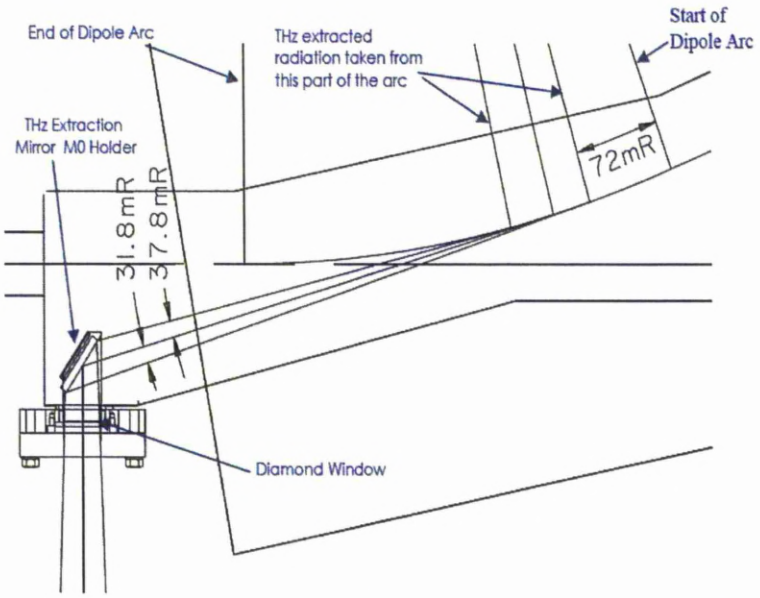

Figure 4.7. A schematic of the extraction of THz using mirror M0 collecting the THz from the arc created in dipole 4 of the chicane.

The THz light is then transmitted to the vessel containing the M1 and M2 mirror that is in the accelerator hall. M1 is a 6 inch focusing optic which deflects light down 400 mm to M2 which is a plane mirror with a 6 inch diameter. M2 directs the beam in a horizontal plain 15 degrees out from the ALICE accelerator straight at a height of 1000 mm from the accelerator hall floor. The M1 focus should be at around 3.6 m downstream in the beam pipe between mirrors M2 and M3, depending on the wavelength of the light.

Mirror M3 is the second focusing mirror in the beam line, it is a 6 inch diameter optic which turns the beam through a 45 degree angle, taking the light into a shielding wall labyrinth, towards mirror M4. The focusing nature of mirror M3 means it will focus at 5.2 m downstream in the beam line. Mirror M4 is a 90 degree turning plane mirror that takes the light into the diagnostics area, it has a diameter of 150 mm. M5 is the first mirror in the diagnostics area, and is a 200 mm diameter 90 degree turning mirror. The full layout of all the mirrors is shown in the schematic in figure 4.8.

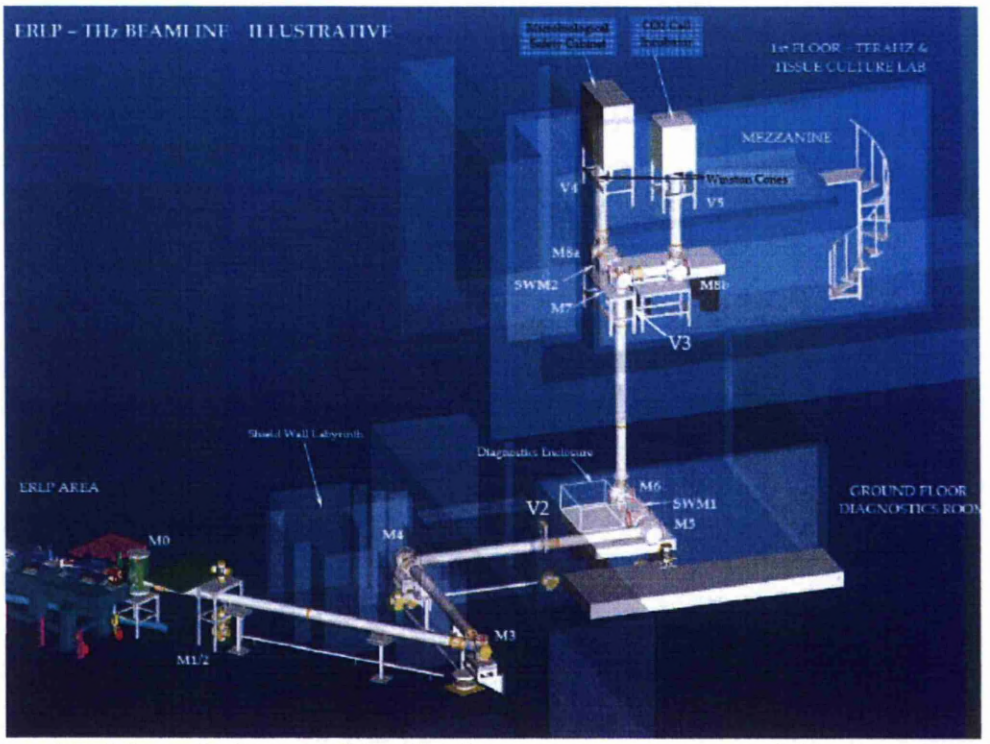

Figure 4.8. Schematic layout of the THz beam transport system . This shows the THz radiation transport system from the diamond window, at M0 through the labyrinth, into the diagnostics room and up to the TCF [4].

SWM1 is the first switch mirror, found between mirrors M5 and M6. It is housed in an ISO 5 way cross chamber and can be lowered into the position of the beam to take the THz radiation into the Martin Puplett spectrometer, shown as the diagnostics enclosure in figure 4.8. This will enable diagnostic work and FTIR experiments to be performed and allow a spectrum of the radiation to be generated. When SWM1 is translated vertically, out of the beam, it allows the THz radiation to continue from mirror M5 to M6, taking the light onward to the TCF. The TCF has two floors, the first floor has a diagnostics hutch, where a number of experiments will be performed from simple THz absorption experiments to more complicated pump probe experiments. These are yet to be performed and are not covered in this thesis. The second floor contains a microbiological safety cabinet and an incubator and is designed to allow cell experiments to be performed in their ideal conditions, as was mentioned earlier.

Mirror M6 is a 200 mm plane optic that works as a periscope mirror sending the light up 4400 mm to the mirror M7, which is found on the ground floor of the TCF. Mirror M7 is a 200 mm diameter plane mirror, which is a periscope receiving mirror than can be directed to send the light to mirrors M8a or M8b.

Prior to each of these mirrors is a position for a switch mirror that can direct radiation to any experimental or diagnostic equipment on the ground floor of the tissue TCF. Both mirrors M8a and M8b are 200 mm plane mirrors that deflect light up to the microbiology safety cabinet, via M8a, or into an incubator, via M8b, both situated in the TCF's second floor. At each of these opening apertures there is a TPX (Polymethylpentene) window, with a Winston cone used to help collect the flux near the focus for the THz wavelengths [4,5].

4.2.4 The THz radiation model of ALICE

The THz radiation of ALICE is generated in the chicane, shown in the figure 4.9. This section will consider the model used to gain theoretical information on the THz output to enable comparison with experimental measurements.

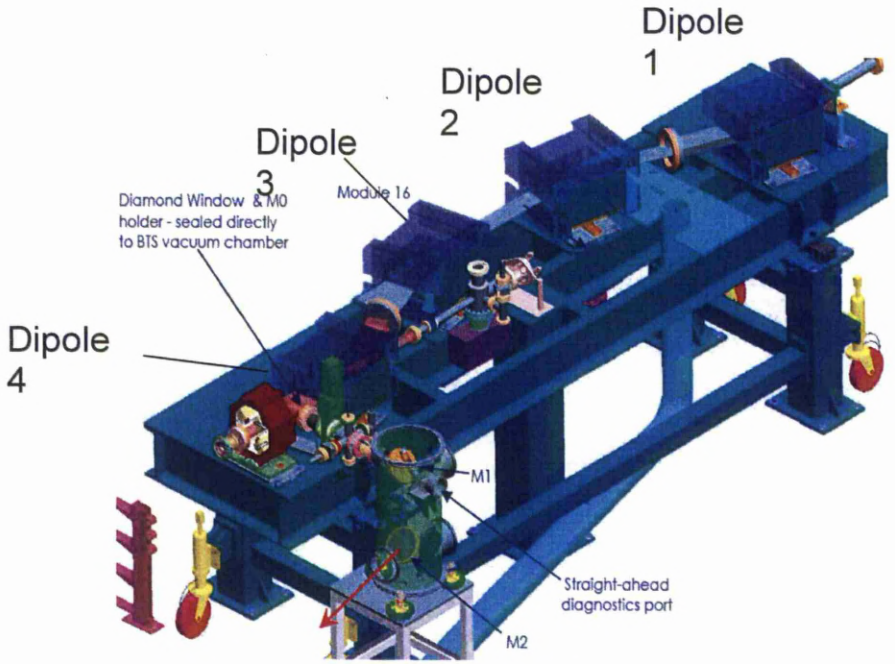

Figure 4.9. The chicane on ALICE, the source point of the THz radiation is in the fourth dipole. The green section is where the diamond window is located.

The source point of the THz radiation is the bending magnet radiation in the 4th dipole . The electron beam trajectory through the 4th dipole magnet is defined by the following parameters:-

Arc length = 410.25 mm

Angle of bend = 368.8 mRads

Radius of bend = 1112.25 mm

The distance from the centre of mirror M0 to the tangent point, with the source point 459.58 mm from the centre of mirror M0 [5].

With the radius of the bend, and the known electron charge it is possible to work out the power using the formula 4.1. Due to the electrons travelling at close to relativistic speeds, v can be considered the same as c, therefore the equation can be written as below.

$$\text{Relativistic Power (W)} = \frac{e^2 c\ \gamma^4}{6\pi\varepsilon_0\ r^2} \qquad \{4.2\}$$

e is the electron charge = 1.6 x 10^{-19}, c is the speed of light 3 x 10^8 ms^{-1}, γ is the relativistic ratio gamma, ε_0 is the permittivity of free space 8.85 x 10-12 Fm^{-1} and r is the bending radius 1.112 m. The following steps are required to calculate γ.

$$\text{Energy/electron on ERLP} = 35\text{ MeV} = 35\times1.6\times10^{-13}\ J = 5.6\times10^{-12}\ J$$

If we equate this to the total kinetic energy of the electron in the beam we get;

$$5.6\times10^{-12}\ J = m_0c^2(\gamma-1) \qquad \{4.3\}$$

Where m_0 is the rest mass of electron = 9.1 x 10^{-31} Kg. Therefore;

$$\gamma = \frac{5.6\times10^{-12}}{9.1\times10^{-31}\times(3\times10^{-8})^2} + 1 = 69.3$$

$$\text{Therefore } P = \frac{(1.6\times10^{-19})^2\times3\times10^8\times69.3^4}{6\pi\times8.85\times10^{-12}\times1.112^2} = 8.5\times10^{-13}\ W$$

This is the calculated power per electron. To calculate the THz power generated at ALICE, the coherent enhancement must be considered. As mentioned previously, if the wavelength of radiation is greater than the bunch length, coherent enhancement, each pulse radiates as N^2, where N is the number of electrons. The design bunch charge at ALICE is 80 pC.

$$\text{N= bunch charge (coulomb)}\times6.24\times10^{-18} = 80\times10^{12}\times6.24\times10^{-18} = 5\times10^8$$

Therefore the bunch instantaneous power becomes,

$$8.5\times10^{-13}\times(5\times10^8)^2 = 212\ kW$$

The model used is based on the analysis discussed in section 2 of "The Science and Technology of Undulators and Wigglers" by James Clarke, a member of the Daresbury staff [6]. For convenience the model is set up in Microsoft Excel

allowing numerous parameters to be inputted by the user to enable changes in accelerator settings (including beam energy, bunch charge, bunch length, train length and machine rep rate). The model calculates the output of THz radiation from dipole 4 based on the inputted conditions. This can then be used to evaluate the effects of the acceptance of mirror M0, the window transmission and any other relevant factors.

In the development of the model, certain assumptions were made, one crucial one was that the electron bunch would have a Gaussian distribution, this is considered to be a good basic model, however there is work to improve the model by using experimental bunches. But since this is yet to be completed the Gaussian bunch is taken as an estimate.

With the machine condition parameters set to 35 MeV, 80 pC, a machine rep rate of 20 Hz, with 100 μsecs train lengths and a bunch length of 0.6 ps RMS, the specification of ALICE in the design phase gives an average power of 0.34 mW/mrad with a peak power of 1.5 kW/mrad. The expected spectrum of THz for these conditions is shown in figure 4.10. Note that spectrum has a Gaussian distribution due to the calculation assuming a Gaussian electron density distribution within the electron bunch.

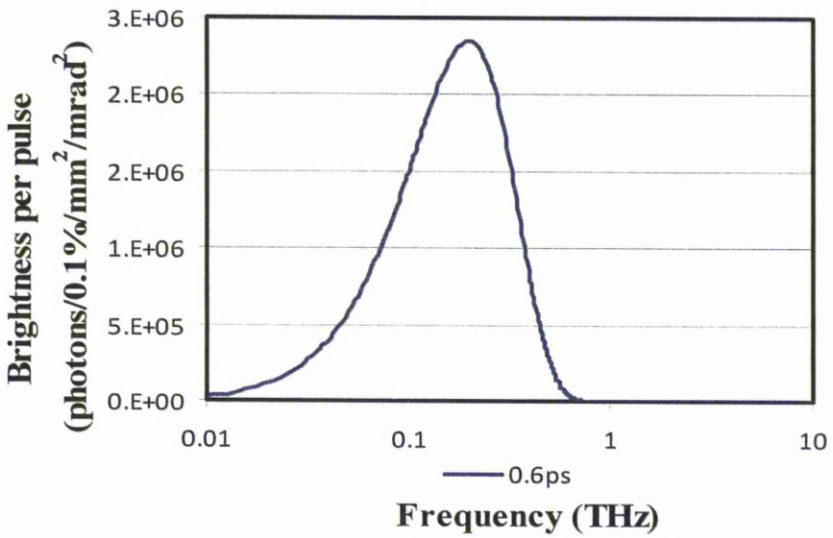

Figure 4.10. This shows the theoretical output from the calculation for the brightness per Pulse of THz generated by ALICE at 35 MeV, 80 pC, 20 Hz, 100 μsecs and 0.6 ps RMS.

Figure 4.11 shows the effect of coherent enhancement on THz production. The calculation accounts for this enhancement with the form factor, which takes the

RMS bunch length and clarifies whether it is shorter than the wavelength of light being emitted, resulting in the factor which can be used to calculate this enhancement.

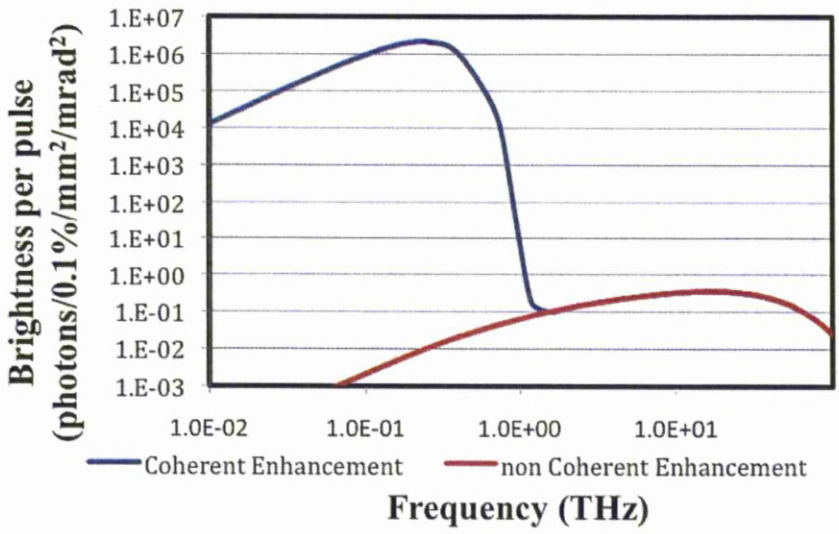

Figure 4.11. The Brightness per pulse of THz generated by ALICE at 35 MeV, 80 pC, 20 Hz, 100 μsecs and 0.6 ps RMS, with Log scale, showing the affect of coherent enhancement (note log scale).

The red line, in figure 4.11 shows the THz production with no coherent enhancement, this illustrates the poor performance with conventional synchrotrons in generating THz radiation. The blue line shows the affect of coherent enhancement, which occurs when the length of the bunch is shorter than the wavelength of light it is emitting. The onset of the increase in brightness is linked directly the bunch length, as shown in figure 4.12.

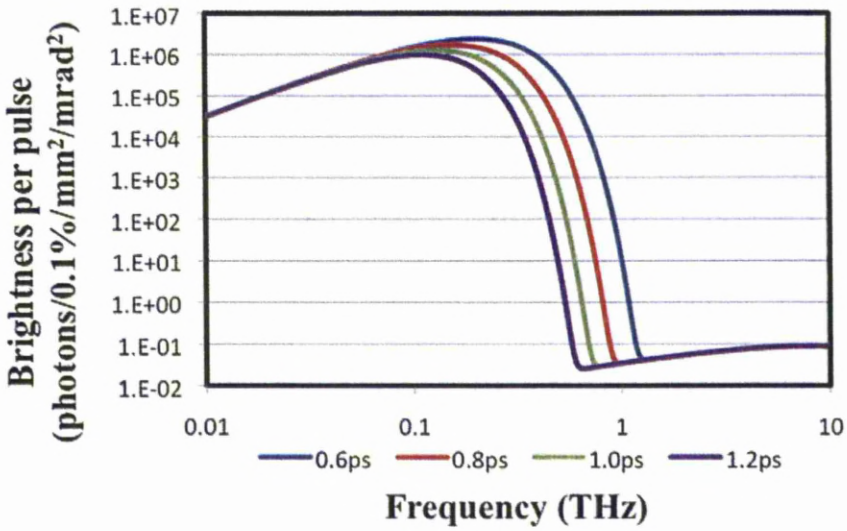

Figure 4.12. The Brightness per pulse of THz generated by ALICE at 35 MeV, 80 pC, 20 Hz, 100 μsecs and 0.6 ps RMS, with Log scale, showing the affect of RMS bunch length on the onset of coherent enhancement (note log scale).

Figure 4.12 shows the theoretical affect of change in RMS bunch length on the onset of coherent enhancement of the THz brightness. It is expected that the optimum bunch compression of the electron bunch in ALICE is 0.6 ps RMS, which theoretically would give an enhancement at greater than 1 THz. Consequently this demonstrates that bunch length plays a major role, not only of the spectra in the THz spectrum, but also the power emitted. The power law, shown in both figures 4.11 and 4.12, is 1/3. This is a known power law distribution of energies, producing a power law emission. This is a recognized value and is built into the calculations built by James Clarke and demonstrated in his book [6].

Table 4.1 shows the dependence of the average and peak powers observed theoretically, with any changes in RMS bunch length as all other parameters are maintained (beam energy 35 MeV, bunch charge 80 pC, rep rate 20 Hz, and train length 100 μsecs).

Table 4.1. The affect of RMS bunch length on Average and Peak power of THz emitted (these are theoretical values).

RMS Bunch Length (ps)	Average Power (mW)	Peak Power (KW)
1.2	6.86	15.19
1.0	8.33	23.03
0.8	11.76	38.71
0.6	16.66	73.99
0.5	21.39	112.03
0.4	28.38	185.84
0.3	40.67	356.72
0.2	70.92	1,005.88

The spectral information given in table 4.1 is expected to be comparable with experiments. They are displayed in the figure 4.13. The drop off in power is greatest between 0.3-0.8 ps, which is due to the onset of the coherent enhancement region as shown in figure 4.12. In this case the relationship between peak power and average power are shown to be very similar. However if the average powers become a concern, this is unlikely as they are so small, it is possible to change the timing structure of the ALICE accelerator, and maintain the high peak power, while lowering the average power further.

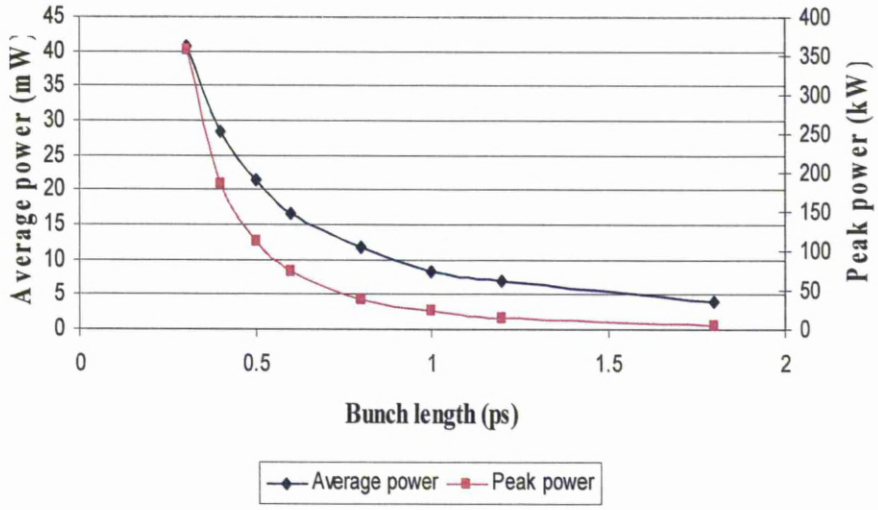

Figure 4.13 The affect of RMS bunch length on Average and Peak power of THz emitted (these are theoretical values)

To calculate the expected output of the ALICE accelerator, for comparison, there are a number of other paramaters that must be considered. These factors are determined by the THz emittance from the arc, the angle of acceptance of mirror M0, the vertical acceptance of the diamond window, the transmission of THz light and the efficiency of the transport system. These parameters are shown below;

- Mirror M0 vertical acceptance is 82 mRads
- The vertical acceptance of the vessel housing the diamond window is 72 mRads.
- From this it is suggested a cone angle of 70 mRads is acceptable for the model.
- The diamond window transmission is 0.7.

• The efficiency of the THz transport system from the diamond window to the diagnostics room is 0.25 (though is dependant on wavelength). Transporting the THz from the diagnostics room to the tissue culture facility has an efficiency of 0.5 [5].

With the addition of these parameters to the model, the theoretical values for the output of THz at ALICE seen at the diamond window with the machine settings 35 MeV, 80 pC, 20 Hz, 100 μsecs and 0.6 ps RMS, are an average power of 16.7 mW and a peak power of 74 kW.

4.3 Chronological History of Commissioning Work

The previous sections have described the design of the ALICE accelerator and THz beam line. This section gives a chronological account of the commissioning of the THz beam line, detailing some of the problems that had to be overcome in commissioning the THz capability on ALICE.

The ALICE accelerator, and the THz beam line are shown in figure 4.14. This shows where the THz leaves the ALICE accelerator and is directed via a number of mirrors, down the beam line held under vacuum, to the diagnostics room, and then transported to the tissue culture facility (not shown in figure 4.14).

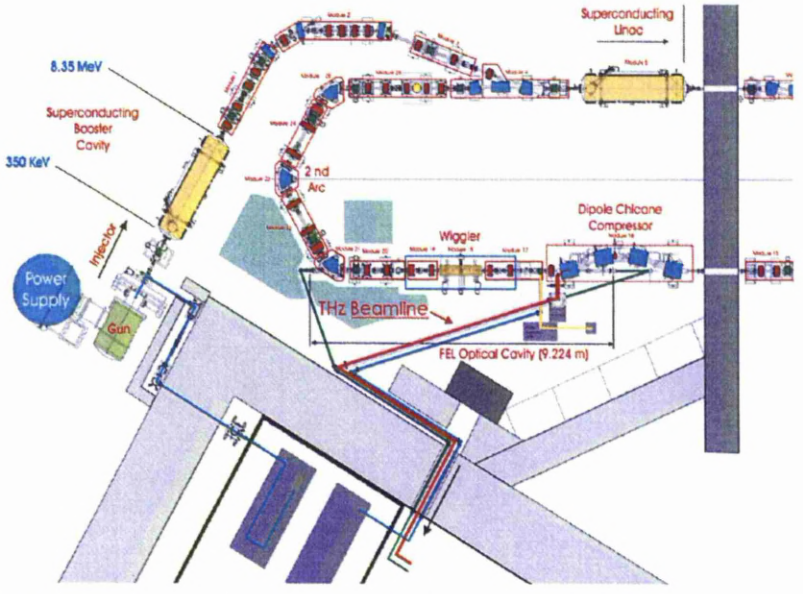

Figure 4.14. This schematic shows the dipole chicane compressor and the THz beam line with its direction through to the diagnostics room with the red line.

4.3.1 Early THz detection

The first step in commissioning the THz beam line involved the use of a HeNe laser to align the optical elements from the diamond window to the diagnostics room. The beam line was then pumped down to 0.01 mbar. The first THz signal was detected in the diagnostics room with the liquid helium bolometer in January 2009. This demonstrated that the ALICE accelerator was producing short electron bunches. It was hoped the THz beam line could then be used as a diagnostic tool to test the performance of the accelerator. However it was not possible to determine the power level as the detector had not been calibrated, so the units were arbitrary. The production and detection of THz was seen as a significant achievement, with energy recovery only having been achieved one month earlier at the end of 2008.

In February 2009, a further investigation into the characteristics of the THz output of ALICE was completed. The aim was to maximise the THz signal by manipulating the mirrors of the THz beam line. The first test was to establish where the THz radiation was entering the Martin Puplett spectrometer, which is situated on the diagnostics table in the diagnostics room. The alignment with the HeNe laser indicated that the beam entered centrally, so it was assumed that the mirrors were aligned correctly. However further investigations were completed which involved placing a metal block of various shapes to block all but a quarter of the beam, to determine where it was entering the spectrometer. This suggested the beam was entering the spectrometer at the bottom left quarter of the aperture, as viewed from behind the beam.

To enable the THz radiation to be directed into the diagnostics room on axis, it was thought that the position of the switch mirror SWM1 needed to be reassessed. However this mirror was not motorised and required manipulation by hand meaning real time measurements were not possible. Between each measurement the vacuum in the beam line within the diagnostics room had to be let up to air, a port on the beam line needed to be removed and the mirror had to be manoeuvred by hand, before replacing the port and evacuating the beam line. This procedure had no effect on the signal, which could be due to the vibrations arising from the evacuation and letting up to air negating the effects of changing the mirror alignment. Consequently it was decided to have this mirror motorised for movement in the x and y direction, which gave rise to left/right and up/down translation. Varying the vertical position of the mirror SWM1 ensured that the mirror was at the correct height.

The effects of the settings of the accelerator on the THz signal was then investigated and it was established that changes to the settings of ALICE had a huge affect on the THz signal. However, rather surprisingly the detailed steering of the electron bunch through the chicane, which changes the source position of the THz, seemed to have little or no affect on the THz signal received in the diagnostics room.

4.3.2 Initial Results

As a result of this early experience of commissioning the THz beam line it was decided that a number of mirrors would need to be motorised along the THz beam line during the next shutdown. At this time the understanding of the performance of the ALICE accelerator in general was limited and with settings that produced good energy recovery, or good THz, on one day failing to reproduce the same results the following day. There were also a number of issues with the performance of the gun which delayed things as the machine had to be run at lower settings, so further THz work was limited prior to the early year shutdown in March 2009.

The shutdown was extended due to issues with the RF allowing time to check a number of issues relevant to the commissioning of the THz beam line. The alignment of the mirrors was rechecked with the HeNe laser in air from the diamond window to the diagnostics room. This was possible as the centres of the mirrors are polished allowing optical wavelengths to be reflected with the outer parts of the mirrors being far rougher, as they do not need to be highly polished in order to reflect longer wavelengths. This was performed in a stepwise manner, ensuring the light was at the centre of the mirror M1, before moving to mirror M2 and working through methodically. This alignment was then checked by relocating the laser in the diagnostics room and shining the light back towards the centre of the diamond window. This alignment achieved a high level of accuracy. Overall, very little adjustment of the mirrors was required, to align the laser light, indicating that the low THz radiation signal observed, and its direction of entry into the Martin Puplett spectrometer was not due to misalignment of the optical components.

The HeNe laser was then moved back to the diamond window and the SWM1, that takes light into the Martin Puplett spectrometer, lifted so that it is out of line, allowing the laser to reach mirror M6, which takes the THz radiation up towards the tissue culture facility. The remaining mirrors were aligned in the same methodical manner as before so that the HeNe laser hit the centre of the TPX

windows in the incubator and the microbiological safety cabinet, utilising the switch mirror SWM2, and noting its position. The position of the light at the TPX windows did not change as a result of the beam line being evacuated, indicating that the mirrors did not move during the evacuation and letting up to air of the beam line. During the pumping down of the beam line it was noted that the TPX windows in both the biological safety cabinet and the incubator bowed slightly when under vacuum, this was noted and discussed in further meetings to discuss the possibility of using thicker TPX.

Ideally when aligning the beam line mirrors the HeNe laser should be located at the source point of the THz, however, this is not possible since the source point is in the accelerator vessel and is not accessible. Also the effective source point is dependant on the electron beam position in the beam pipe, and therefore is likely to change. Therefore the presumption that the THz is leaving the diamond window at the original simulated angle and direction is assumed, and the laser shone from the diamond window at this angle.

It was hoped that by motorising the mirrors in the beam line it would be possible to make allowances for small variations in the direction that the THz left the diamond window, by making small changes to the mirrors and monitoring the signal in real time in an attempt to maximise the signal. This is important, as mirrors M1, M2 and M3 are not accessible to be moved manually when ALICE is running, requiring access on limited access, resulting in no ability to perform real time measurements or small alterations during beam running. The mirrors in the diagnostics room can be altered, manually without the need for limited access, however no real time measurements can be taken until they were motorised, due to the requirement to bring the beamline up to atmospheric pressure, open the beamline and move the mirrors, before then re-evacuating and taking another measurement.

It was considered that the cause of the THz signal entering the diagnostics area on the bottom left corner, and the lack any effect of steering observed on the bolometer in the diagnostics room, was most likely to be due to the position of the source, and the direction in which the THz leaves the diamond window. With the current design, it is not possible to manoeuvre manually or via motors mirror M0 which sits in the accelerator. It was therefore decided that the long term solution to this issue was to develop an improved dipole vessel to house a motorised movable mirror. This will be discussed later in this chapter.

The next step was to clarify whether mirror M0 was in the correct position relative to the source position. Mirror M0 had been positioned in order to accept the maximum cone angle of THz from a source position that had been calculated from a theoretical understanding of the trajectory of the electrons through the chicane. Ben Shepherd, of Daresbury, calculated the trajectory of the electrons through the beam line with respect to the magnets, using experimental data from the accelerator and this was plotted against the survey drawings. This demonstrated that the path the electrons take experimentally, and minor alterations of this to allowing for error, do not match up with those of the ideal theoretical path. This indicated that the source point of the THz is likely to be in a different position to the original specification, and consequently the mirror M0 may not be in the correct position. As a result of this uncertainty it was decided that a study of how the THz leaves the diamond window was required. Previously THz radiation had been detected with a bolometer in the diagnostics room. The bolometer is used at sub-millimeter wavelengths and is the most sensitive detector available, however to achieve this sensitivity the bolometer has to be cooled using liquid helium and held under vacuum. This makes the bolometer immobile and unsuitable for spatial mapping of the output from the diamond window. As a result it was decided to source a Thomas Keating Power Meter to detect THz radiation at the output from the diamond window (a detailed description of all detectors is in chapter 2). The detector is calibrated to show a signal of 1 mV for every 1 μJ of radiation absorbed.

4.3.3 Measurements Near the Diamond Window

In early August 2009 the power meter was placed at a position 300 mm from the diamond window, with a beam pipe (3 inches) between the diamond window and the detector. The beam pipe was terminated with a TPX window allowing a low vacuum to be maintained along the 300 mm pipe. Once the machine was running at 21 MeV and 20 pC with 100 μsec train length, a little manipulating of the machine settings by the accelerator physicists produced a signal of between 10-15 mV on the power meter. Figure 4.15 shows the output of the detector with no signal, just noise, on the left and then with the THz signal on the right. The yellow peak, on the bottom left of each trace is the laser trigger pulse.

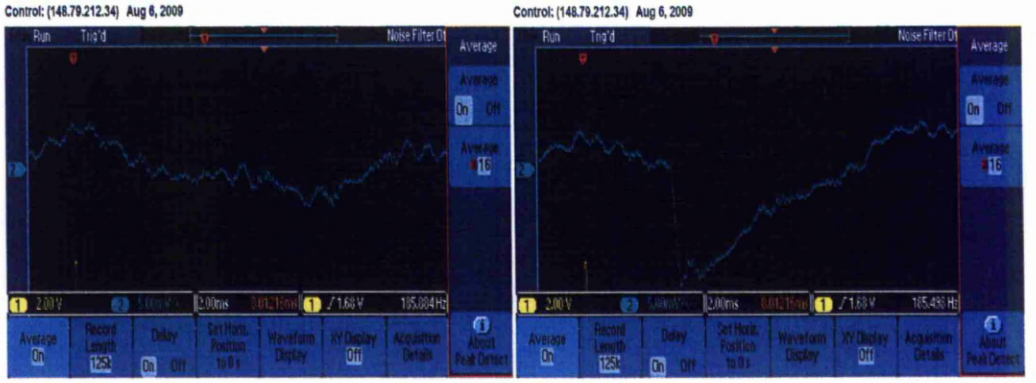

Figure 4.15. Power Meter with no beam on left and beam on right, the scale is 5 mV per vertical division. The yellow peak is the laser trigger pulse.

This was the first time a THz signal had been observed on a calibrated detector and it indicated that 10-15 μJ of THz radiation was being observed 300 mm from the diamond window. Theoretical analysis indicated that a 0.6 ps RMS bunch length would give rise to a THz signal of 42 μJ. If the lower than expected signal was due to the length of the bunch, this would indicate a bunch length of 1.3-1.8 ps. The signal to noise ratio shown in figure 4.14 is poor and the signal level was also unstable (the figure changed 2-3 μJ between measurements), making it difficult to use this signal to fine tune the accelerator, or the THz beam line mirrors.

In order to improve the signal to noise ratio new cabling with better insulation was installed and the amplifier was moved closer to the detector. Lead shielding walls were installed around the detector and preamplifier in an attempt to minimise any affect of the intense X-rays produced by the linac, and beam losses in the accelerator hall.

4.3.4 Unusually Large THz Signal

In the following days further experiments were performed in an effort to maximise the THz signal and further understand the accelerator conditions required for strong signals. The machine was set up at 21 MeV, 30 pC and 100 μsecs train length and a considerable signal was achieved, as shown in figure 4.15, of 130 mV (130 μJ) with significantly reduced signal to noise (shown on left of figure 4.16). The accelerator settings were repeated in the following shift on the same day and a signal of up to 150 mV (150 μJ) was observed, shown on the right of figure 4.16.

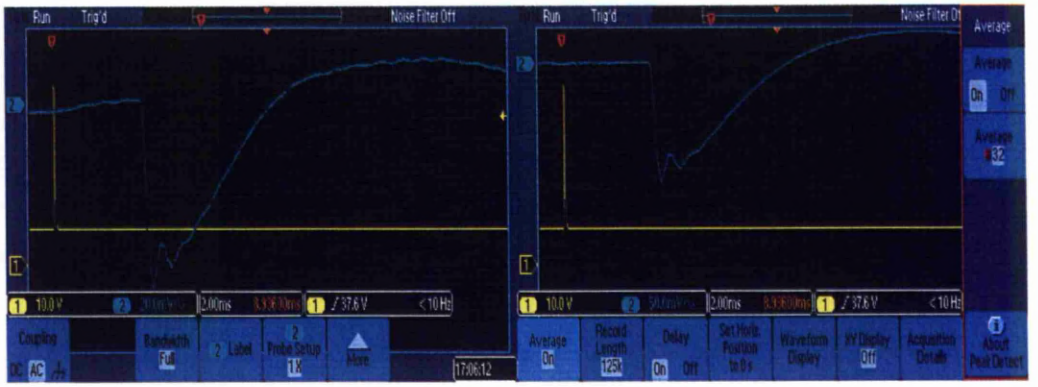

Figure 4.16 Large THz signal 130 mV on left and 150 mV on right. (note change of scale).

The results of the theoretical analysis, as described in previously [The THz radiation model of ALICE], indicate that these accelerator settings should yield 94 μJ of THz radiation, when the bunch length is 0.6 ps. The THz signal observed indicates a bunch length of between 0.4-0.5 ps RMS. 0.6 ps RMS is predicted to be the optimum compression possible in the ALICE accelerator, so the large signal could be due to instability in the linac cavities that were occurring. It is possible that this instability could be creating artificially short bunches, by forcing the electron bunch density into a small pocket of the train. Sadly, the settings of the machine seemed to be very unusual, and despite attempts being made, it has not been possible to reproduce a machine set up that produces such a strong, and unexpected, signal.

4.3.5 Attempt to Monitor THz Radiation in the TCF

Having established the accelerator conditions necessary to achieve a strong and stable THz signal, close to the diamond window, the next experiment was to measure a signal with the use of a power meter in the microbiological safety cabinet of the TCF. The mirrors had previously been aligned using the HeNe laser, so it was believed that a signal, even if small would reach the TCF. The power meter uses a microphone for detection, and so is susceptible to acoustic noise as well as radiation. When placed in the accelerator hall, there is a contribution to the noise from the mains electricity as the machine running at 10 Hz is a divisible of the mains frequency of 50 Hz. However the TCF has far less acoustical noise in comparison to the accelerator hall, and there are far fewer electrical systems running in close proximity. Furthermore there is no danger of X-ray radiation in the TCF and so it was hoped that the signal to noise ratio would allow a signal to be identified. Sadly there was no signal observed, despite a number of changes to the accelerator settings

and to the mirror alignment. This was then followed by complex accelerator issues, which resulted in no further work being possible.

4.3.6 Actions Following Failure to Detect THz in the TCF and Diagnostics Room

It was unclear whether the lack of THz signal in the TCF was due to a lack of production of THz by ALICE, or a failure to transport along the THz beam line. At this stage the accelerator was still producing variations in THz signal, from day to day, despite the machine settings remaining constant. It was decided to redevelop the transport pipe of the THz beam line between the diamond window and the mirror M1M2 vessel. This modification could allow a switch mirror to be installed at the diamond window, with a permanent detector in place, to allow monitoring of the THz levels at the diamond window, before measuring at the diagnostics room. The redesigned mirror vessel has been constructed and was installed in February 2011, it installation and commissioning is discussed in the final section of this chapter.

4.3.7 Relationship Between THz Production and Beam Physics

4.3.7.1 Energy Recovery

In order to explore whether the accelerator could be operated in energy recovery mode and still generate intense THz radiation, a test was performed with the power meter situated close to the diamond window. It was felt that there may be a difference in the bunch distribution exiting the linac dependant on energy recovery.

The machine settings were 20 pC, 21 MeV and 80 μsecs train length with a THz signal of 5 μJ. The signal was lower than expected with these beam settings (22 μJ expected with a 1 ps RMS bunch length) however there was no change whether there was energy recovery or not, as shown in figure 4.17. To stop energy recovery, a pop in dump (PID) is moved into the beam path and is located at the end of arc 2. This can only be performed for a short time, before you risk induced activity in the pop in dump.

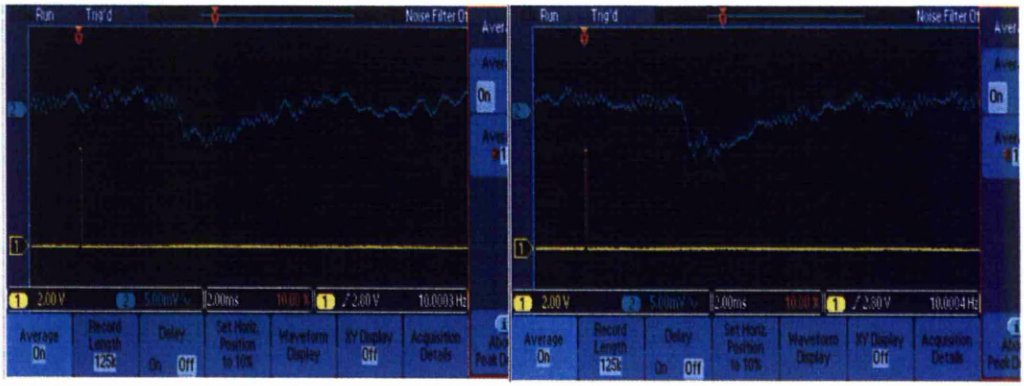

Figure 4.17. This shows the THz seen at the diamond window, with energy recovery on the left, and no energy recovery on the right, each vertical division is 5 mV.

4.3.7.2 Beam Steering

The affect of beam steering on the production of THz was also monitored. The beam was steered through the chicane to acceptable extremes with no major difference in THz generation. However when DIP-03 (3^{rd} dipole in the chicane) was altered by a large amount a positive signal was seen. This positive signal, 10 mV in amplitude, shown in figure 4.18, has a very similar shape to the negative THz signal. It was assumed that the change in sign was being generated from an X-ray bombardment on the detector. The power meter works by a microphone sensing a pressure difference in the gas contained between two transparent films. Consequently a positive signal is not possible unless it is thought to be due to an affect of the X-rays on the electronics. To test the hypothesis the electron beam was crashed into the walls of the chicane prior to the diamond window, generating a large amount of X-rays and having no electron beam compressed further in the chicane to provide a THz source. This resulted in a large positive signal being seen on the detector, therefore proving that the positive affect on the detector was due to the influence of the X-rays.

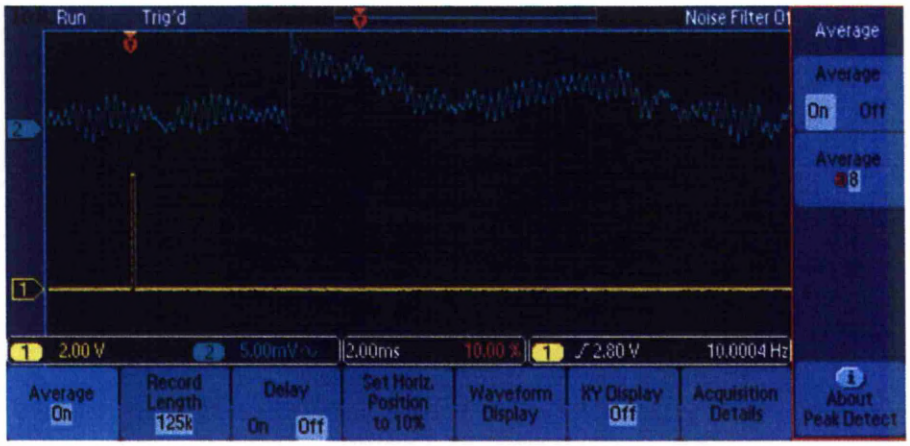

Figure 4.18. This shows the positive THz signal, when the beam is steered massively at DIP-03, one division vertically is 5 mV.

4.3.7.2.1 Further Study of X-ray Effect with Pyroelectric Detector (later in year)

Later in the year with the new pyroelectric detector sourced, it was decided to re-evaluate the X-ray effect that had previously been observed. The first spectra in figure 4.19 shows a THz signal seen on the pyroelectric detector. Once this signal was stable, the accelerator physicists inserted four screens (usually used for monitoring beam position) prior to the chicane, which disturbed the electron beam, resulting in massive beam losses and no electron beam passing through the chicane. The middle image on figure 4.19 shows a negative signal observed on the detector, which must be resulting from the X-rays generated by the electrons hitting the sides of the beam pipe, as it was not possible for THz radiation to be generated.

The next step was to remove all the screens and insert one in arc 1, thus increasing the distance from the detector of the X-ray generation, resulting in the electron beam crashing into the beam pipe further away from the chicane and the detector, with no chance of THz generation, this resulted in the third spectra in figure 4.19, with a small but still negative signal. This confirms that the change in signal on the detector is due to the generation of X-rays, and the signal is true X-rays, rather than a summation of a positive THz signal and a negative X-ray signal.

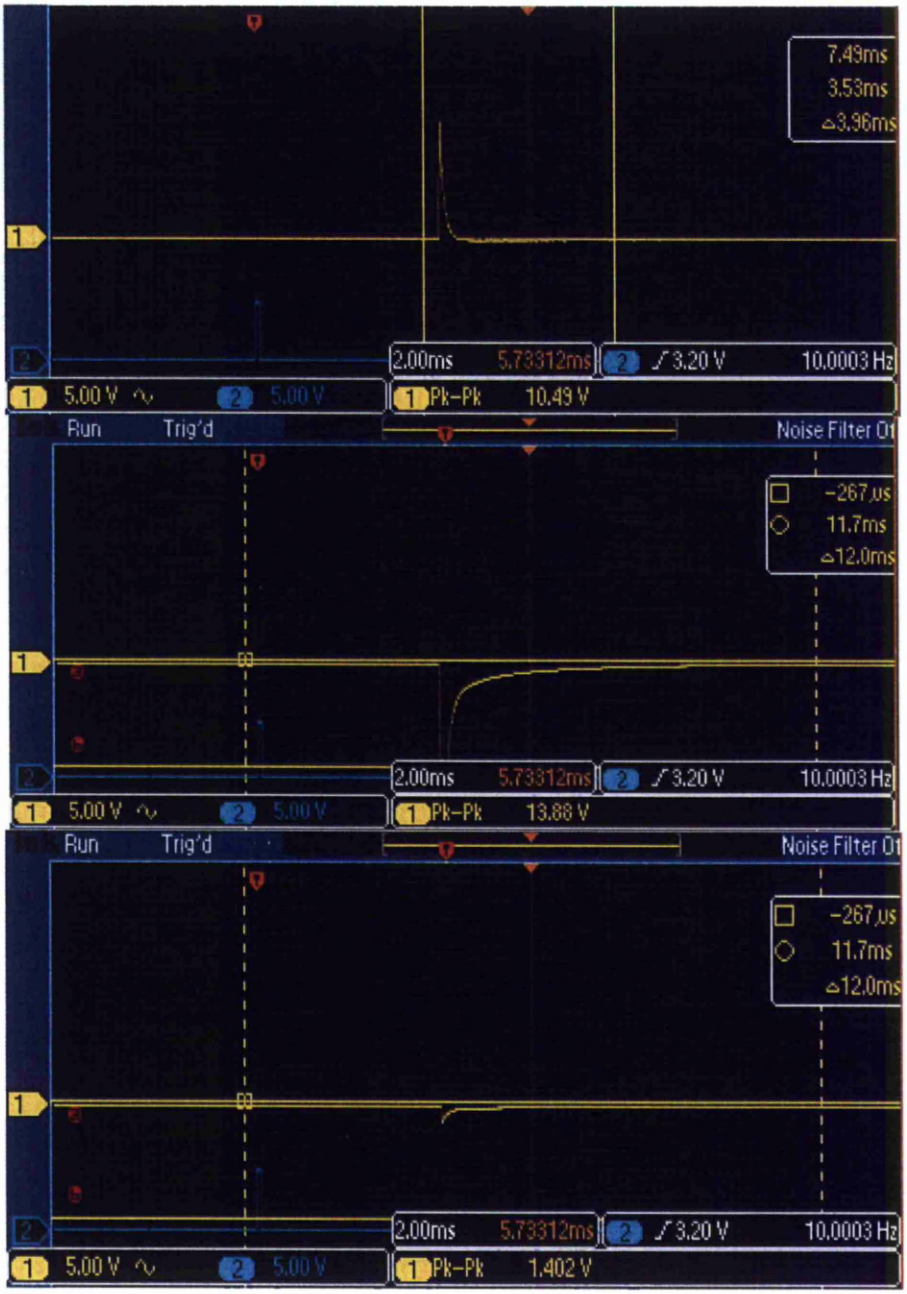

Figure 4.19. The pyroelectric detector response. The top spectra show a normal THz signal seen, the middle spectra shows the negative peak, believed to be X-rays, with the bottom image showing a smaller amount of X-ray radiation detected by the pyroelectric detector.

4.3.7.3 Train Length Dependence

The next experiment was to measure the effect of train length on the THz signal, the results are shown in figure 4.20. Theoretically it is expected that the THz signal will depend linearly on the train length. This is because the train length determines the amount of bunches. When ALICE is operated with 8125 bunches this gives a train

length of 100 μsecs. Based on theoretical evidence for the beam conditions set, and a 1 ps RMS bunch length the following is expected, 20 μsecs-5 μJ, 40 μsecs-11 μJ, 60 μsecs-16 μJ and 80 μsecs-21 μJ. Experimentally the THz observed was 20 μsecs-5 μJ, 40 μsecs-7.5 μJ, 60 μsecs-10 μJ and 80 μsecs-15 μJ.

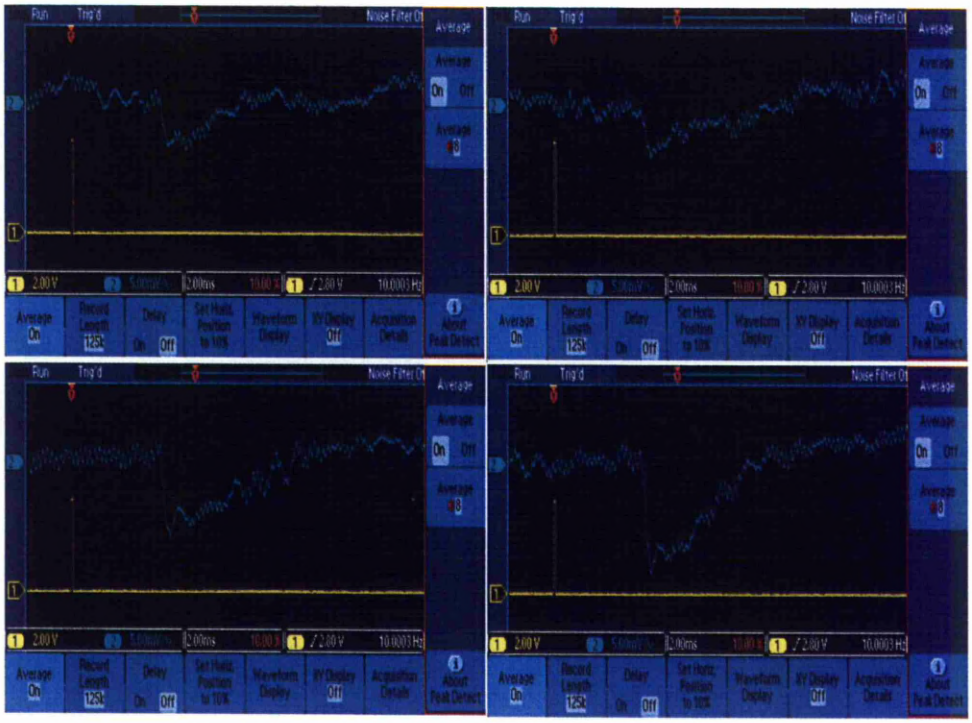

Figure 4.20. The effect of train length, 20 pC, 21 MeV, with 20 μsec top left, 40 μsec top right, 60 μsec bottom left and 80 μsec bottom right (each vertical interval is 5 mV).

These experimental results do appear to demonstrate a linear nature, however the signal observed at 80 μsecs, is slightly larger than expected, as shown in figure 4.21. This is thought to be because the beam line is set up to maximise the THz produced at long train lengths, and the experiment was performed with minimal changes made on beam settings and steering, with just the train length altered to establish the effect.

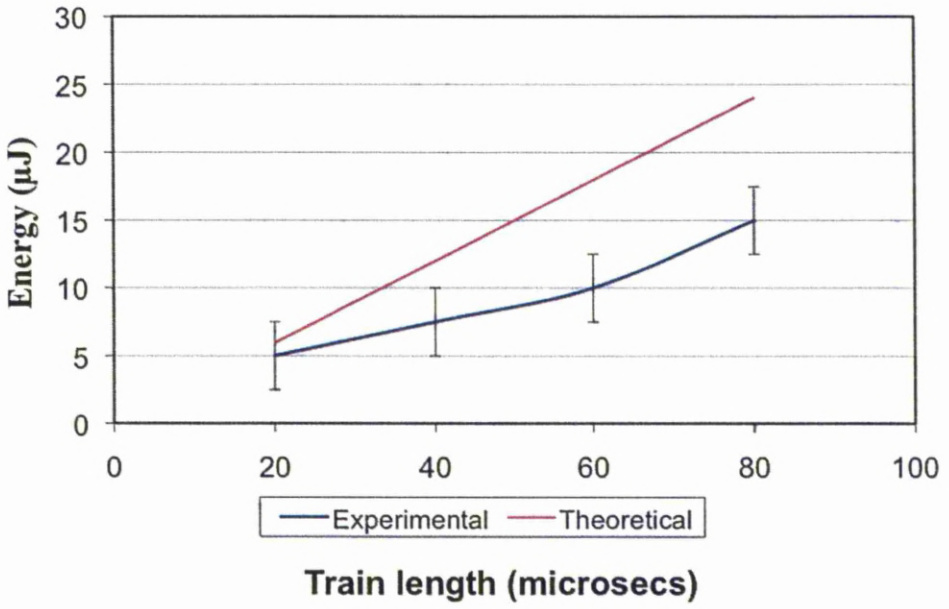

Figure 4.21. Effect of bunch charge on THz signal, comparisons between theoretical and experimental results. With an experimental error in the data of ± 2.5 μJ shown via the error bars.

This was repeated later in the year with a different detector and figure 4.22 illustrates the expected linear dependence of the THz signal as train length increases up to a train length of 60 μsecs where it is highly likely that the detector saturates.

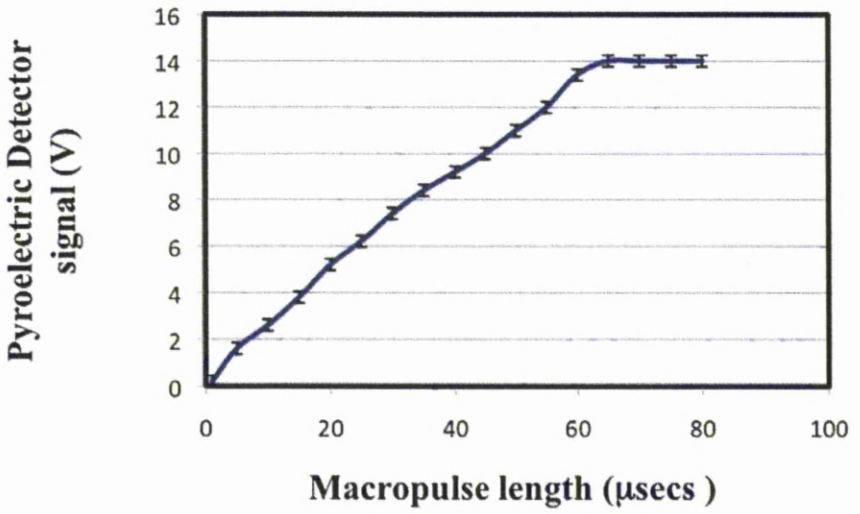

Figure 4.22. The effect of train length on THz, the vertical axis shows the pyroelectric detector response, in V that is arbitrary, and the horizontal is the train length (Macropulse length).

4.3.7.4 Effect of Bunch Charge on THz Signal

The final accelerator specific experiment was to measure the effect of the bunch charge on the THz signal close to the diamond window using the power meter. Theoretically this is expected to give a quadratic dependence, as shown in figure 4.23, however experimentally the results did not show this, at 20 pC the signal is roughly 5 μJ, and at 40 pC the signal is 10 μJ. It was not possible to understand why at this time, however it is clear the power levels being received are far lower than those that were theoretically predicted.

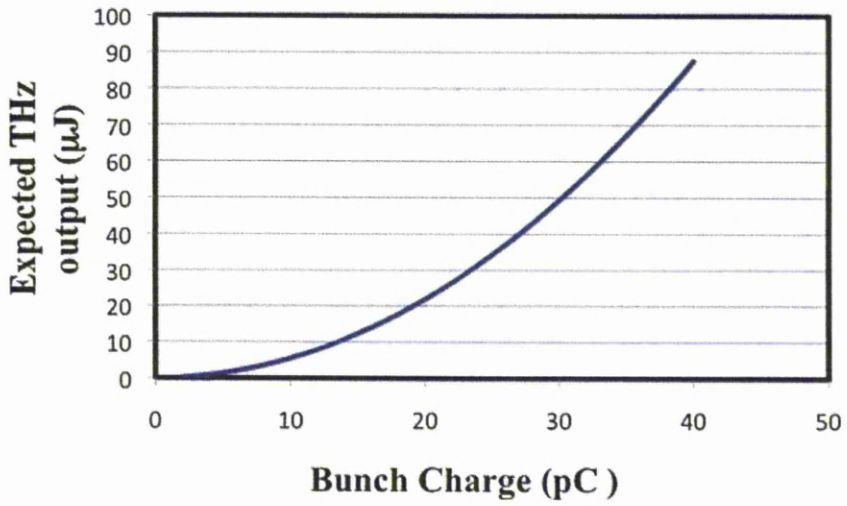

Figure 4.23. The theoretical affect of bunch charge on THz signal, there is a quadratic dependence.

4.3.8 Improvements to THz Signal Through Advances in Accelerator Settings

Close collaboration with the accelerator physicists enabled the THz signal to be used to monitor the improvements in the accelerator settings. With the detector placed close to the diamond window, the ALICE accelerator was set to 20 MeV and 20 pC with a rough signal of 15 mV seen on the detector. The signal was very stable and with a high level of energy recovery, it was decided to advance the accelerator settings by increasing the beam energy to 29.6 MeV and maintaining a bunch charge of 20 pC. With 100 μsec bunches a 30 μJ THz signal was observed, which would give a theoretical bunch length of 1ps RMS, (original specifications and target performance was 0.6 ps RMS giving a potential signal of 58 μJ). At this point there was no ability to experimentally measure bunch length.

Once a stable THz signal was seen, with stable energy recovery, it was decided to advance the bunch charge from 20 pC to 40 pC, resulting in the settings of the accelerator being 29.6 MeV, 40 pC and a train length of 50 μsecs. Due to the high bunch charge, it was not possible to run with train lengths much greater than 50 μsecs, due to beam loading on the RF systems of the main linac, however as there is a linear dependence on train length, and a quadratic one on bunch charge, it is still advantageous to run at higher bunch charge and lower train length. With full energy recovery a stable THz signal was observed on the power meter equating to 10 μJ, however when energy recovery was deliberately lost, by inserting the PID, which sits after the second arc before the return to the main linac, a signal of 20 μJ was observed. Theoretically the value should be 60 μJ with a 1 ps RMS bunch length, although this result would indicate a possible train length of 2.2 ps RMS if we were collecting the whole signal. However no matter what the actual bunch length is, it is clear that the THz signal has a dependence on whether there is energy recovery. This is an interesting result concerning the operation of ALICE that could arrive from the decelerated electrons. The likely explanation is described as beam loading, and can be solved by some changes to the accelerator RF systems.

An attempt was made to increase the bunch length to 60 μsecs, with a number of changes to the linac cavity gradients, buncher power and magnet energies required to maximise the signal. Once this was complete a maximum signal of 60 μJ was observed on the power meter, with a theoretical value expected at these conditions to be roughly 72 μJ, based on a 1 ps RMS bunch length. This result suggests, that if all the THz energy was being collated, the bunch length would be expected to be between 1.1-1.2 ps RMS. In later days it was possible to up the train length to 100 μsecs and a signal of 86 μJ was observed.

4.3.9 Realignment of the THz Beam Line

With the improvements in accelerator settings leading to strong and stable THz production it was decided to attempt to measure a signal in the diagnostics room. Due to the failure to see any signal in the diagnostics room with the power meter previously, it was decided to recheck the alignment of the THz beam line prior to any new experiments. Fortunately there was sufficient time for an extensive alignment process due to a major problem with the photoinjector laser of ALICE. This was first done by locating the HeNe laser in the diagnostics room and working back towards

the diamond window, one mirror at a time. This revealed that mirror M4 was considerably misaligned. This may have been due to a driver fault. This misalignment was corrected and, once all the mirrors were aligned, it was possible to see the light in the centre of the diamond window as shown in figure 4.24.

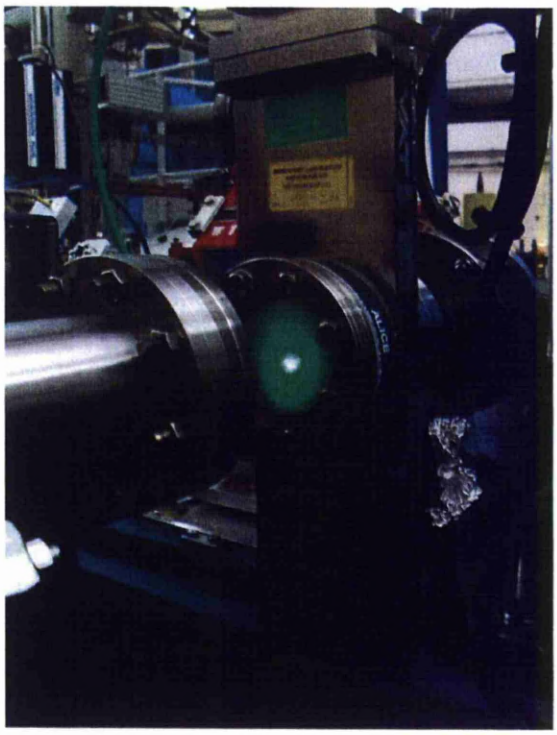

Figure 4.24. HeNe Laser aligned on the centre diamond window port from the diagnostics room.

The HeNe laser was then placed at the diamond window to confirm the mirrors to the TCF were aligned correctly. Once this was completed, a light bulb which is an incoherent source and as a result is a better model for the expected THz radiation, was first placed at the diamond window, and shone through to the diagnostics room. It was then moved to the diagnostics room and directed to the tissue culture facility, where the light could be seen clearly. Due to the rough polish of the mirrors giving light scatter at visible wavelengths and the weak light bulb source, it was not possible to detect the light from the TCF when the bulb was at the diamond window. The THz beam line was then pumped down in order to check that there was no change of the mirror positions during the pump down. The light was seen in both the microbiological safety cabinet and the incubator, although

subjectively this was at a slightly reduced intensity (measurements were subjective as measured by eye only).

4.3.10 Detection of THz in the Diagnostics Room

An important step in both characterising the beam line and the THz is to transport the THz to the diagnostics room to allow the spectrum to be measured. In a preliminary experiment the power meter was used to detect the THz output close to the diamond window, with a stable signal of 10-20 mV. The power meter was then removed, under limited access, and the beam line reconnected to allow THz radiation to be transported to the diagnostics room. The signal measured using the bolometer in the diagnostics room (currently in arbitrary units) was 2, and with some accelerator adjustments and an adjustment of the THz beam line mirrors the signal was increased to 5. The bolometer was then replace by the power meter in the diagnostics room, in the Martin Puplett spectrometer and no signal was observed. The beam line mirrors were scanned in an attempt to achieve a signal but it was not possible to achieve a signal.

In seeking to understand the discrepancy between the readings on the bolometer and the power meter, the THz transport system was checked by eye to ensure all the mirrors were operational. This indicated a misalignment of mirror M2. The mirror holder had lost a ball bearing that is required for the mirror motors to work. This is likely to have happened if the mirror was driven too far in one direction, which may have happened when it was scanned for a signal when the power meter was in the diagnostics room. This was fixed and the mirror realigned by eye. It was therefore considered that this may have played a crucial role in the lack of signal observed with the power meter, and so the experiment was to be repeated. All mirror driver limits were noted to ensure this error would not happen again.

Over the next few days a regular signal of up to 30 mV (30 μJ) was monitored using the power meter close to the diamond window for beam conditions of 29.6 MeV, 40 pC and 40 μsecs train length. This corresponds to an expected theoretical result of 48 μJ for a bunch 1 ps RMS in length. With the accelerator generating THz at a more consistent level, it was again attempted to measure the signal being received in the diagnostics room. The bolometer was prepared and immediately a signal of 2-3 arbitrary units was observed with a train length of 50 μsecs. Mirrors M2 and M4 were then scanned in both horizontal and vertical

directions in an attempt to increase the signal however this did not result in any evident improvements. The accelerator settings were then adjusted and a signal value of 4 was achieved. Again the mirrors were scanned to ensure this was the optimal signal possible.

The power meter was then placed in the position of the bolometer in an attempt to quantity the signal being received. A very small signal was observed, although only once the detector amplifier gain was increase to 20 dB (decibel), representing a signal of 0.05 μJ. With the train length increased to 100 μsecs, the signal doubled to 0.1 μJ, however the signal to noise level ratio was still very small so it was considered impossible to optimise the beam line at these current levels.

4.3.11 Power Meter Between M2 and M3

In an attempt to gain a better understanding of the transmission of the THz radiation along the beam line, the power meter was moved to a position between the mirrors M2 and M3, at the rough focus position of mirror M1. In order to do this a polythene window, which transmits for wavelengths below ~ 15.4 μm, was mounted between the two mirrors were a piece of pipe had been removed to allow the power meter to be located. The machine was setup with the same settings that had seen the 0.05 μJ signal in the diagnostics room (29.6 MeV, 40 pC and 50 μsecs). This generated signals observed close to the diamond window of 30-40 μJ, with a theoretical value of 50 μJ expected (close to the diamond window). The signal detected on the power meter in the position between mirrors M2 and M3 was 5 mV = 5 μJ. This suggests, based on previous results that there is a loss of up to 4.95 μJ between mirror M3 and the diagnostics room, and 25-35 μJ between M2 and the position close to the diamond window.

Alternatively the THz beam may be very divergent at the point where the detector was positioned between mirror M2 and M3. The active area of the power meter, is 60x40 mm. Mirror M0 is a focusing mirror and the focus should be at the point where the detector was placed, however if the light were not hitting the mirror as designed, then the beam would be more divergent and the focus shifted. It is therefore possible that the THz radiation beam is larger than the active area, so the full signal is not collected.

4.3.12 Mirror M1M2 Vessel Chamber

In order to understand the loss of THz signal between close to the diamond window and the position between mirror M2 and M3, it was decided to explore the signal being received in the M1M2 vessel. The detector was first positioned at the diamond window where a signal of 10 μJ was observed. The air was then evacuated from the small pipe between the window and the power meter at the entrance to the M1M2 vessel, and the signal was still 10 μJ. The detector was then positioned in the M1M2 vessel, without any pipe work between the M1M2 vessel and the diamond window and no signal was observed on the power meter. This indicates that none of the THz was directed from mirror M0 on axis towards the M1M2 vessel as was expected, suggesting that any signal that had been received previously past the M1M2 vessel had only been after multiple reflections along the inside of the beam pipe. This would mean that any transmission further down the THz transport system would be improbable and suffer huge loses.

4.3.13 Discussion to Perform Front-End Study

It was clear from previous work that it was important to characterize the geometrical profile and propagation direction of the THz leaving the diamond window. It was felt that once this was performed, it would be possible to make small alterations to both the ALICE accelerator conditions and THz transport system to transport the THz to the diagnostics room and TCF. A replica of the mirror M0, which is the mirror located in the accelerator in a fixed position was obtained. This was used in experiments with a microwave source at the University of Liverpool, and was determined to be working as was expected in the design. A number of filters were also sourced to allow a study of the THz signal and beam profile at different wavelengths. This would allow us to gain more information on the THz radiation as it left the diamond window, and compare it to theoretical models.

4.3.14 Initial Experiment to Measure the THz Intensity at the Diamond Window

To enable the THz intensity to be measured at the diamond window the beam pipe between the diamond window and the mirror M1M2 vessel was removed and the power meter was placed next to the diamond window. A THz signal of 36 μJ was observed with the accelerator settings of 30 MeV, 30 pC and 60 μsec train length. A signal of 57 μJ was observed when the train length was increased to 100 μsecs.

These results demonstrated a linear response of the THz signal to train length that would be expected theoretically. Furthermore when a reflective metallic pipe was inserted between the diamond window and the power meter, the signal increased thus supporting the belief that the THz radiation was being emitted with a large divergence, which was then collected by the reflective pipe.

A further experiment was performed in an attempt to monitor the affect of bunch charge on the THz signal with a polythene filter (transmits wavelengths below ~15.4 μm – 20 THz) in place of the beam, and without it. As discussed earlier, it is expected theoretically that the THz signal will depend quadratically on the bunch charge (coherent enhancement), however to this point, experimental proof at ALICE was minimal. With the filter in position, the relationship between bunch charge and THz signal was seen to be quadratic, however with no filter in place, the relationship was non quadratic at the higher bunch charges, becoming quite linear. It is not fully understood why this was the case, however it may be due to changes in the beam position, and therefore source position of the THz.

4.3.15 Initial Beam Profile Study

To accurately perform the THz radiation beam profile experiments it was decided that a detector with a smaller active area than the power meter was required, while still keeping the ability to manoeuvre the detector. A pyroelectric detector was sourced and placed on a translational stage in order to perform a profile of the beam (the detector is discussed in the experimental chapter 2). This would provide vital information to understand the THz beam divergence. The detector body was placed 14 mm from the diamond window, with the detector element being 16.5 mm behind the detector body's front edge. This made the total distance from the diamond window to the pyroelectric detectors element 30.5 mm. The detector was set up with a x20 amplifier, a filter and its output channelled into an electronic scope. Figure 4.25 shows the detector on the translation stages in front of the diamond window. The image was taken from the diamond window and the M1M2 mirror vessel (cylinder) can be seen in the background.

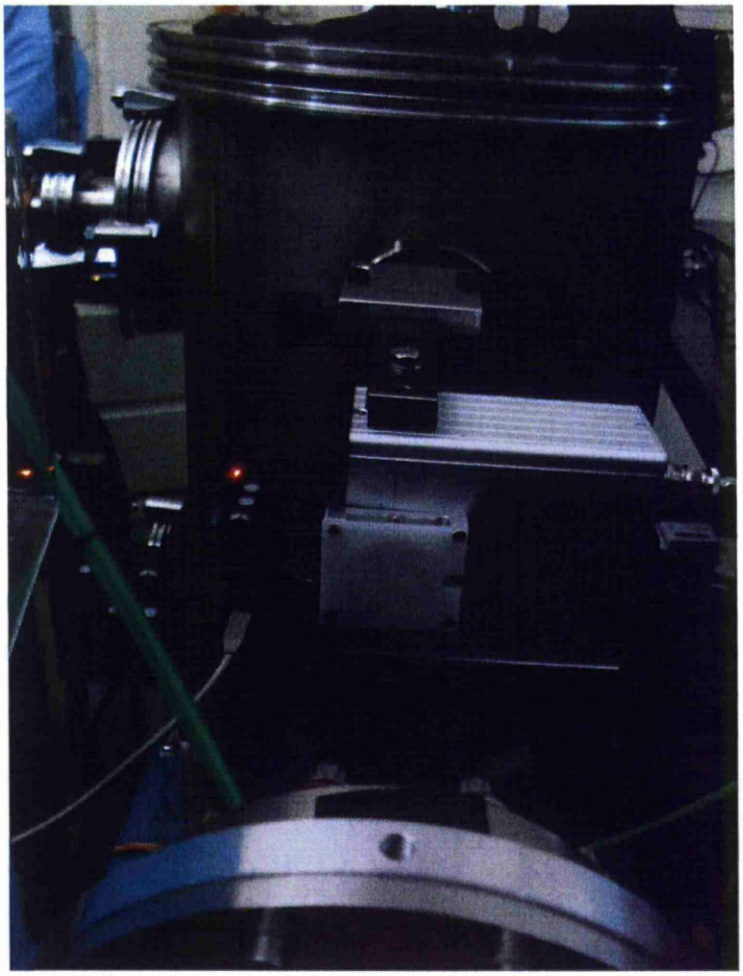

Figure 4.25. The pyroeletric detector fixed on the linear stage, photo taken from diamond window.

A schematic diagram of the setup is shown in figure 4.26. This shows the pyroelectic detector with its detector element lined up to the diamond window. Using the translation stage, which can be seen in figure 4.25, the pyroelectric detector could be scanned in the vertical and horizontal direction via computer controlled software. The distance from the diamond window can be changed to allow the measurements of the beam profiles, in order to monitor the beam divergence at different distances, however this can only be done manually.

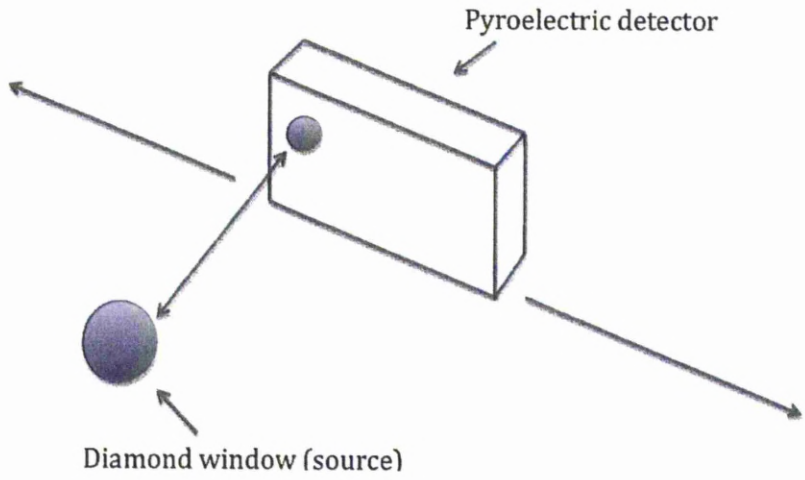

Figure 4.26. A schematic of the detector setup for the beam profile studies. The pyroelectric detector can move along the axis shown, as well as vertically (not shown) to measure the beam profile at a distance from the diamond window source.

The initial profile study was performed 30.5 mm from the diamond window. The pyroelectric detector was scanned in the horizontal direction with 108 mm representing the centre line of the diamond window to the detector. The results are shown in figure 4.27.

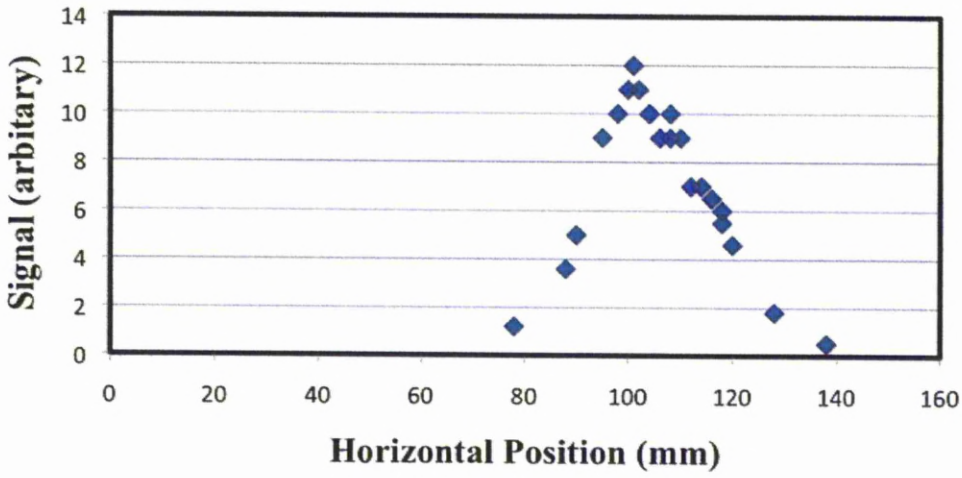

Figure 4.27. Horizontal beam profile results obtained with the pyroelectric detector 30.5 mm from the diamond window, the diamond window is perfectly lined up with the detector element at 108 mm.

Figure 4.27 shows a clear peak in the THz intensity located at 101 mm in the horizontal plane. If the THz was hitting mirror M0 as originally intended, it would be expected that the main peak would be at 108mm, where there is a very slight bump as this is on axis to the diamond window. However with the main peak being off

axis, this could explain the reason why very little/no THz was reaching the M1M2 vessel. The pyroelectric detector was then returned to 108 mm on the horizontal linear stage and a vertical scan was taken. The results are shown in figure 4.28.

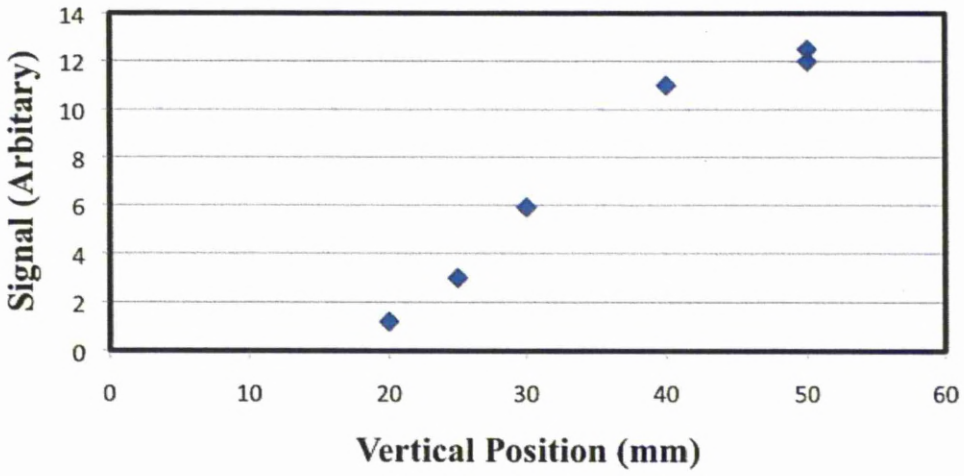

Figure 4.28. Vertical beam profile results obtained with the pyroelectric detector 30.5mm from the diamond window, the pyroelectric detector is central to the diamond window horizontally. 50 mm being level with the centre diamond window.

It was only possible to move the detector in the vertical plane between 20 and 50 mm with the 50 mm position corresponding to the height of the centre of the diamond window. This was due to the proximity of accelerator components. The experiment in the horizontal plane was repeated with a 11 cm^{-1} (0.3 THz) filter placed in the filter holder of the detector. The filters transmission is shown in figure 4.29. The filter allows light between 11-12 cm^{-1} and can be easily inserted into the fitted filter holder.

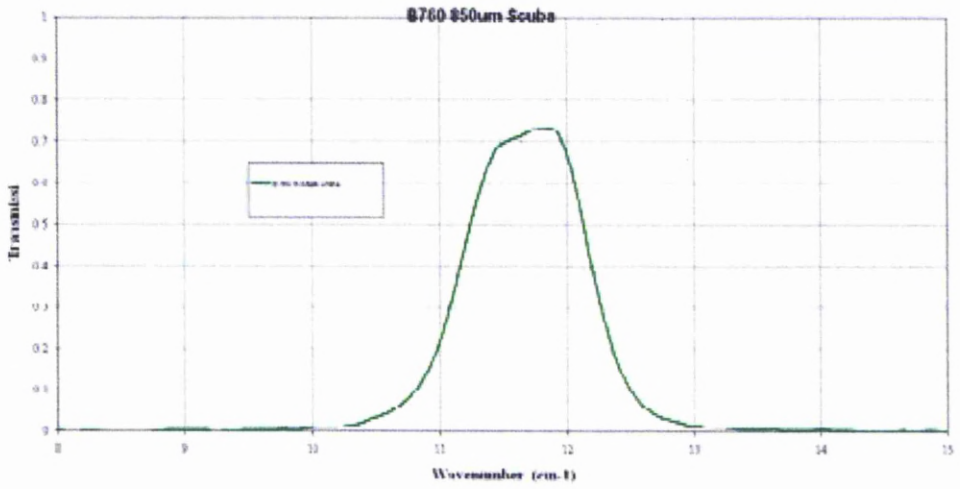

Figure 4.29. This graph shows the transmission of the 11 cm^{-1} filter used. The vertical axis is transmission with each division corresponding to 0.1 transmissions. The horizontal axis shows the wavenumber (cm^{-1}) with each division corresponding to 1 cm^{-1}.

The results of the horizontal beam profile with the 11 cm^{-1} filter in place are shown in figure 4.30. The peak was shown to be around 128 mm on this occasion compared to 100 mm on the unfiltered version. This is interesting as this demonstrates that coherent THz is being generated at wavelengths close to 11 cm^{-1}, however this is only a small contribution compared to the unfiltered version which shows a signal 10 times stronger (units are arbitrary). These early experiments indicated that the THz light was not directed on the expected axis from mirror M0. Further work was required to understand the reason why.

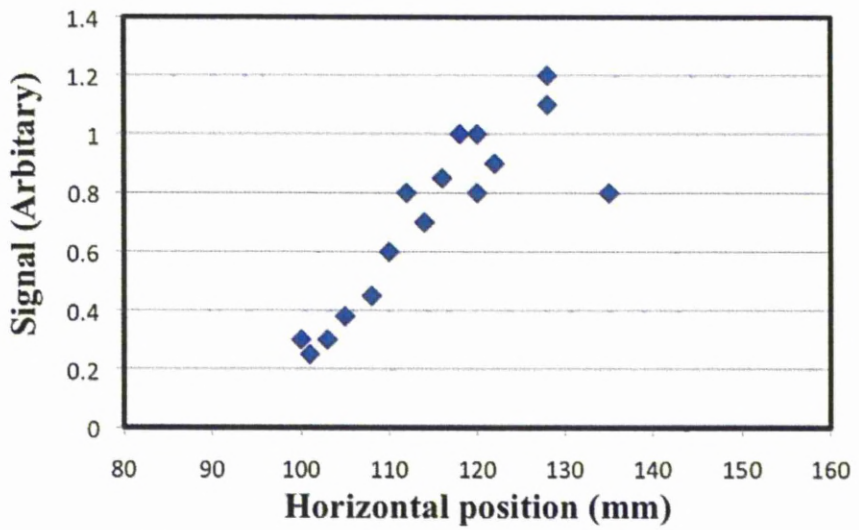

Figure 4.30. The filtered (11 cm^{-1}) horizontal beam profile obtained using the pyroelectric detector, vertically on centre with the diamond window 30.5 mm away.

The next experiment was to position the detector further back from the diamond window and record a beam profile. This allows the divergence to be reviewed further away from the source that can be directly compared with theoretical calculated divergences at similar distances. The first profile data was measured at 200 mm from the diamond window with no filter in place. Due to the new location of the linear stage, 200 mm from the diamond window, it allowed the detector to be scanned horizontally between 30-180 mm. The detector was centrally positioned to the diamond window at the 85 mm position. Vertically, the detector can be scanned from 0-50 mm, with the central position to the diamond window at 16 mm. The vertical scan was performed first and the results are shown in figure 4.31.

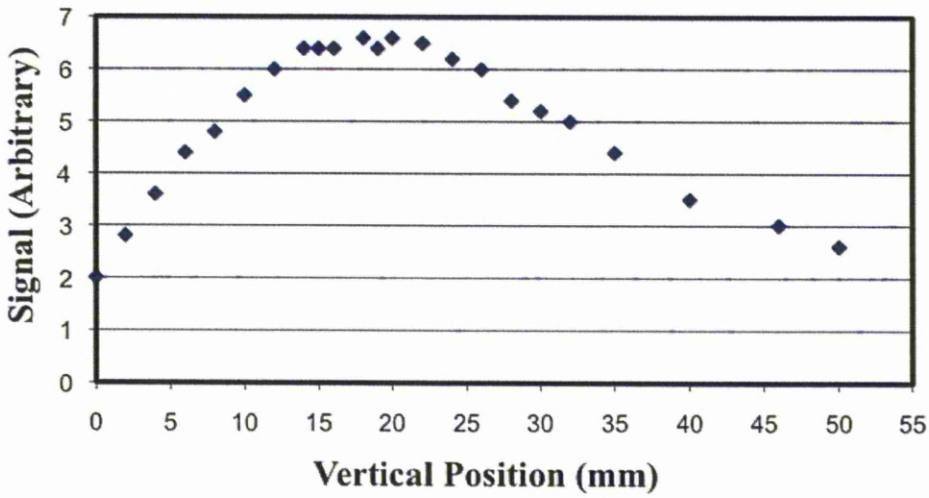

Figure 4.31. The vertical beam profile of THz radiation 200 mm from the diamond window, horizontally central to the diamond window (85 mm position). The horizontal scale shows the vertical position in mm, with the vertical centre of the diamond window is at 16 mm.

The vertical beam profile is quite broad with the peak roughly in the position 16-21 mm, which is in line with the diamond window. The horizontal scans were then performed, at three different vertical heights, 9 mm, 19 mm and 29 mm with 19 mm, chosen as the maximum from the vertical scan in figure 4.30. The horizontal scans, at each of the three vertical heights are shown in figure 4.32. (85 mm is central to the diamond window).

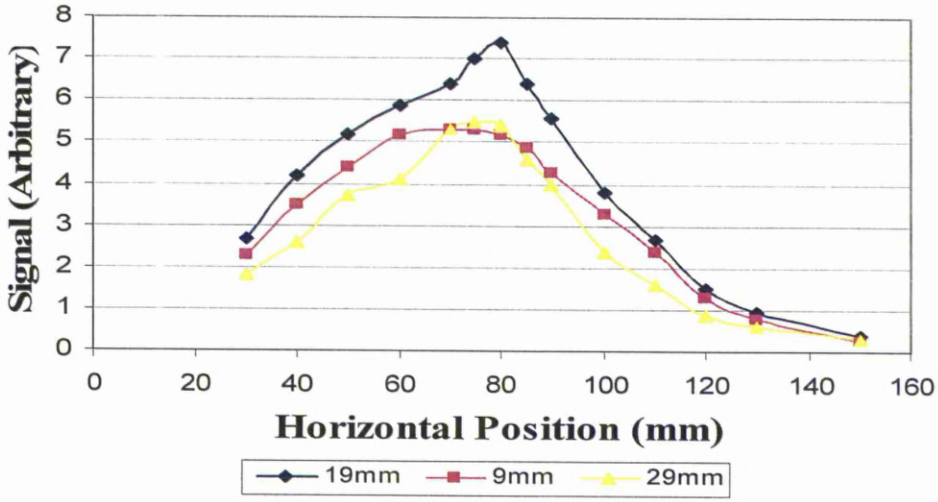

Figure 4.32. The horizontal beam profile at three different heights. 19 mm was chosen as the maximum from the vertical scans, the signal on the vertical axis is arbitrary.

Figure 4.32 shows that the peak on the horizontal scan is at 80 mm, which is only 5 mm off the centre of the diamond window. There is a definite peak observed in both the 19 mm and 29 mm horizontal scans, with the 9 mm scan showing a far broader divergence. The slight second peak observed in the earlier vertical scan closer to the diamond window is not present in any of these scans.

The following experiment was to take the same measurements with the 11 cm^{-1} filter, as previously discussed. Figures 4.32 and 4.33 show the vertical and horizontal scans respectively. All conditions have been kept the same; the only change is the addition of the filter.

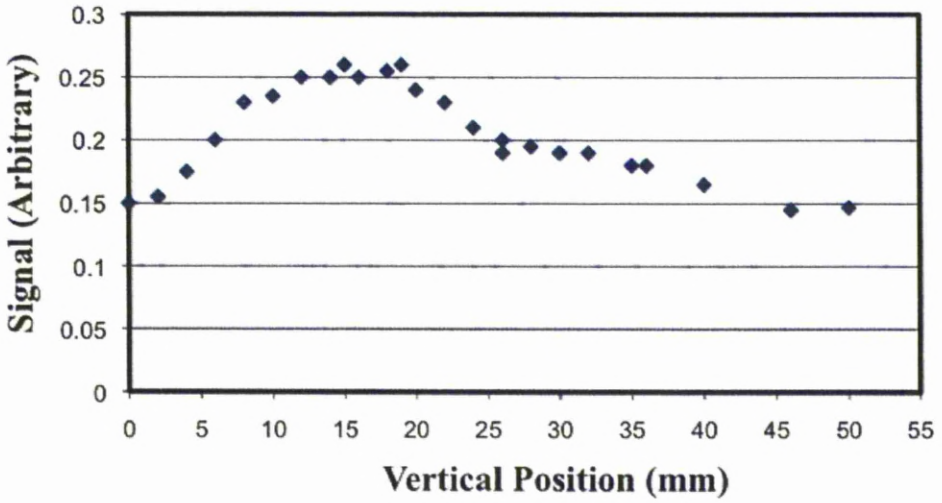

Figure 4.33. The above graph shows the vertical profile of the THz intensity filtered to 11 cm^{-1} at a central position horizontally to the centre of the diamond window.

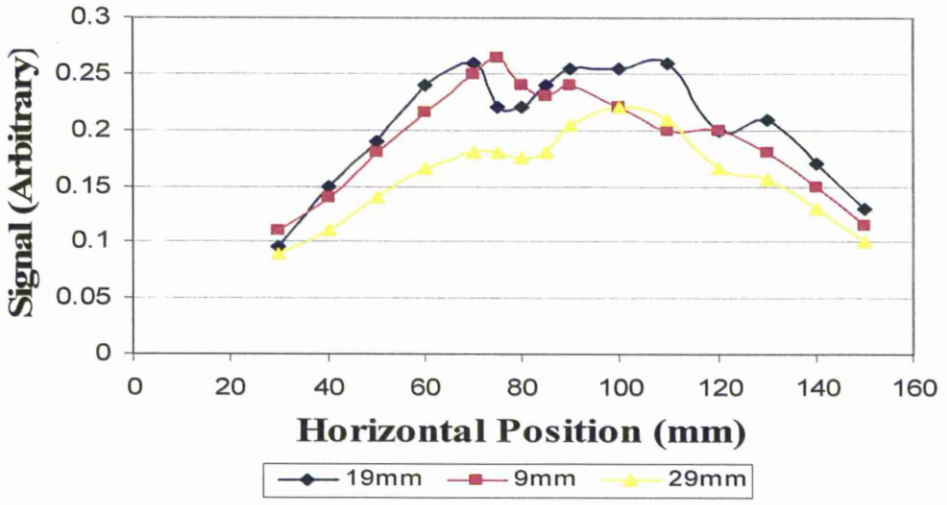

Figure 4.34. The horizontal beam profiles of THz intensity with a 11 cm^{-1} filter at 9 mm, 19 mm and 29 mm vertical positions. The signal on the vertical axis is in arbitrary units.

The vertical divergence is not seen to be any different with the 0.3 THz filter to the unfiltered beam profile, just a decrease in signal strength which is expected. However, horizontally the beam profile is very different, with three peak features, two main peaks at 70 mm and 90 mm with a trough at 75 mm, and a third peak at 110 mm. The main peak that was originally seen at around 80mm is no longer evident as a strong peak. The profile at 29 mm is similar to the profile at 19 mm, however the 9 mm horizontal profile has a very strong peak in a position that is not present in the others.

A second filter was used which accepts light between 25-31 cm^{-1} which is just below 1 THz (33 cm^{-1}). Figure 4.35 shows the filter transmission.

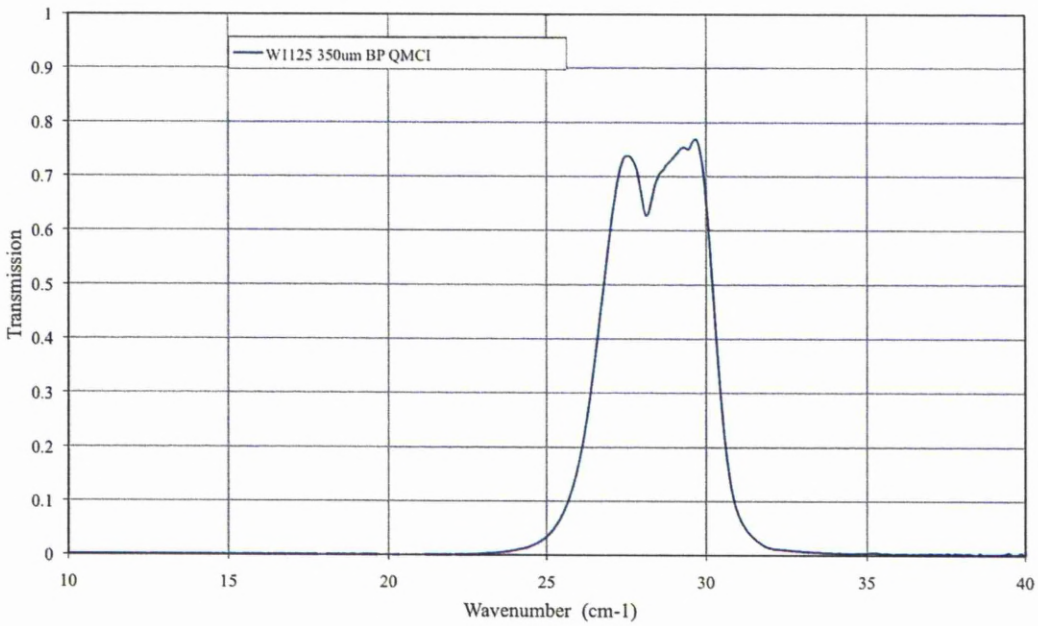

Figure 4.35. This is the transmission for the second filter, which allows light between 25-31 cm^{-1}.

Once the filter was positioned, the same scans were performed as with the 11 cm^{-1} filter and the unfiltered beam profiles. The results of the vertical scan are shown in figure 4.36.

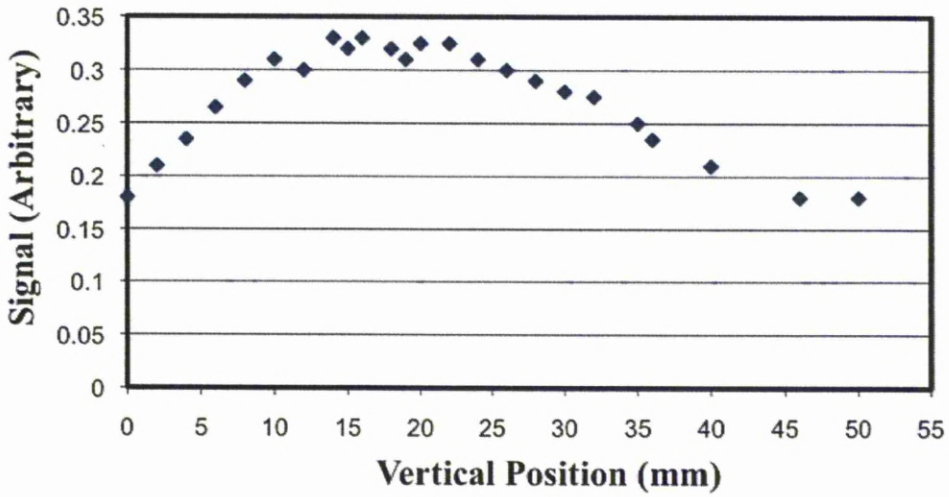

Figure 4.36. the vertical profile of the THz intensity filtered to 25-31 cm^{-1} at a central position horizontally to the centre of the diamond window.

There is little change in the vertical spectra, with the 25-31 cm^{-1} filtered when compared to the 11 cm^{-1} filtered and the unfiltered vertical beam profiles. Though the filtered intensities are far lower than the unfiltered scans, which is to be expected. The horizontal scans where then performed, again at the three vertical heights. These are shown in figure 4.37.

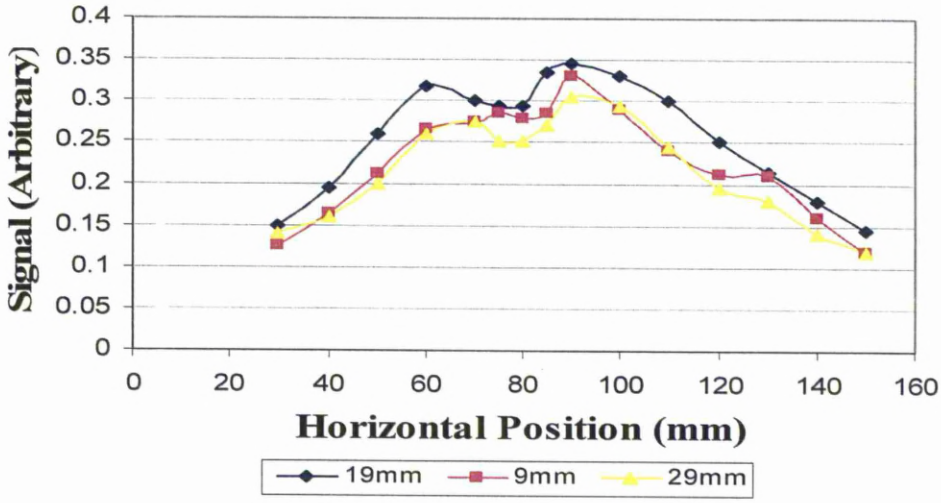

Figure 4.37. The horizontal beam profiles of THz intensity with a 25-31 cm^{-1} filter at 9 mm, 19 mm and 29 mm vertical positions. The signal on the vertical axis is in arbitrary units.

The overall width of the horizontal profile does not appear to change, although the peak seen in the 11 cm^{-1} filtered data at 110 mm is not seen in the 25-31 cm^{-1} filtered data, however the other peaks at 85-90 mm and 60-70 mm are still present. Both the filtered profiles are far broader in full width half maximum (FWHM), though the signals are very small. The differences between the filtered data and the unfiltered data are very interesting, and suggest that the propagation of the THz radiation at these wavelengths is not as theoretically expected. Further work is needed in this area, with more sensitive detectors.

The next step of the experiments was to perform the beam profile measurements at a position 300 mm from the diamond window. Due to the diminished signals seen at 200 mm from the diamond window when the filters were used it was decided that it would not be of use to perform the experiments at 300 mm due to signal to noise issues. The position of the linear stage, and therefore detector position was officially surveyed to find the exact position relative to the centre of the diamond window using engineering lasers prior to any movement, and a new beam profile taken at 200 mm from the diamond window. The detector was placed

300 mm away from the diamond window, measurements retaken with the engineering lasers and a profile at the further distance measured. Figure 4.38 shows the vertical beam profile, horizontally central to the centre of diamond window, comparing the measurement at 200 mm and 300 mm. 0 mm on the horizontal axis represents the central position of the diamond window.

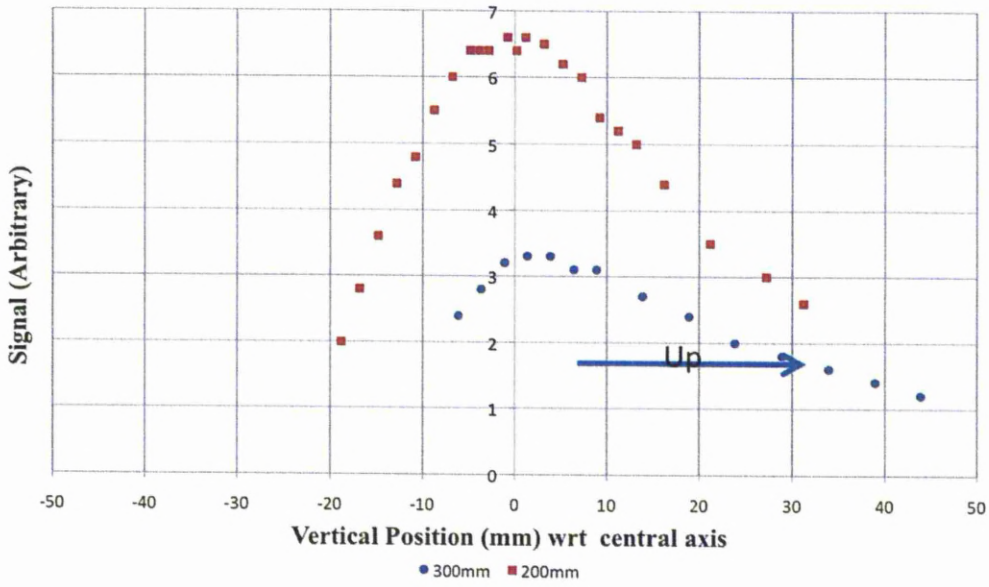

Figure 4.38. The vertical beam profiles of THz intensity at 200 mm from the diamond window in blue diamonds, and 300 mm from the diamond window in red squares.

Figure 4.39 shows the comparison of the THz intensity beam profiles horizontally.

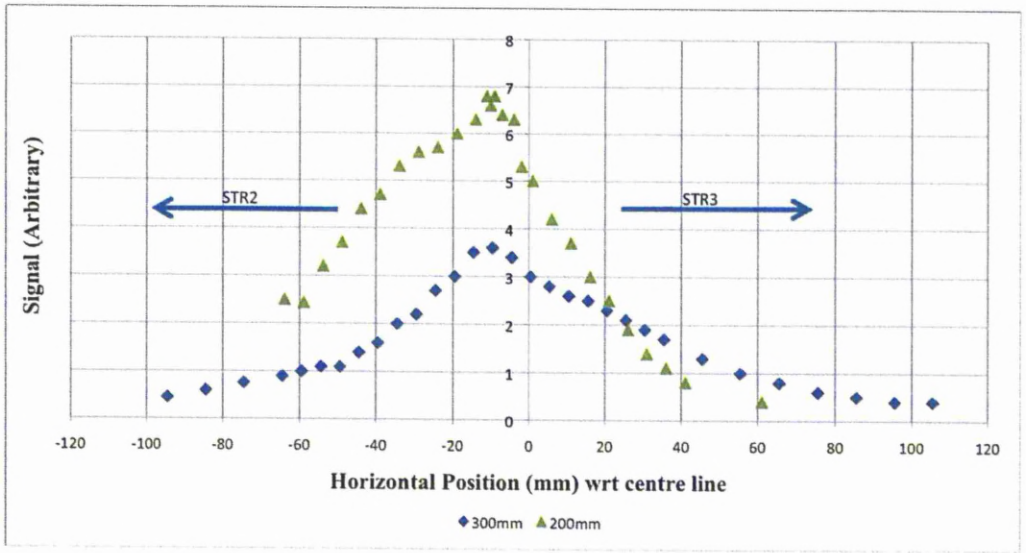

Figure 4.39 The horizontal beam profiles of THz intensity at 200 mm from the diamond window in blue circles, and 300 mm from the diamond window in red squares.

The vertical scan is similar at 300 mm to that seen at 200 mm, although the maximum signal is slightly above the axis at 300 mm. Horizontally they both are quite similar, with exception of the signal power, so it is difficult to deduce the amount of divergence between the two, the main intensity of the THz beam is diverged over 60 mm horizontally when only 200 mm from the diamond window, and diverges further at a distance of 300 mm. There is a slight shoulder peak seen in the measurements at 200 mm from the diamond window. Once the signal is under 1 V it is difficult to make any firm conclusions. Due to the position of peak signal in the experimental data being close to the theoretically expected and designed position it was hoped that through beam steering in the chicane, or by a slight reposition of the M1M2 mirror vessel the small difference could be accommodated allowing better transport of the THz radiation.

4.3.16 Comparison of Experimental Results with Model

The experimental results were compared with the basic model used during the design of the THz transport beam line by Marion Bowler. Mark Roper of Daresbury lab, adapted the synchrotron radiation wave (SRW) code previously used to look at the beam profile information at 1 meV (8 cm^{-1}) and 0.6 meV (4 cm^{-1}), this data was them compared with experimental results. The SRW code has significant limitations at the chosen wavelengths, which may not allow for spurious features arising from possible diffraction patterns. The code only allows for a single electron output to be modeled for coherent sources. This means that any potential effects of the electron beam emittance are not covered in the simulations. All the output intensities are in arbitrary units due to the code being unable to calculate coherently enhanced emission. A further limitation in the SRW code is the inability to add a plane mirror to the transport system. Therefore the extraction mirror is simply modeled as an aperture, with the diamond window a second circular aperture. Figure 4.40 shows the field intensity distributions using a rainbow colour scheme, red is low signal/none, blue is strongest signal. The top left image shows the 1 meV intensity at 3 cm after the diamond window, the central left image showing 30 cm away from the diamond window and the bottom left image showing 100 cm away from the diamond window. On the right hand side is the same distances but for the 0.6 meV photon energy. Initially the circular diffraction ripples can be seen, however as you move away from

the diamond window the early structure of the beam disappears and a single peak begins to show through at 100 cm after the diamond window [7].

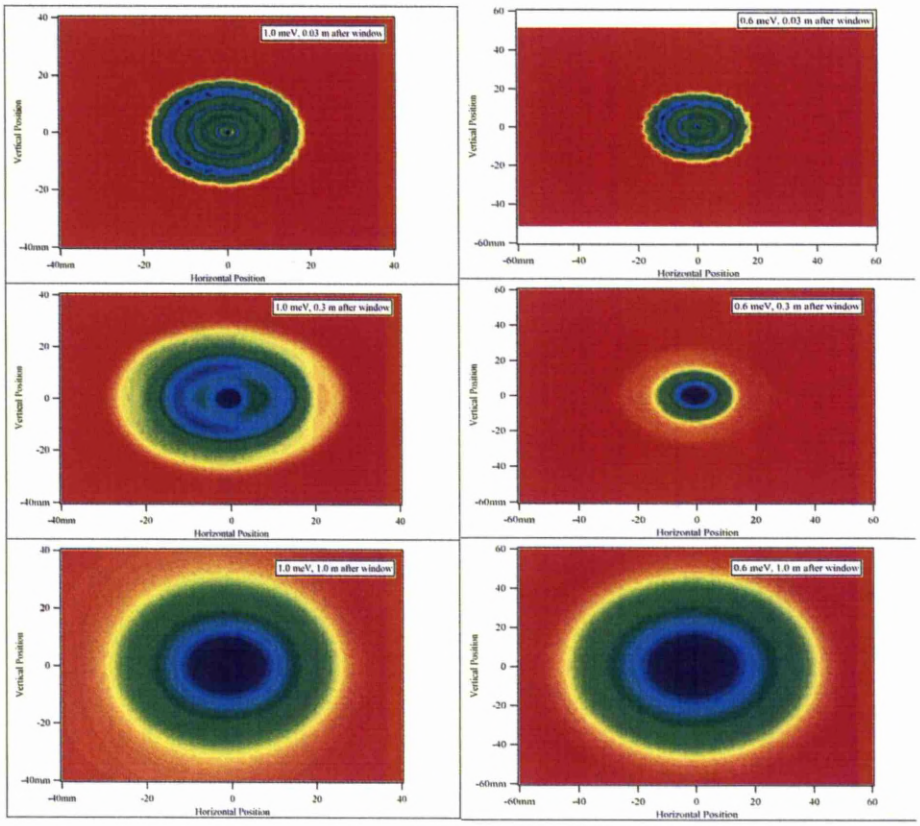

Figure 4.40. Above are the beam profile intensity images based on the SRW code at 1.0 meV on the left, and 0.6 meV on the right. The top images are at 30 mm from the diamond window, middle images are 300 mm from the diamond window and the bottom images are 1000 mm from the diamond window. The scale is a rainbow colour with blue showing areas of strong intensity and red showing low/zero intensity areas [7].

Figure 4.41 shows the horizontal beam profile of both the 1 meV radiation and the 0.6 meV radiation. They both show, like in figure 4.39, that the initial beam structure disappears as the distance from the diamond window increases as it blends into one signal peak [7].

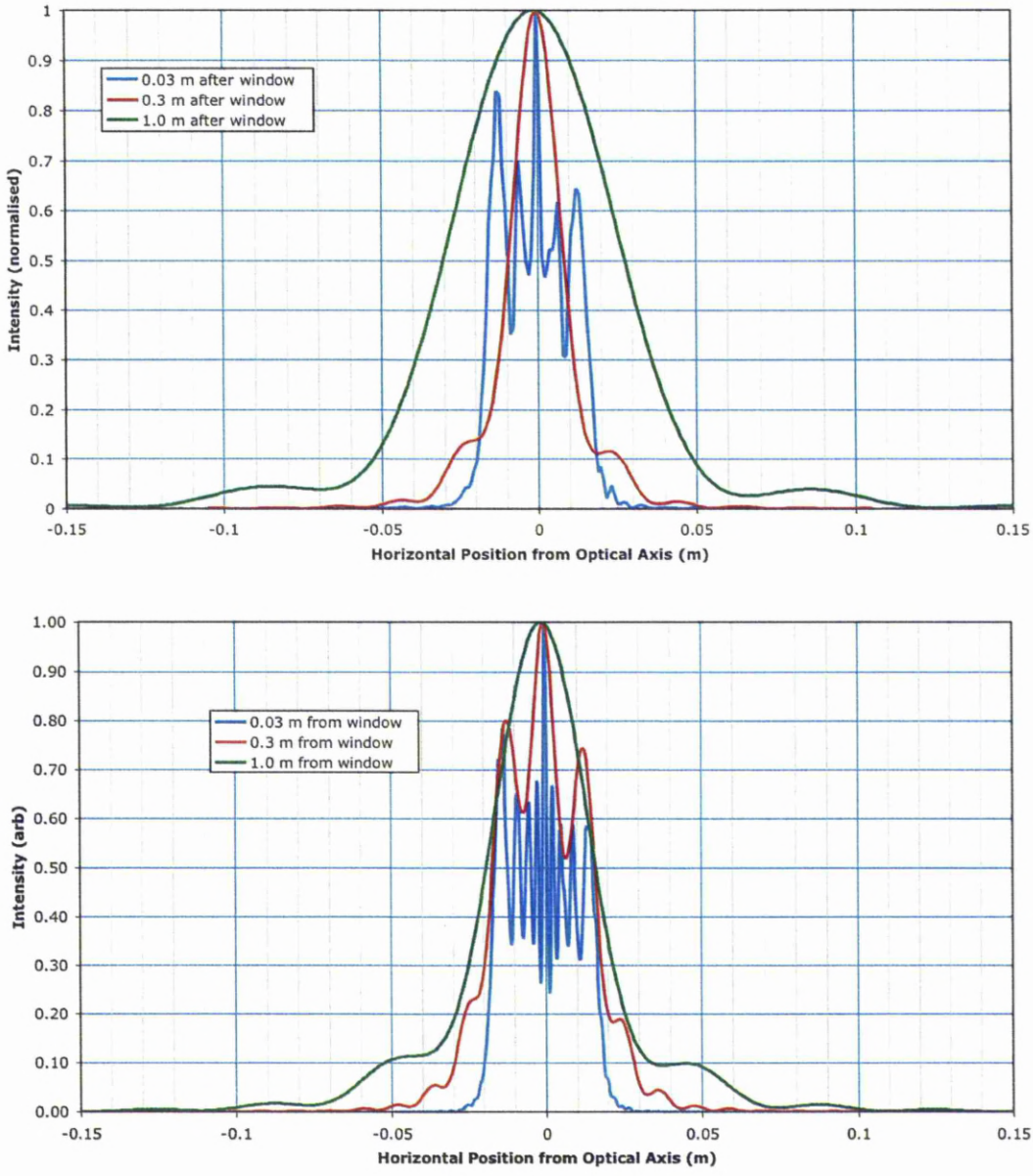

Figure 4.41. Simulated horizontal beam profile of 1 meV Radiation in the top graph, and 0.6 meV in the bottom graph. The intensity is normalised [7].

Figure 4.42 shows the comparison between experimental data taken and theoretical data calculated shown in the previous two figures. The theoretical data is taken for 0.6 meV, 1 m away from the diamond window and the experimental data is from two experiments where the measurements are taken unfiltered and 1 m away

from the diamond window. The difference between the two measured beam profiles in figure 4.42 is the accelerator conditions, resulting in different bunch compression in the chicane and a change in the source position.

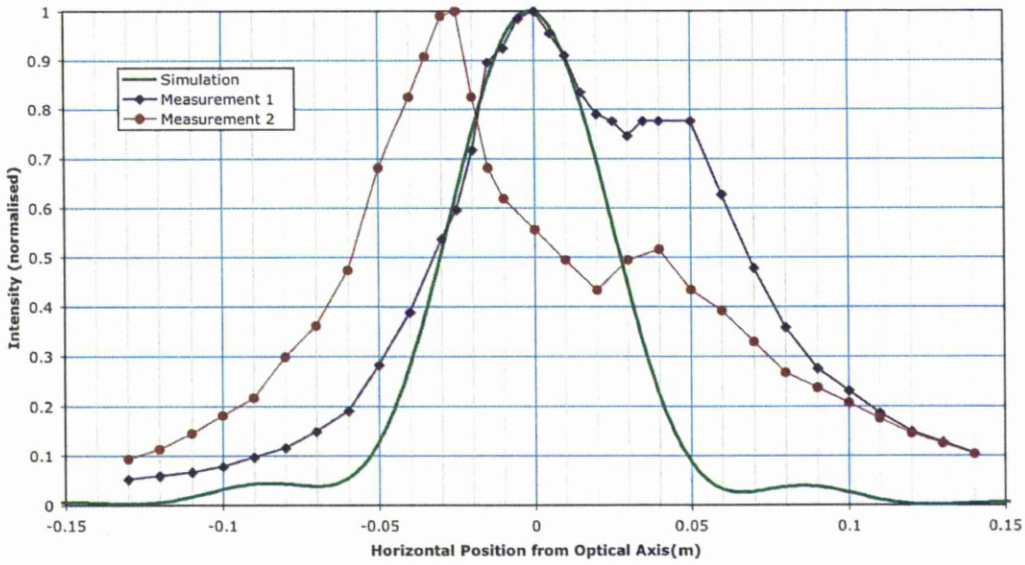

Figure 4.42. Comparison of beam profiles. The simulated data is taken at 0.6 meV 1 m away from the diamond window and unfiltered measured profiles at 1 m from the diamond window [7].

The biggest difference between the measured beam profiles and those from the simulation is the appearance of the second peak in the measured beam profiles. It is suggested that the two peaks arise from two sources of THz. The first being from the fourth dipole, the desired source point of the THz from the chicane, and the second peak due to THz radiation from any or all of the dipoles. The latter could be scattered around the dipole vessel and after multiple reflection transmitted through the diamond window.

In previous work by Mark Roper [8] calculations demonstrated that a radial movement of the effective source point of 10 mm would give an angular shift of the beam by about 25 mrad. After a meeting with a number of the accelerator scientists, Yuri Saveliev, ALICE Senior Accelerator Physicist, suggested that the change in machine settings could present a movement of the source point by up to 20 mm, which could explain the movement seen in the two experimental measurements in figure 4.42, and would suggest that this peak resulted from THz from the effective source point in dipole 4. The difference between the two peaks is 30 mm which is

slightly more than would be expected in the meeting, however later discussions suggested it was possible.

This led to the belief that the second peak, which is in the same position in both measurement profiles despite the steering effect, was due to scattered radiation. Work performed by Roper [9] discusses the effect of scattered light out of the diamond window. He suggests that light scattered within the dipole vessel that exits the diamond window having reflected off mirror M0 would most likely direct out on the downstream side of the optical axis, towards STR3 (the third straight in the ALICE beam line, shown in figure 4.1). However if the THz radiation that is scattered in the dipole vessel exits the diamond window without deflecting off the diamond window it will exit on the source side of the axis, therefore back towards the chicane. Consequently it is considered that the fixed peak is due to scattered radiation transmitting out of the diamond window, having not reflected off mirror M0. This could be due to bunch compression in other parts of the chicane, which will be discussed in the bunch compression section.

4.3.17 Study of Mirror M0

In an effort to understand the difficulty in transporting the THz through the mirror M1M2 vessel a parallel study, performed during the beam study work in the previous section, was performed at the University of Liverpool on a replica mirror M0, as mentioned earlier. The mirror M0 can be seen through the diamond window to the left of figure 4.43.

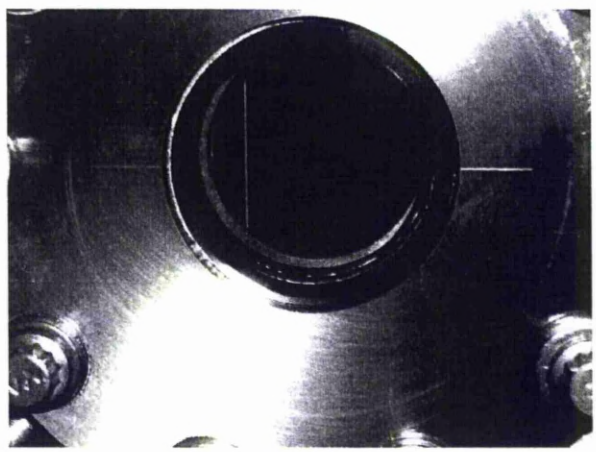

Figure 4.43. Mirror M0 behind the diamond window. The picture shows the diamond window with the edge of mirror M0 on the left hand side.

An exact replica of mirror M0 is shown in figure 4.44. The mirror is placed in the holder by sliding it into position and it is possible that the mirror had not been correctly located and had slipped as shown in the image on the right of figure 4.44.

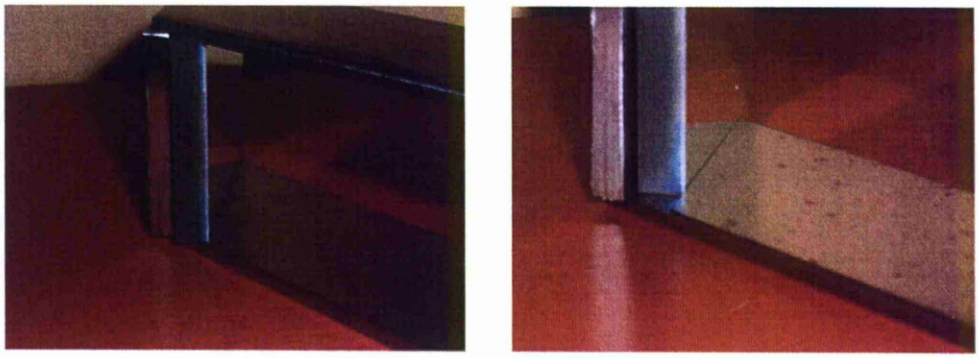

Figure 4.44. Two images of the Mirror M0 in its holder, on the left shows the mirror in the correct position, on the right shows the mirror has been slightly pushed away from the camera.

By shining a light into the diamond window it was established that the mirror was correctly positioned in the holder. This is shown in figure 4.45.

Figure 4.45. The view through the diamond window, using an intense light source to check the mirror position. It can be seen that the mirror is in the correct position.

This was very positive news as work on the THz beam line to this point had indicated that the problem was from either the source point of the THz or the mirror M0. Had the mirror been the issue, either by being set at the wrong angle, tested at University of Liverpool, or slightly out of position, it would be very difficult to fix, and very timely, due to the requirement to let the accelerator up to atmospheric pressure to gain access to the mirror.

A possible problem with the source point is the electron beam not being compressed correctly. The observation of emission confirms that short bunches are being generated. However it is important that the short bunches are produced in the area of the chicane that is close to the source point.

4.3.18 Beam Compression

The beam compression is an important part of the generation of THz radiation. The design specifications and position of the mirror M0 were developed from the theoretical model of the electron trajectory through the chicane developing an ideal curve. The effective source point for the model was taken from this data and used in order to model the THz beam line calculated from this point. Therefore if the THz is not generated at or close to this ideal source point, this would explain the beam profiles seen in the section previously. This section will discuss the beam compression that could take place during experimental running and have led to the two peaks seen in the beam profile section, using a theoretical model based on experimental accelerator parameters. The Elegant code was developed by Michael Borland [10] from the Advanced Photon source at Argonne National Lab and was applied by Peter Williams, a beam scientist at Daresbury. The code includes the effects on the beam of the generation of coherent synchrotron radiation. In ALICE the coherent synchrotron radiation is in the THz region, so when the graphs show energy loss in the beam due to radiation, it can be assumed that most of this beam loss is the result of THz generation.

As previously mentioned this simulation uses the accelerator parameters that were used in the beam profile experiments, which allows an insight into the potential problems with the compression chicane. However the bunch used in the model, is not based on experimental bunches, but on a theoretical one.

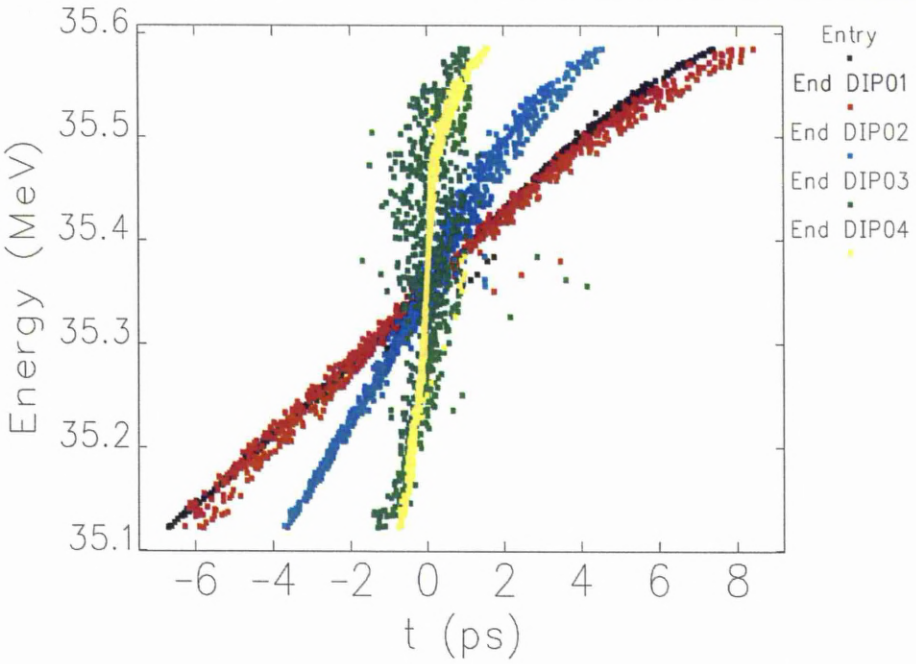

Figure 4.46. Longitudinal phase space (energy vs time) of bunch at five points in the chicane.

Figure 4.46 shows a plot of the longitudinal phase space, with energy vs. time at 5 different points in the chicane. This shows the beam compression expected under the ALICE operating conditions. There is little or no compression in the first dipole, the spatial distribution is very similar to that of the bunch at entry. The bunch is then shortened progressively in dipoles 2 and 3 with a small change in dipole 4. The latter, between dipoles 3 and 4, is a geometrical change due to tightening of the bunch. These results support earlier views that THz could be generated at dipole 3 and would bounce around the beam pipe before exiting the diamond window, along with the THz generated at the source point.

This is comparable with measurements accelerator physicists had taken on the accelerator. They had looked at the proportion of change in the bunch compression, through the chicane and their figures suggested that the highest compression was taking place in bending magnet 3, with bending magnet 4 slightly decompressing the bunch [11]. This would agree to an extent with the Elegant theory results and the suggestion that the THz is being generated in the wrong position of the chicane. The experimental THz profile data generated would also agree with this.

Experimentally it was found that the length of the bunch following transport through the linac was four times longer than expected though the compression in the chicane was as expected. When the bunch length is long, there is the likelihood that

the bunch can, under compression, curve. This curvature of the bunch can result in a lack of compression and therefore a loss in power of THz signal. This curvature can be overcome by using the sextupole magnets in the arc, which re-straighten the bunch that therefore allows it to be successfully compressed in the chicane. Experiments were performed to test the affect of the sextupoles on THz signal, though the results vary.

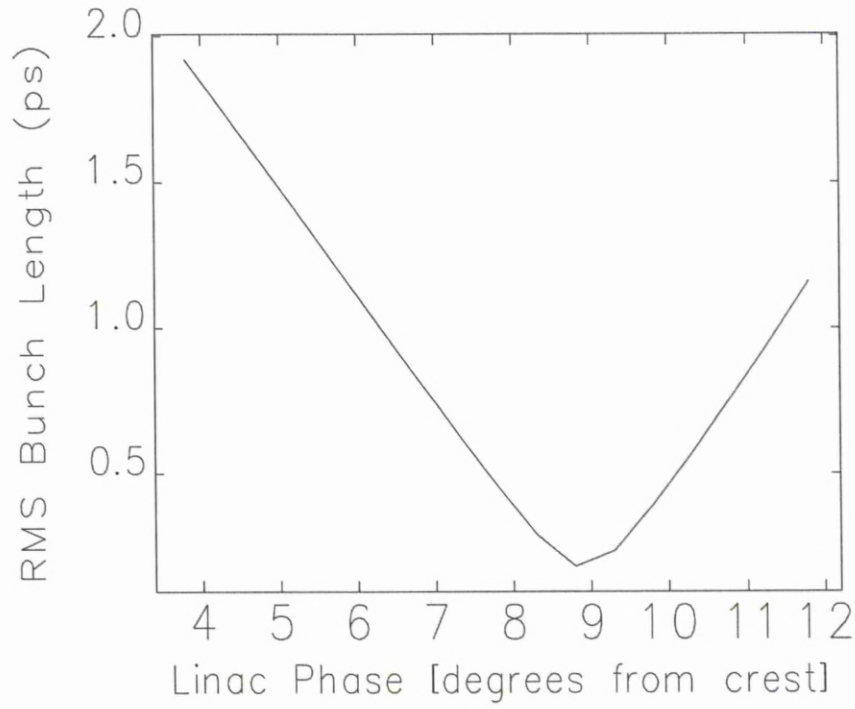

Figure 4.47. Theoretical results from Elegant simulations of the affect of linac phase on RMS bunch length (ps) at the end of dipole 4.

Figure 4.47 shows the affect of linac phase on the RMS bunch length at the exit of the chicane dipole 4, calculated using the Elegant model. This shows that the maximum compression of the bunch occurs when the linac is set to 9 degrees off crest, however the compression is greater than previously considered. The crest of the linac and the ability to move off crest was discussed earlier and this effects the "energy chirp" of the bunch. This theory links closely to the experimental results, where it has been shown that the maximum THz signal comes when the linac is set to 9 degrees off crest. This will be revisited later, when experimental results are shown in the filter section.

Figure 4.48 shows the affect of the linac phase on the loss of energy in the bunch to THz radiation in the different sections of the chicane. The red line

(indicating 9.8 degrees) demonstrates that the linac setting of 9.8 degrees off crest is the optimum setting for THz generation in the final dipole and has been proven to be similar experimentally. It is worth noting that with a linac phase of 7.8 and 11.8 off crest (blue and black respectively) they both result in the same total amount of THz generation, however with the linac phase of 11.8 off crest there is a greater loss in dipole 3, consequently less produced in the last dipole, which is most suitable for the THz beam line. Therefore it is desirable to have the linac phase that results in the highest amount of THz production in the final dipole, rather than the greatest total, however theoretically a linac phase at 9.8 degrees off crest gives both, the largest amount of THz at the 4th dipole, and the highest total of THz.

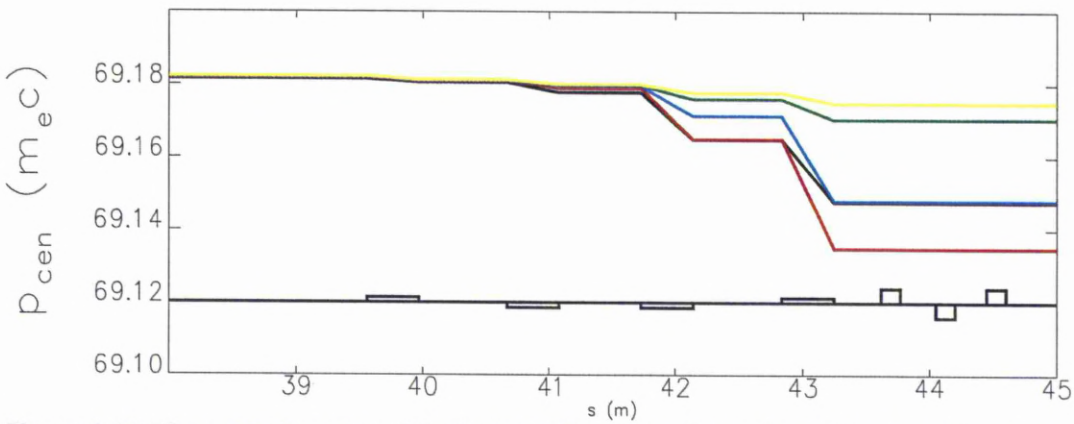

Figure 4.48. The central energy of the beam with varying linac phase. The drop in energy (y axis) is due to the energy lost via THz in the dipoles. The blue has a linac phase of 7.8, the black 11.8, red 9.8, the green 5.8 and the yellow is 3.8 (all off crest).

Measurements taken at the diamond window using the power meter have demonstrated that while the generation of THz is quite easy, transporting the THz light correctly to the M1M2 mirror vessel is very difficult. It is likely that a lot of the THz light that is observed is not coming directly from the source point at the fourth dipole, but from other places within the chicane and bouncing inside the electron transport system before leaving the diamond window in a divergent manner. The beam profiles that show the broad THz range with the small peak in the centre seem to arise from a proportion of the THz signal generated at dipole 3, with the peak signal coming from THz radiation generated at dipole 4.

There is a positive aspect to these observations in that the poor transport and wide beam profiles are caused by the accelerator beam conditions rather than problems with the position of mirror M0. This is fortunate since it would be more

difficult and more expensive to replace and/or move the mirror M0 or the diamond window than to vary the beam conditions. Once the electro optics system is installed it will be possible to measure bunch lengths, which will allow better understanding of the transportation and efficiency of the beam line. This may also provide information on other sources of THz other than dipole 4.

4.3.19 THz Signal with 850 Micron Filter

It was decided that the cell experiments that were originally planned for the tissue culture facility would take place in the accelerator hall. This is discussed in more detail in chapter 5, however during the commissioning of the beam transport system to the incubator in the accelerator hall a number of preparation experiments were performed. A light pipe was installed to transport the radiation to the incubator, and it was noticed that this massively increase the THz signal, as it was internally polished metal. This allowed the opportunity to perform a number of filter experiments to gain more information on the affect of accelerator conditions on the THz signal, as the powers were stronger than previously seen. This resulted in the ability to look at the unamplified signal without a filter, and an amplified signal once the filter was in place, and make more accurate comparisons. The filter used was an 850 micron (0.3 THz) filter, figure 4.48 shows the transmission of the filter provided by the manufacturer.

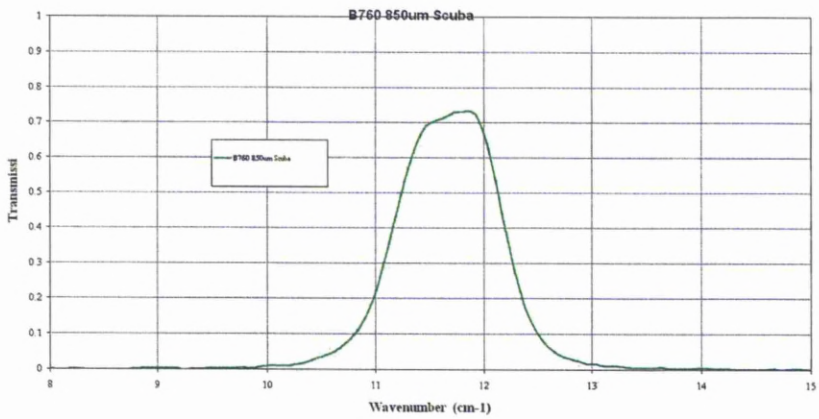

Figure 4.49. This is the transmission of the 850 micron filter, the y axis shows transmission with wavenumber on the x axis.

The new light pipe, between the diamond window and the incubator, has a small gap, halfway down, which can be closed to allow transportation of the THz radiation to the incubator, or opened to allow a filter to be fitted as can be seen in

figure 4.50. It is possible to position the filter using the linear stage, with a webcam positioned to monitor its movement. This is an improvement on past experiments as there is no requirement for the accelerator to be ramped down to allow limited access to change filter. The pyroelectric detector remains in the incubator, as is shown in the cell exposure section.

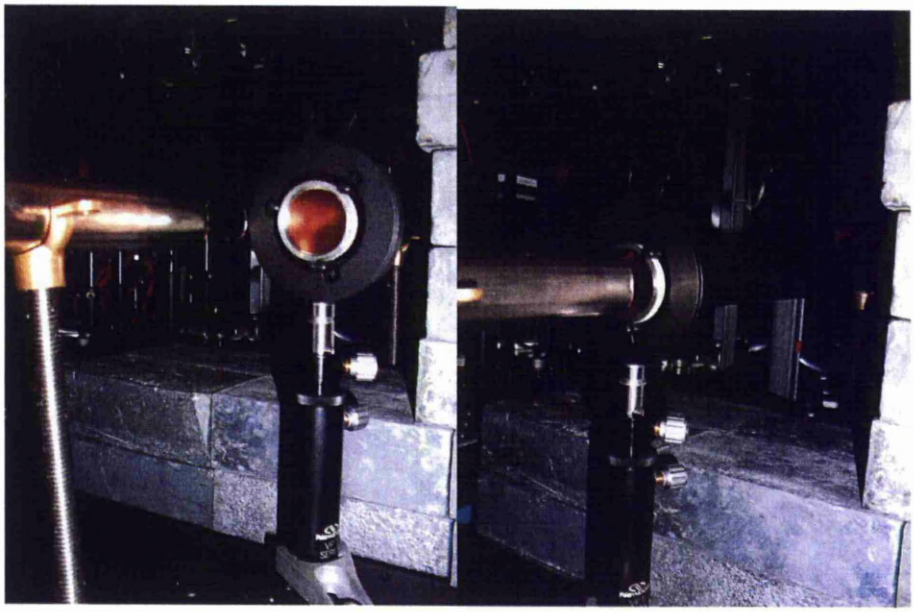

Figure 4.50. The filter shown out of position of the light pipe on the left, and in position on the right.

Theoretically, with a full signal, with the beam conditions used in the experiment, 27.5 MeV, 35.5 pC and 100 μsecs you would expect a signal of 149.4 μJ for a 0.6 ps RMS bunch length (0.8 ps RMS – 103.8 μJ) with the filtered signal being 6.6 μJ at 0.6 ps (0.8 ps RMS – 2.4 μJ). Table 4.2 for varied bunch lengths is shown below.

Table 4.2. Theoretical values for full THz signal and filtrered THz signal with the accelerator set to 27.5 MeV, 35.5 pC and 100 μsecs train length with a variation of RMS bunch length.

Bunch length	Full THz signal	filtered THz signal	Ratio
ps	μJ	μJ	
0.3	359.1	17.2	20.8
0.4	249.7	13.4	18.6
0.5	188.3	9.7	19.4
0.6	149.4	6.6	22.8
0.7	122.9	4.1	29.7
0.8	103.8	2.4	42.8
0.9	89.4	1.3	67.5
1	78.2	0.7	115.7
1.1	69.2	0.3	215.4
1.2	62.0	0.1	434.0
1.3	55.9	0.1	944.3
1.4	50.8	0.0	2214.2

Figure 4.51 shows the graph of this theoretical data with the THz signal for the unfiltered on the left *y* axis, and the THz signal for the filtered on the right *y* axis.

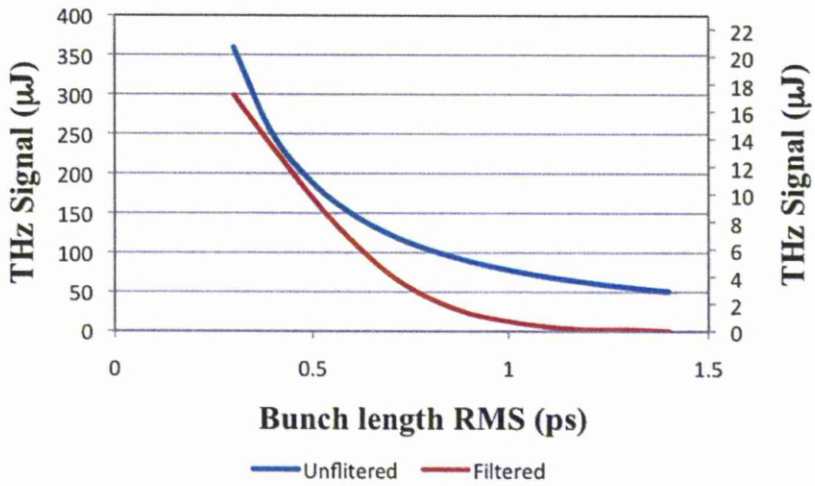

Figure 4.51. The theoretical affect of bunch length on the THz signal, filtered and unfiltered. Note the change in axis scales. The unfiltered values are plotted on the left *y* axis, with the filtered values plotted on the right *y* axis.

The expected spectrum from theory is shown in figure 4.52.

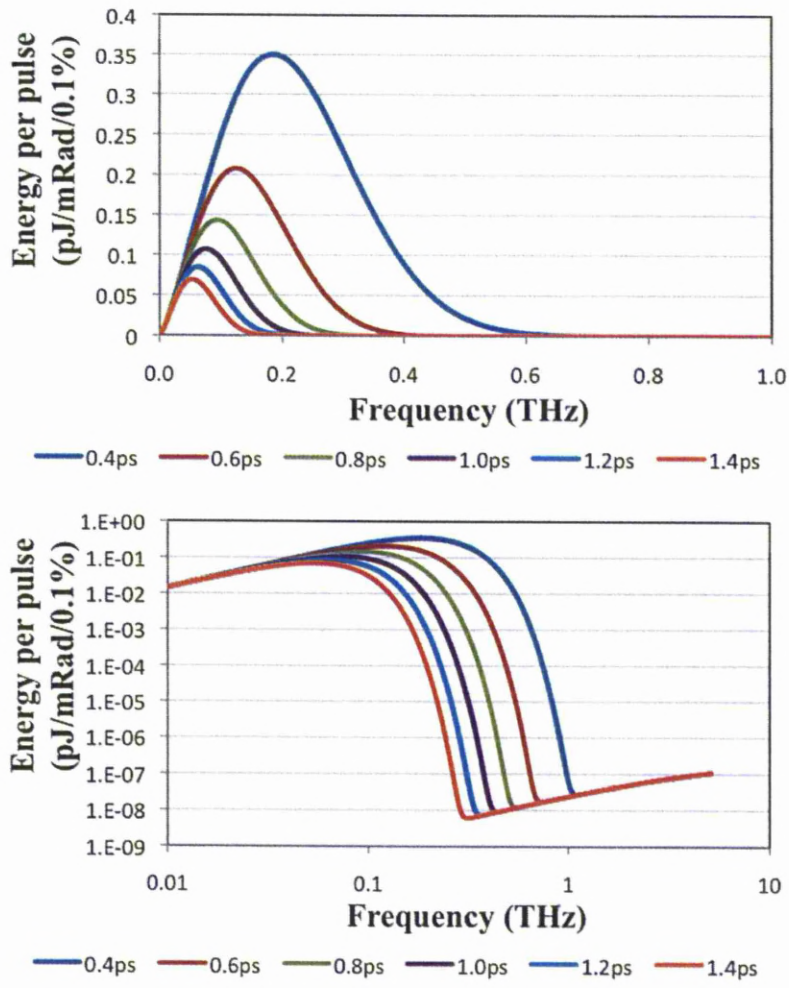

Figure 4.52. The expected theoretical THz spectra, with varying bunch length and 27.5 MeV, 35.5 pC and 100 μsec, the above is fit on a normal scale, the bottom with a log scale.

Experimentally the filter produced a reduction in THz signal of a factor of 150 during experiments performed with an accelerator set up that is suitable for FEL running. A 9.2 V signal was observed after amplification with no filter in place at a train length of 50 μsecs and once the filter was inserted the signal dropped to 0.13 V after amplification at 100 μsecs. However, when the machine was set up specifically for THz generation, the measured amplified signal at 15 μsecs was 5 V, with an expected extrapolated signal of 33.33 V if the train length was upped to 100 μsecs (this was not possible as the detected would saturated at roughly 9 V). The measured amplified signal once the filter was positioned was 1.72 V with a train length of 100 μsecs. This results in a ratio between the unfiltered and filtered of 19.4, indicating a RMS bunch length of 0.6 ps. Early work with the electro optics suggest

that the experimental train length is between 0.6-0.8 ps. This shows a good correlation between the theory and experimental data. This experiment should be repeated with a calibrated Pyroelectric detector so to allow for absolute values to be measured and compared.

4.3.20 Further Filter Experiments

A number of filters were sourced and a filter holding plate was designed that could be placed on the translatable stage, which has been used in a number of previous experiments. This meant that the filter could be driven into place remotely in order to avoid the need to enter the accelerator hall on limited axis. A custom made filter holding plate was manufactured, with a number of holes to allow filters to be inserted. The holes were cut in order to create a tight seal around the filter, something that had caused concern during the previous study, as it was possible that the THz radiation may be leaking around the edge of the filter.

The filter holding plate was placed on the translatable stage, with the detector in a fixed position behind the plate, on line with the diamond window. The plate was moved, by the linear stage to confirm the position of the specific filter holes, ensuring they were centrally located, and online with the diamond window. The plate was positioned in five different positions; position one had no hole just the plate blocking the detector, the second has the 3 THz filter, the third having the 1 THz filter with the fourth position just a hole to allow full radiation and allow for the aperture. A fifth position was noted where the plate was driven out of the way of the detector completely, to allow complete exposure with no aperture.

The detector used for this study was 2 mm pyroelectric detector fitted with a 20 THz black polythene filter. An alteration was made by Paul Harrison to improve the gain and amplification of the signal.

The first experiment performed showed there was no signal when the solid aluminium plate was in place, as expected, and 9.2 V (close to saturation of the detector) when the plate was completely removed. When the 3 THz filter was inserted the signal dropped to 8.6 V, with a signal of 8.7 V when the 1 THz filter was inserted.

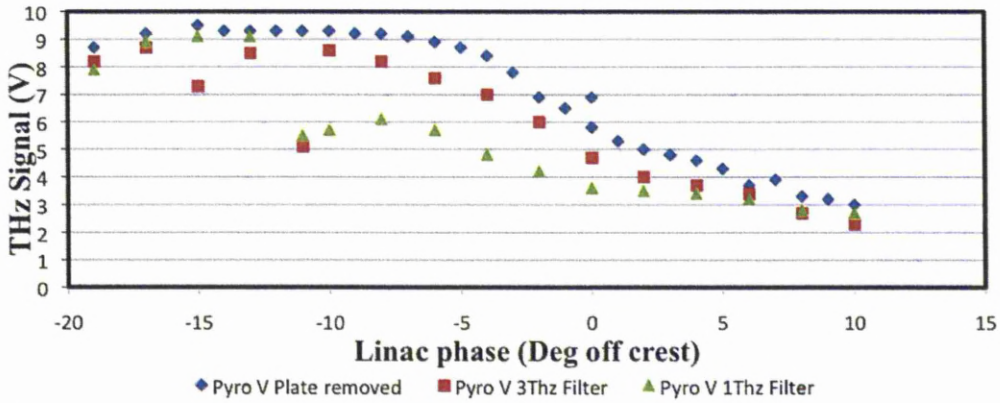

Figure 4.53. Effect of linac phase on filtered THz signal.

The subsequent experiment was to measure the THz signals using the filters as a function of linac phase, with the results shown in figure 4.53. As previously discussed the linac phase changes the "energy chirp" on the electron bunch (not only in power but in specific frequency due to coherent enhancement), so effects the compression that takes place in the chicane. As expected the THz signal has shown to have a massive effect from linac phase, previously discussed in the bunch compression section. The peak in THz signal is at -10 to -15 degrees off crest for no filter, -10 degrees off crest for 3 THz and -8 degrees off crest for 1 THz, although partial loss of energy recovery was observed once the gradient reached -17 to -19 degrees off crest reducing the THz signal at these phases and so it is possibly skewing the data. To regain energy recovery some changes to the dipoles in arc1 and arc2 would be required, which in turn would affect the position the bunch travels through the chicane, changing the source position and so having an affect on the THz signal, that would not be good to do, as it would not be possible to suggest whether the effects were due to linac phase or linac phase and steering. Therefore although these results do show an interesting dependence on the linac phase, they must be taken as a basic comparison rather than a thorough study.

A further experiment was completed to establish the linearity of the train length on the THz signal using the filters. As mentioned earlier, the train length dictates the number of bunches in the train, at 100 μsecs there are 8125 bunches, 40 μsecs there are 3250 bunches etc. The results are shown in figure 4.54.

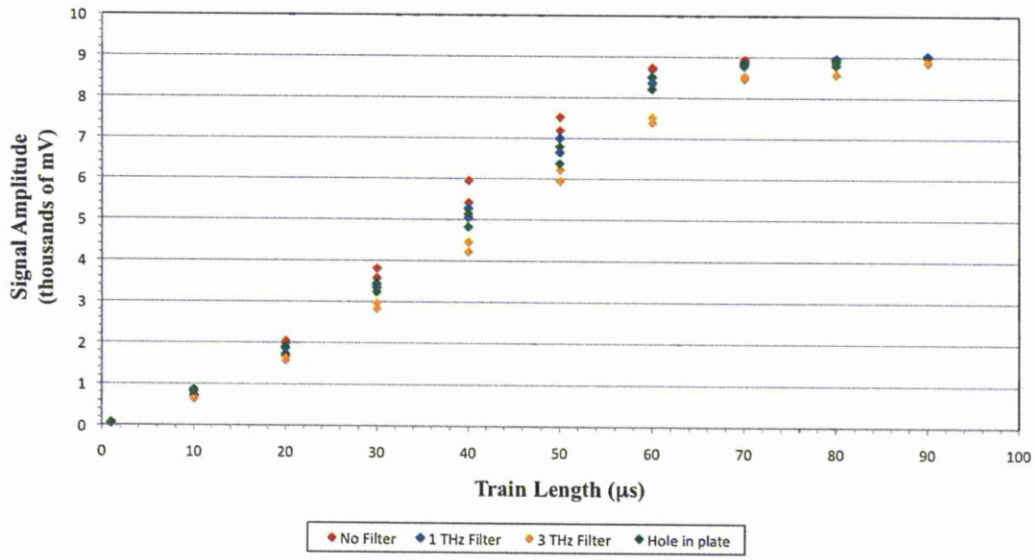

Figure 4.54. Linearity of THz signal with filtering to train length.

The results clarify the linearity of the THz produced, at all wavelengths with train length, however the detector clearly saturates at train lengths >60 μs. The error in these measurements was within 1 mV, therefore it is difficult to make vast conclusions on the differences between each filter.

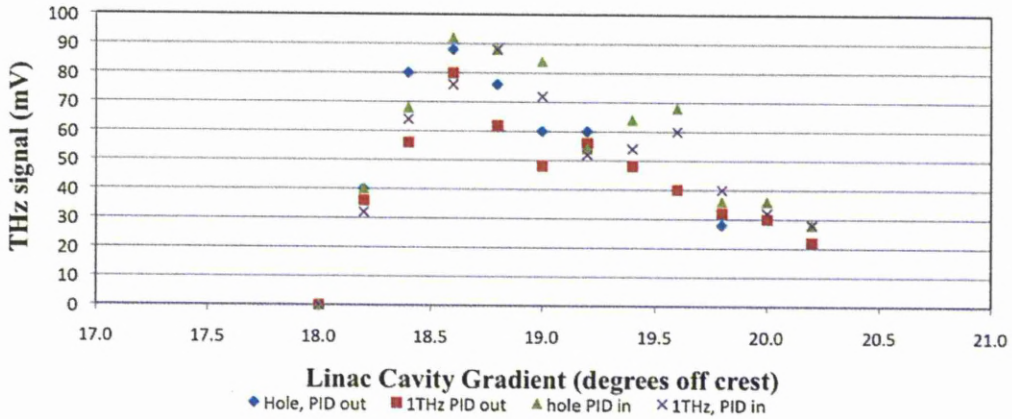

Figure 4.55. The effect of changing the gradients on linac cavity 2 on THz signal with and without a 1 THz filter and with the pop in dump (PID) in and out. Error in measurement is +-5 mV.

Figure 4.55 presents the effect of linac cavity gradient on the THz signal detected with and without a 1 THz filter, and with and without the PID in the line of the beam. The PID, as mentioned earlier blocks the electron bunch prior to the main linac, preventing energy recovery. However it is thought that the returning bunch

could have an affect on the outgoing bunch. It is not possible to run the machine for long periods with the PID in place, however when used at short periods, it allows the accelerator physicists another tool to further understand the machine settings and their affect on THz production. Generally, with the PID in the THz signal improves at all linac gradient settings. This would seem to confirm that there is an affect of the incoming decelerated electrons on the bunch being accelerated, however the difference is dependant on linac gradient phase as expected. It is possible that with further machine alterations, magnet and RF settings in the buncher that this affect can be minimized. It has been shown in some shifts that the insertion of the PID has no affect.

The final experiment was to check the affect of the sextupoles on THz radiation detection. Figure 4.56 shows the affect of changing the power of the first sextupole in arc 1. It was possible to achieve a factor of 2.5 increase in THz by the sextupoles. While changing the second sextupole in arc 1 had no positive affect on THz. The sextupoles in arc 2 were able to improve energy recovery that could allow for alterations to the chicane dipole magnets to maximize the signal further however the detector was saturating prior to any changes so this was not possible.

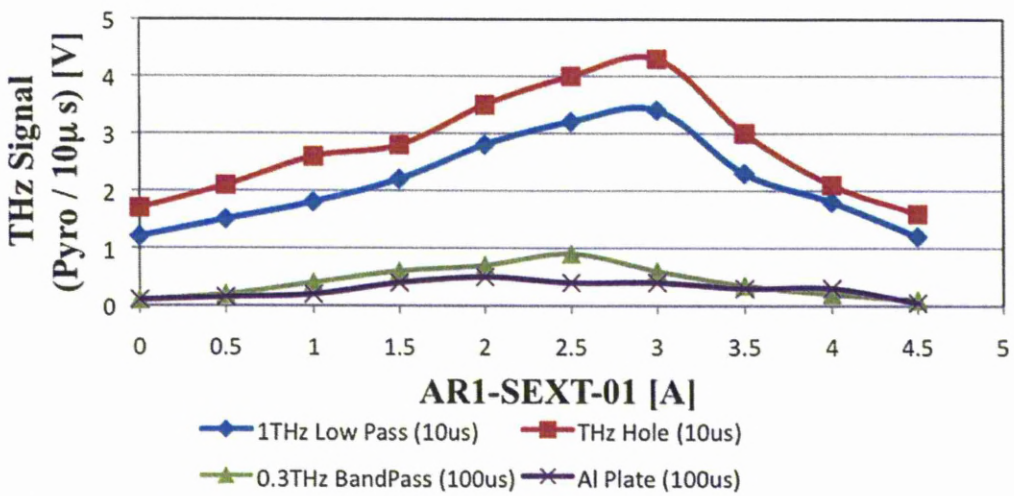

Figure 4.56. Effect of Arc1 Sextupole 1 changes to THz signal with varying the filters.

4.3.21 Final Experiments Prior to Cell Studies

A number of experiments were performed prior to the first cell studies to ensure the accelerator was performing at a sustainable level. Cell exposure experiments required accelerator stability for periods of up to 10 hours. It was therefore vital to

perform some last minute experiments to ensure the accelerator setup (magnet and RF specifications) produced the highest level of THz radiation possible, while being stable for long periods.

4.4 THz in the Diagnostics Room and TCF

In February 2011, THz was detected in the diagnostics room and the TCF. This was a great achievement and was made possible by the development and commissioning of a number of updates to the mirror M1M2 vessel. The requirement for a new design had been born as a result of the analysis of the problems with the THz extraction and transport to the diagnostics room and tissue culture facility. The new upgrade is situated between the diamond window and the mirror M1M2 vessel. The new additions have been designed to provide greater customizability of the THz transport system and allow active live monitoring that can allow alterations to mirror M1 to compensate for the direction the THz radiation leaves the diamond window.

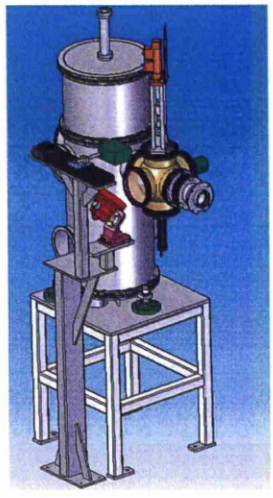

Figure 4.57. The new design for the THz beam line with the new piece in light yellow, six way cross, sitting before the mirror M1M2 vessel.

The new chamber has been designed and installed and can be seen in figure 4.57 and is located before the M1M2 vessel. The new six way cross vessel is shown in light yellow and is the major new piece of the new design. The red mirror directs the THz radiation up to the "Angel of the North" pyroelectric detector. This is placed on a translatable stage so beam profiling can be performed in this position.

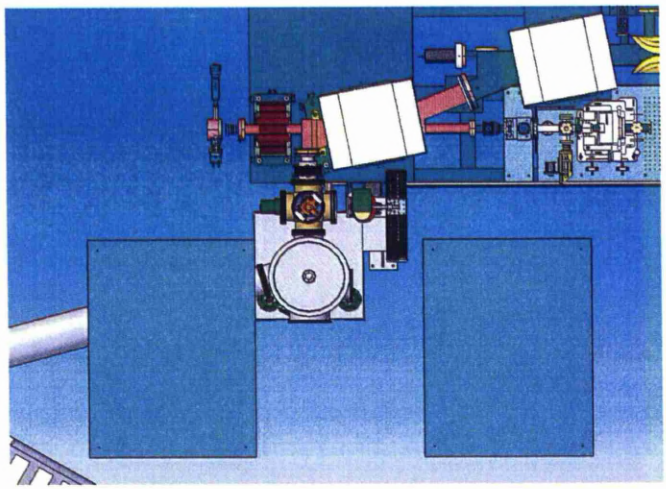

Figure 4.58. Plan view of the new front end of the THz beam line, with the six way cross positioned between the diamond window and the mirror M1M2 vessel. The blue rectangles are optical benches used for beam length monitoring.

The advantage of the six way cross vessel is to allow the THz beam to be extracted and deflected upwards with a plane mirror for beam profiling at 1 m from the diamond window (at the "Angel of the North" position). This also makes it possible to measure the THz at the diamond window automatically. The benefit of being able to measure the signal close to the diamond window at any point, without a requirement to enter on limited access allows clarification that any change in signal further along the beam line is due to an adaption to the beam line *e.g.* movement of mirror M3, rather than a change in accelerator conditions. The control of the new vessel from outside the accelerator room will facilitate the transport of the THz to the diagnostics room and beyond, through a number of motorised mirrors. The M1M2 vessel has been adapted so that mirror M1 can be remotely driven out of the beam line to allow propagation to the in hall experiments. This new setup will allow real time THz measurements to be taken at 1 m from the diamond window, before the mirror is driven out of position and the radiation transported further, it is hoped that this will speed up further commissioning.

The initial experiment performed was to generate a profile of the THz radiation after the mirror M1M2 vessel with mirror M1 removed. With this profile calculated the maximum point is marked on the lead shielding that protects the incubator. The incubator is shown on the left of figure 4.59 behind a steel wall, with the light pipe entering the back of the incubator.

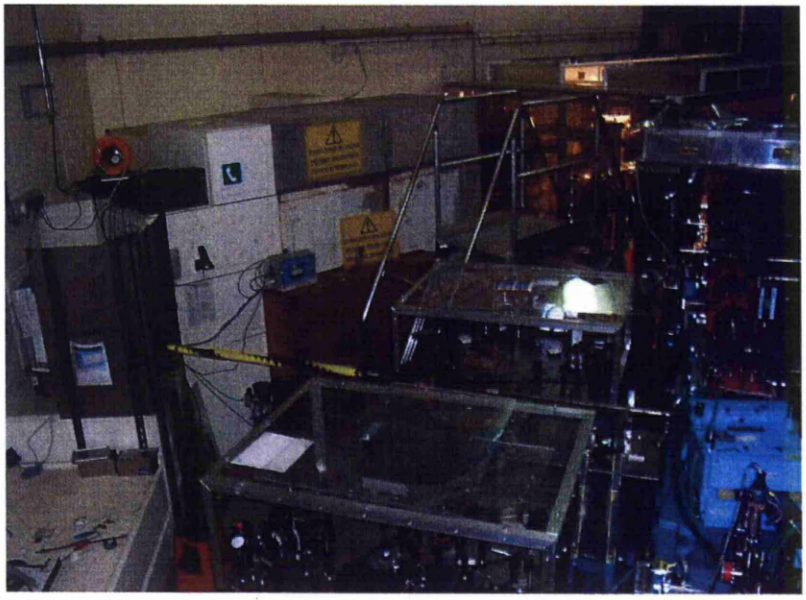

Figure 4.59. A picture showing the ALICE accelerator hall, with the incubator behind the steel shielding on the left of the image, with a light pipe linking it to the diamond window, which is close to the light blue magnet box shown on the right hand side.

The optical laser is then directed on the same optical axis, lining up with the THz radiation leaving the diamond window in order to optically simulate the THz signal reaching mirror M1. This can then be used to align the mirrors downstream from mirror M1 to transport the optical laser to the diagnostic room and onwards to the TCF. This has solved the problem of having no physical source point of THz radiation, and should there be any changes in beam conditions, the adaptations can be made in only a few hours with limited requirement for entry to the accelerator hall via limited access. Figure 4.60 shows the HeNe laser on the left hand side, shining a visible red light through two iris's into the port of the six way cross. This is then deflected by the first mirror, which can be automatically driven into place, on the axis that the THz exited ALICE prior to the 2010 shutdown. The laser position can be used to line up the THz transport beam line, using a reference point that matches the THz source.

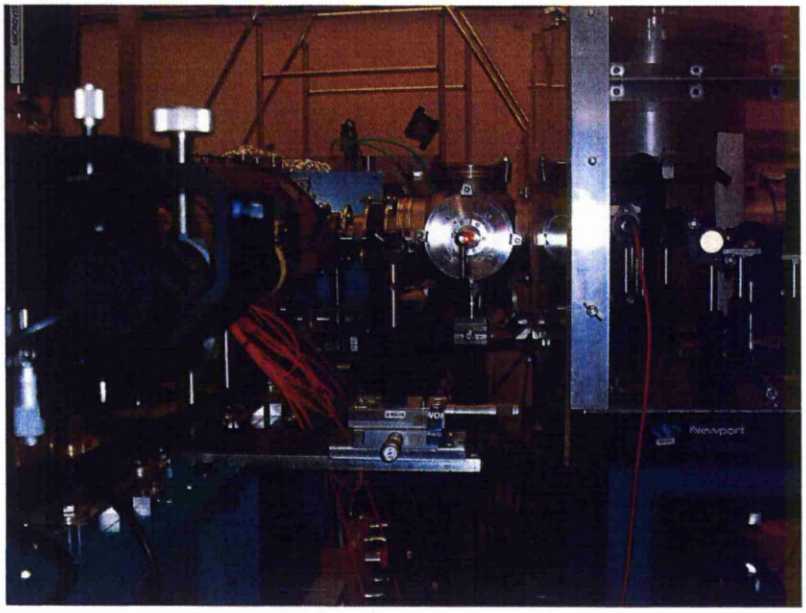

Figure 4.60. The HeNe laser source, close left, shone through to iris's to the port on the new 6 way cross, where the light will hit a mirror and be deflected to the right. The ALICE accelerator electrons travel along the same axis as the laser light, however towards the camera.

During the beam profile studies and the cell experiments, performed prior to the shutdown at the end of 2010, it was noticed that the peak signal was 3.3° from the design centre line as shown in figure 4.61.

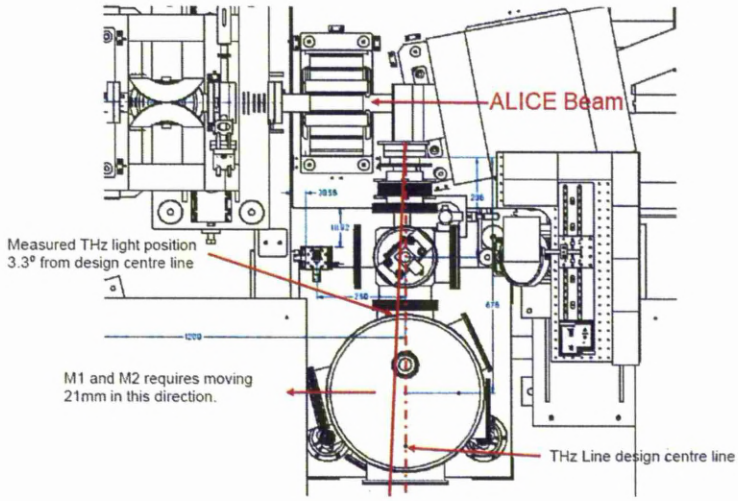

Figure 4.61. This shows the angle of THz from the diamond window, with the dotted line being the design centre line, based on theoretical calculations and the solid red line being the actual experimental results achieved.

As mentioned previously, the THz transport system was designed prior to

ALICE generating THz, and as such, the mirrors were placed in specific positions based on a theoretical model. Due to time pressures this was considered the best option, however in retrospect it was not ideal. Fortunately the new setup allows the maneuver of mirror M1 to allow for this difference, between experimental and design peak THz. This has proved to be very beneficial with THz detected in the diagnostics room and the TCF only weeks after the new designs commissioning.

The beam pipe between mirrors M2 and M3 were removed and the Aux pyroelectric detector was placed at the affective focus of mirror M1, directly between mirrors M2 and M3. This is obviously a rough focus due to the variation in wavelength of light and therefore it is very likely, due to the small active aperture of the detector that only a small amount of signal is being observed. The signal measured was 390 mV, the detector is uncalibrated, however a cross calibration later suggests the signal could be between 15-20 μJ. The detector was moved, requiring access via limited access, to the Martin Puplett spectrometer in the diagnostics room. After a number of tweaks to the mirrors a maximum signal of 600 mV was observed. It should be noted that the beam pipe between M2 and M3 was not replaced, and no sections of the beam line were evacuated. This signal would indicate a potential THz signal of 25-30 μJ. It may look unusual that a larger signal is observed further away from the diamond window, however, this is due to the mirrors in the Martin Puplett spectrometer, allowing more of the signal to be detected by the pyroelectric detector. The detector was then placed in the incubator in the TCF. The aperture of the TPX window in the incubator is larger than that of the aperture of the detector, resulting in an inability to collect all the THz signal. This is made more difficult due to the Winston cone at the end of the beam line, which despite collecting all the THz and focusing it to a smaller aperture, it results in the beam propagating at many angles. Therefore it is impossible with the detector available to measure the full signal being received in the TCF. The signal achieved, with a number of small modifications to mirrors was 350 mV, which suggests a THz signal of 12-17 μJ. The accelerator conditions for this study where 27.5 MeV, 60 pC and 100 μsec train length, however the machine rep rate was halved to ~41 Hz. This allows for a larger bunch charge which allows for a higher peak THz signal, with a similar average power. This method is discussed further in the Zebra fish chapter, as it was used for a number of the later exposures.

A few days later the experiments were performed again with the advantage that the calibrated large area detector was available. The accelerator was optomised for THz generation using the pyroelectric detector on the new "Angel of the North" position that is shown in figure 4.57. The mirror was then translated away so that the light would pass onto the diagnostics room and the mirrors were maneuvered to maximise the signal detected on the pyroelectric detector housed in the Martin Puplett spectrometer. Once the signal was optomised, the power meter was taken into the accelerator hall and placed in the same position as the pyroelectric detector to get a calibrated value. The signal detected was 58 mV (~ 25 μJ). The detector was then moved to the diagnostics room where a signal of 10-12 mV (~ 5 μJ) was observed. This is a transmission efficiency of 20 %, which is not dissimilar to the transmission that was predicted by Marion Bowler for wavelengths of 8 cm^{-1} [5]. A measurement was then taken in the TCF with a signal of 3.8 mV (1.5 μJ) observed. This was the first calibrated power signal observed in the TCF and would suggest peak power levels of 8.5 W and an average power of 0.7 μW. Further work is required to ensure maximum collection of THz radiation from mirror M0 to ensure maximum THz signal received at the TCF. The efficiency of the beamline is similar to theoretical values, however there is a belief that improvements can still be made, especially between the diagnostics room and the TCF.

4.5 Conclusion

During the commissioning of the THz transport system at ALICE a number of important findings have been uncovered and a lot of progress has been made. At the time of writing THz radiation has been detected in the diagnostics room and TCF, however absolute measurements are limited and no spectral data has been possible. This has been due to an instability in THz intensity making it difficult to gain an interferogram. Despite this, the detection of THz in the TCF was considered a great achievement and was only made possible through the development and commissioning of a new front end to the THz beam line which was installed in early 2011.

Previously it had proven difficult to transport THz radiation through the diagnostics room and beyond with a number of potential problems analysed and tested. A thorough beam profile study of the accelerator suggested the problems lay in how it propagates out of the diamond window. Studies have been performed to

understand the horizontal and vertical profiles of the THz radiation at certain distances from the diamond window and indicated that the THz radiation was not propagating from the diamond window on the originally designed axis resulting in a huge loss in THz signal before the M1M2 vessel.

Further analysis, including work on theoretical models discovered that the THz radiation detected at the diamond window was resulting from two different sources within the chicane. Performing power studies at the diamond window may well have been a loss leader. Despite the ability to change the accelerator settings to maximize the THz signal observed, the way in which the THz was being generated may not have been preferential. Experimental and theoretical results suggest that there could be two sources of THz radiation that have been producing these large signals. The two sources are believed to be the designed source from the THz radiation produced in dipole 4 of the magnetic beam compression chicane, and the other is thought to be THz created due to compression earlier in the chicane, and propagating out of the diamond window following numerous bounces/reflections inside the beam pipe.

The THz has provided a vital diagnostic in further commissioning the ALICE accelerator and studies have shown that the THz signal responds to changes in accelerator conditions as would be theoretically expected (*e.g.* linear response to train length, quadratic response to bunch charge). Early laser optics experiments performed have indicated that bunch lengths of 0.8 ps RMS are achievable (on that occasion) which is reasonably consistent with the experimental results achieved on the THz with respect to the power levels expected from theory (0.8-1.0 ps RMS).

Future work should concentrate on the new front end of the THz transport system. This will allow for the first time THz to be monitored close to the diamond remotely while being able to transport the light further, measuring it for example in the diagnostics room. This will allow an understanding of the beam transport system that has not been possible up to this point. The new section will also allows mirror M1 to be translated out of position to allow the THz radiation to continue to the incubator in the accelerator hall as was done late in 2010. Further beam profile studies using the filters available will give a greater understanding on the accelerator conditions and use of the filters measuring the THz radiation received at different points in the transport system will allow a greater understanding of its efficiency.

A priority also must be the spectral properties of the THz radiation as this

will allow for greater understanding of the accelerator conditions as well as biological investigations.

4.6 References

[1] STFC (2010) Accelerators and lasers in combined experiments. "online" (2011) http://www.stfc.ac.uk/ASTeC/Programmes/17425.aspx (13/09/2010)

[2] G.P. Williams, *Reports on Progress in Physics,* **69**, 301 (2006)

[3] J. Alexander, P. Atkinson, R. Bate, C. Beard, N. Bliss, M. Bowler, I. Burrows, R. Buckley, S. Buckley, J. Clarke, P. Corlett, G. Cox, P. Dickenson, M. Dufau, D. Dunning, B. Fell, A. Gallagher, K. Gleave, P. Goudket, S. Griffiths, A. Goulden, J. Herbert, C. Hill, S. Hill, P. Hindley, F. Jackson, S. Jamison, J. Jones, L. Jones, A. Kalinin, N. Marks, B. Martlew, P. Mc Intosh, J. Mc Kenzie, K. Middleman, B. Militsyn, A. Moss, I. Mullacrane, B. Muratori, A. Oates, J. Orrett, P. Phillips, M. Poole, S. Pattlwar, G. Priebe, P. Quinn, R. Rotheroe, Y. Saveliev, D. Scott, B. Shepherd, R. Smith, S. Smith, J. Strachan, G. Stokes, M. Surman, N. Thompson, B. Todd, P. Warburton, T. Weston, A. Wheelhouse, P. Williams, C. White, G. Hirst, P. Huggrad, W. Flavell, E. Seddon, P. Weightman, P. Harrison, D. Holder, G. Holder, K. Harada, G. Neil, K. Jordan, F. Hannon, C. Hernandez, F. Gabriel, P. vom Stein, C. Gerth. IEEE Particle Accelerator Conference (2009).

[4] M.A. Bowler, Transport of THz radiation from ERLP to the tissue culture facility. *Internal Transcript on THz radiation transport, Version: 1.2.* (2007) Accessed: 06/06/2009.

[5] H. Clive. Extraction of Terahertz radiation with new vacuum chamber to increase vertical aperture. *Project Engineering Design Group: Erlp_Terahertz Extraction, Version 0.1.* (2007) Accessed: 06/06/2009.

[6] J.A. Clarke. *The science and Technology of Undulators and Wigglers.* Oxford Series on Synchrotron Radiaiton 4. Oxford Science Publications. 16 (2004)

[7] M.D. Roper, Analysis of measured profiles of the THz dipole output from the ALICE accelerator. *Erlp_Terahertz Extraction, Version 1.* Accessed: 04/08/10

[8] M.D. Roper, A ray-tracing study of the effect of source movement on the output beam of the ALICE THz dipole beam line. *Erlp_Terahertz Extraction, Version 1.* (2010) Accessed: 04/08/10

[9] M.D. Roper, Baffles for blocking scattered light on ALICE THz port-first ideas. *Erlp_Terahertz Extraction, Version 1.* (2010) Accessed: 04/08/10.

[10] M. Borland, (2000) ELEGANT: A flexible SDDS-compliant code for accelerator simulation. *Advanced Photon Source LS-287*, September 2000.

[11] Saveliev. Verbal communication. (June 2010)

Chapter 5. Zebra Fish Embryo Exposure

The aim of this chapter is to discuss the initial THz exposure experiments of Zebra Fish embryos at the ALICE accelerator. The initial experiments provide interesting findings and suggest better methods for future exposure experiments.

At this time, there is limited understanding of the effects of THz radiation on biological systems. Some of the previous work both experimentally and theoretically have been discussed in chapter 3. There are many potential uses for THz radiation, including 3D imaging of human tissue *e.g.* teeth, detection of epithelial cancer and applications in manufacturing processes, security and communication. However as yet there is no knowledge on the potential damages/effects that could be induced by the absorption of THz radiation by living cells.

The Liverpool group have built a Tissue Culture Facility (TCF) on the ALICE beam line which can provide high peak power, low average power THz. The TCF and the THz beam line were built thanks to funding by the UK North West Development Agency (NWDA) and the University of Liverpool. The development allows for further research into the controversial Frohlich hypothesis concerning mechanisms of biological organisation, which is discussed in chapter 3. The TCF was designed to ensure it satisfied requirements for work on cancerous tissue and is equipped with a CO_2 incubator and a microbiological safety cabinet. Both of which have apertures built into the bottom to allow THz radiation exposure. This presents the unique ability to grow human tissue and, while in conditions that are suitable for its growth, directly expose the tissue to radiation from the most intense source of broad band THz radiation in Europe. It is the only facility of its type in the world to perform studies on human cells that will provide answers to a number of key and currently unanswered questions.

There are a number of experiments planned to provide more information in three key areas. Firstly, with the increased development of THz radiation based security screening devices, it is likely that the general public will be increasingly exposed to THz radiation. Therefore it is crucial that an understanding of the effects of repeated low dose exposure to THz radiation are obtained. Secondly, there are already low power THz systems used for the characterisation of cancerous tissue removal in surgery and further techniques and systems in development to aid in the diagnosis of skin cancers. However with low power sources, it results in great difficulty in performing and generating accurate clinical protocols. Thirdly, in an attempt to investigate the theoretical ideas on the drivers for molecular organisation, pump probe experiments with optical techniques are planned which will allow real time analysis of protein folding, which may lead to further understanding of the

mechanisms behind this long unanswered question. The facility at ALICE allows all these experiments to be performed, and provides an interesting and potentially succesful future for THz research.

This chapter discusses the preparation of the THz beam line and ALICE accelerator for cell exposure experiments in the accelerator hall, followed by a study of the affect of THz radiation exposure on zebra fish embyros. A number of other cell studies have been performed but are not covered in this thesis.

5.1 Preparing the Accelerator for Cell Exposures

During the commisioning of the ALICE THz beamline, it proved difficult to transport the THz to the tissue culture facility, as discussed in chapter 4. As a result of these difficulties it was decided to perform THz exposure experiments on a number of different cells in the accelerator hall. A number of meetings were held and it was decided to move an incubator into the accelerator hall and place it by the shield wall near to the diamond window.

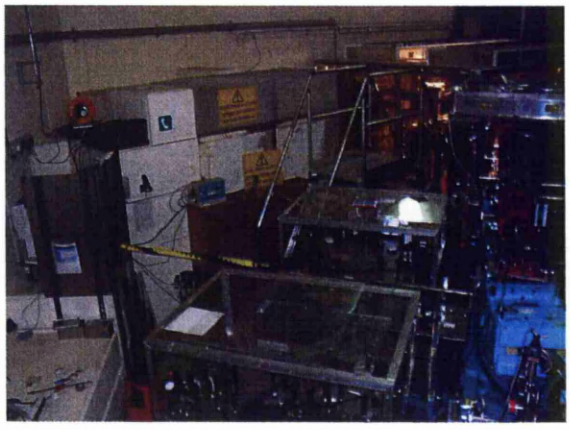

Figure 5.1. The accelerator hall showing the pipe between the diamond window and the incubator. The incubator is positioned on the right hand side behind the steel wall. The pipe runs from the back of the incubator all the way to the diamond window on the left side of the image.

Figure 5.1 shows the accelerator hall with the incubator located on the left hand side, behind the metal sheeting and next to the concrete shield wall. The diamond window is located above the light blue square magnet (this is the fourth dipole magnet in the chicane) on the lower right hand side of the picture. The electrons pass through the chicane and travel upwards in the photograph. There is a light pipe situated at the diamond window that transports the THz radiation to the

incubator. This is made possible by the removal of the mirror M1M2 vessel (normally located in the centre of the picture, where a colleague is standing).

The position of the incubator was limited to the shield wall due to health and safety concerns (ensuring no walk ways are blocked) however this was quite beneficial. Once the M1M2 mirror vessel was removed, initially for beam profile studies, an optical table was installed in its place and a beam profile was taken using settings that would be used for future cell exposure experiments. The maximum position of intensity of the THz radiation was located and marked on the optical table. A straight line was then taken from the diamond window, intersecting this point, to the incubator. With only a small manipulation this was possible and a copper light pipe was manufactured and inserted into a hole drilled into the back of the incubator to allow the THz radiation to enter.

A lead shield wall, constructed from nine inches of lead bricks was built between the accelerator and the incubator to ensure no X-rays hit the incubator. Steel sheet walls were constructed to ensure the lead wall stayed in position round the incubator and can be seen in both images of figure 5.2. The beam pipe can be seen wrapped in yellow and black tape.

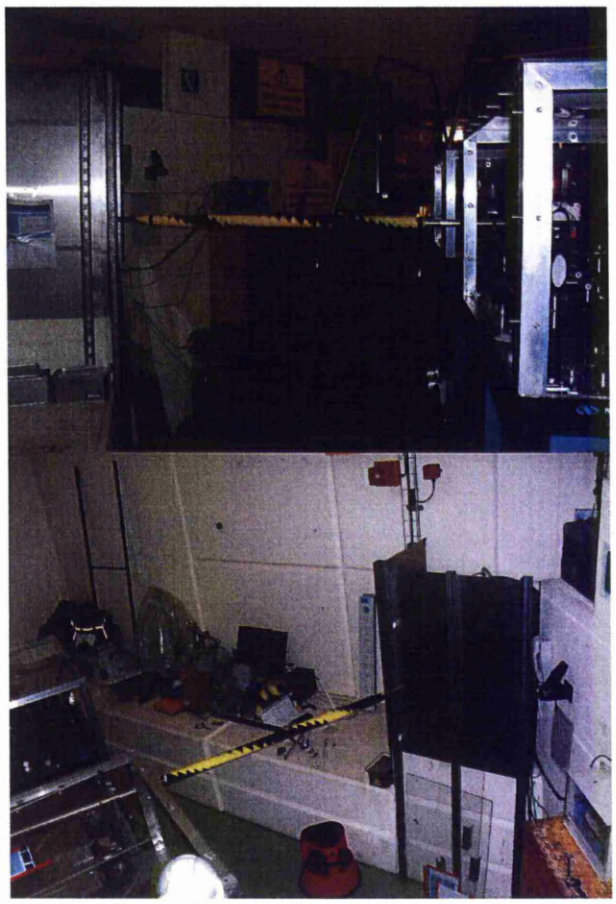

Figure 5.2. Pictures of the beam pipe leading to the incubator from the diamond window.

The THz enters the incubator straight from the diamond window via the light pipe. It was hoped that the majority of the THz radiation travels directly down the pipe, however the pipe was internally polished allowing the THz to "bounce" along the pipe to the cells. This will result in the power of the THz radiation being maximised, as the losses from reflection on metal are very small at these wavelengths. To test this the pyroelectric detector was placed 1 m away from the diamond window and a 0.2 V signal was detected for 10 μsecs train length, 1 V for 25 μsecs and 3 V for 50 μsecs (all detector values are uncalibrated). The light pipe was then placed between the diamond window and the detector and the signal immediately saturated the detector, as can be seen in figure 5.3. The train length was dropped to 2 μsecs and a signal of 3 V was detected. This suggested the pipe was giving an enhancement in signal of up to 25 times.

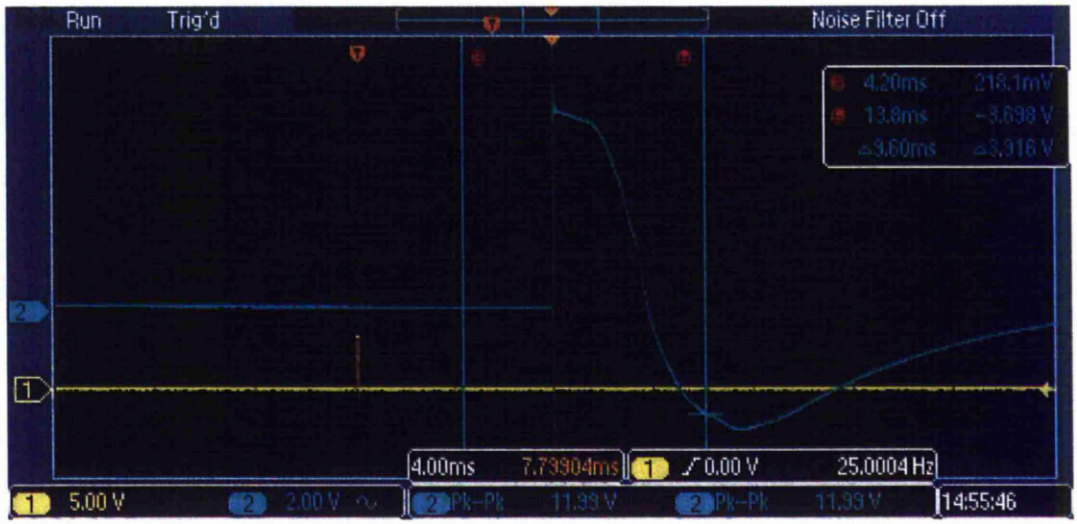

Figure 5.3. The pyroelectric detector signal showing a saturated response to the THz produced once the light pipe was placed between the diamond window and the detector.

Situated inside the incubator is a switch mirror block, which is shown in figure 5.4. The switch mirror block is made out of aluminum and fits onto the light pipe within the incubator. The switch mirror can be remotely controlled, allowing the mirror to rotate to transport THz radiation to either the pyroelectric detector, or the sample position for an exposure.

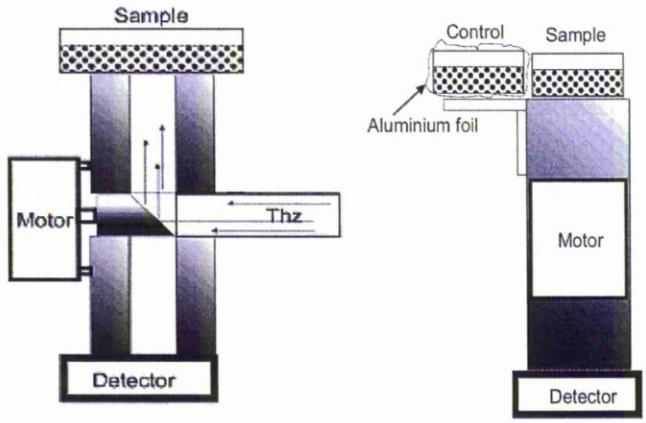

Figure 5.4. View from side of the switch mirror unit, on the left shows the view from the side, the right shows the view from the diamond window.

The cell exposure experiments were designed with a minimum of 3 hours of THz exposure, and there was a concern that the current ALICE accelerator conditions may not be suitable to provide stable THz radiation over a long period of time. This was a new challenge for the accelerator physicists and so careful monitoring of the beam was required, while trying to maximize the signal detected in

the incubator by the pyro-electric detector. There are a number of concerns when running the experiment for this amount of time, so confirming the stability of the accelerator at the optimal settings for the THz cell exposures was performed very rigorously.

The previous studies on biological systems have generally involved low power THz radiation sources. Long exposure times are important in order to further understand the effects of prolonged and or repeated exposures to THz radiation. It is hoped that ALICE could provide an important tool in answering a number of the still unanswered questions, and clarify whether THz modes do play a role in biological organisation, as well as understanding safe exposure limits.

5.2 Zebra Fish Embryos – a Model Biological System

The Zebra fish embryo study described in this chapter was performed in collaboration with Dr Catherine Turner, a biologist with experience of research on Zebra fish embyros.

The Zebra fish (*Danio rerio*) is a small tropical fresh water, benthopelagic cyprinid fish (benthopelagic-live on the bottom or mid waters of a body of water), and is shown in figure 5.5. It has become one of the most important model organisms to study biological processes due to its rapid synchronous development, robustness, large size and transparency. Due to these characteristics it makes it possible for direct observation of xenobiotic (a chemical produced that is not normally expected) induced morphological abnormalities during development. This allows the Zebra fish to be used in ecotoxicological analysis (toxic effect analysis caused by natural or synthetic effects).

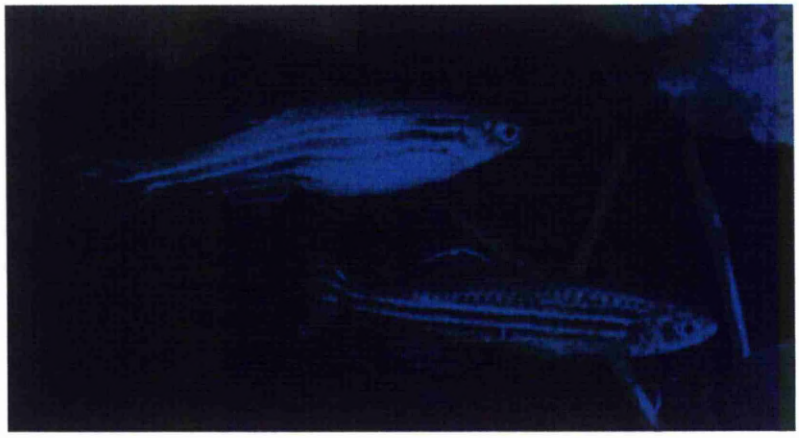

Figure 5.5. The image above shows two Zebra fish, the female is the more rounded bellied above, the male having a reddish tint along his silver lines [1].

Zebra fish embryos are considered to be a model organism. This is suitable for a study of this type because they have the advantage of bringing a wealth of information and validated protocols for their experimental manipulation and study. In addition they undergo rapid development, with a continuously changing system, making them the ideal cell type to further understand THz exposure of biological systems. Due to their rapid development, the regulation of the system is highly complex with any disruption to either the DNA function or protein-protein recognition (which have both been suggested as possibly effected by THz in past work) could provide significant effects [2].

Other advantages of using Zebra fish embryos is that prior to the point of independent feeding they are not regulated or restricted by law, therefore not requiring a home office project license. Additionally, adult Zebra fish are small in size and produce large numbers of offspring with short generation times, and are very economical to keep in large numbers, consequently being very suitable for large scale investigations.

The Zebra fish for the THz experiments were maintained by Dr Catherine Turner at the University of Liverpool [2]. A brief description of the preparation of the Zebra fish for the THz experiments will now be discussed in the experimental method section for the Zebra fish THz exposure.

5.3 Zebra Fish – Method of Preparation and THz Exposure

Zebra Fish typically spawn in the natural habitat within 30 minutes of daylight, this is simulated in the lab so that removal of eggs can take place at 09:00 each morning, which is 30 minutes after the artificial lights come on. This is noted as being 0 hours post fertilization (0 hpf). After this time the Zebra fish embryos go through a number of developmental stages. A full description of this developmental stages from 0-96 hpf can be found in work by Kimmel *et al.* [3] The embryos were only radiated in the 3-12 hpf stage, which is made up of the blastula period (2-5 hpf), the segmentation period (5-10 hpf) and the early part of the segmentation period (10-24 hpf). These are considered to be the most critical periods in the development stage of Zebra fish embryos, which makes them highly susceptible to any effects by THz radiation or other factors. (The remaining periods, of which the cells were monitored but not radiated, are the pharyngula period (24-48 hpf), hatching period (48-72 hpf) and the early larval period (72-96 hpf)).

The embryo tests were designed with a number of known standardization procedures in mind [4-6], however they had to be modified to allow for the requirements of THz exposure (transport to ALICE, beam exposure time, etc). Two different radiation exposures, in terms of hpf were performed, the first during the blastula/gastulation period (exposures performed during the day) and the second during the segmentation period (exposures run over night). The embryos were observed prior to radiation, immediately after, and at 24, 48, 72 and 96 hpf to monitor any observations or changes. It was hoped that the THz radiation could cause mortality, morphological malformations or any microscopically observable differences to those that were not radiated. The embryos would be exposed to THz radiation for between 3-10 hours and statistical testing was used to determine significant differences between experimental and control samples.

During each experiment there were a maximum of 5 samples. These were the THz exposure sample, a sham control placed in the incubator wrapped in foil, a control that was maintained at University of Liverpool, a pronase control (for dechorionation) and in the later experiments a stage control. The embryos were initially radiated with the chorion on. The chorion is a protective layer that surrounds the embryonic cells, as shown in figure 5.6.

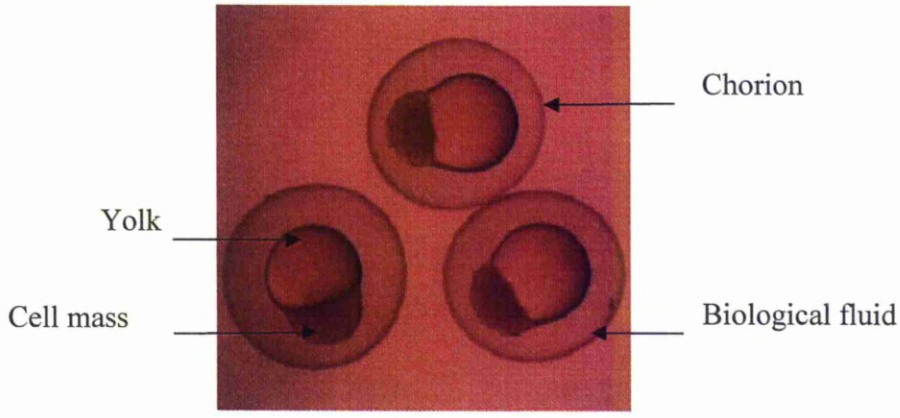

Figure 5.6. Zebra fish embryos (3-4 hpf).

As is shown in figure 5.6, inside the chorion there is a protective layer of biological fluid surrounding the cell mass and the yolk. It was thought that this layer may prevent THz from reaching the cell mass and therefore it was decided to remove it in later experiments. The method for removal of the chorion is to use pronase. This

method results in a large number of embryos and causes no damage to the cell mass or the yolk and therefore allows for large sample sizes to be generated.

The embryo samples being transported to Daresbury, would be taken at the appropriate time with care to the TCF, where they would be prepped for the exposure. Control samples would also be kept at the University of Liverpool in an incubator maintained at 26 ± 1°C (the optimal temperature for Zebra fish cultivation). The incubator, at the University, simulated a 12hr:12hr light/dark photoperiod and the cells were maintained up to 96 hpf.

The samples at Daresbury were prepared in the TCF prior to exposure. The accelerator would be set up to the required conditions to allow a large THz signal and machine stability, as discussed previously. The accelerator would then be ramped down (gun voltage and RF voltage) to allow entry to the accelerator hall via limited access. This allowed the embryos to be transported and placed in the incubator in the correct position, as shown previously in figure 5.4 and the accelerator was ramped up to run for beam. The THz signal and accelerator stability would be checked, and once conditions that were considered suitable where agreed,, the exposure would begin. These conditions would include, the level of X-ray radiation detection on the radmons, and an agreed consideration between high THz signal and machine stability. This would include considering the likelihood of a complete exposure traded off by the highest THz signal possible.

During the exposure a monitor of the X-ray radiation on one of the radmons was collected, as well as periodically (every half hour) checking the THz signal. The machines stability could be monitored by the amount of energy recovery, the demand on the RF and the cryogenics, without causing any disruption to the exposure. If the signal started to drop, which is possible just due to a drop in quantum efficiency of the cathode, tweaks could be made to the accelerator to maintain the THz signal at an acceptable level. These checks would be performed when the mirror was flipped to check the signal. Once the agreed exposure time was complete, the mirror would be switched to directing THz to the detector and the accelerator conditions would be confirmed, before the accelerator ramped down to allow entry via limited access to collect the samples and return them to the TCF for immediate monitoring, and eventual transport back to the University of Liverpool.

The controls are a vital part of any biological experiment. A large amount of thought and care went into the design of the experiments ensuring as many variables

as possible were covered. The control in the accelerator hall was to ensure that there were no effects from conditions in the accelerator hall incubator *e.g.* ionizing radiation, temperature. Controls in Liverpool were used to ensure that there were no effects of transport. The pronase control was used to ensure there were no negative effects of the dechorionation. The staging control was used to see the effect of over crowding in the process. Due to the size of the THz exposure area (18 mm) the embryos were placed in an o-ring in their container, which can lead to crowding. This crowding can result in a developmental slowdown of the embryos (this will be discussed later in the section), however with this control this can be accounted for. This stage control was not introduced until experiment 9. The schematic of the experimental set-up with the stage control is shown in figure 5.7.

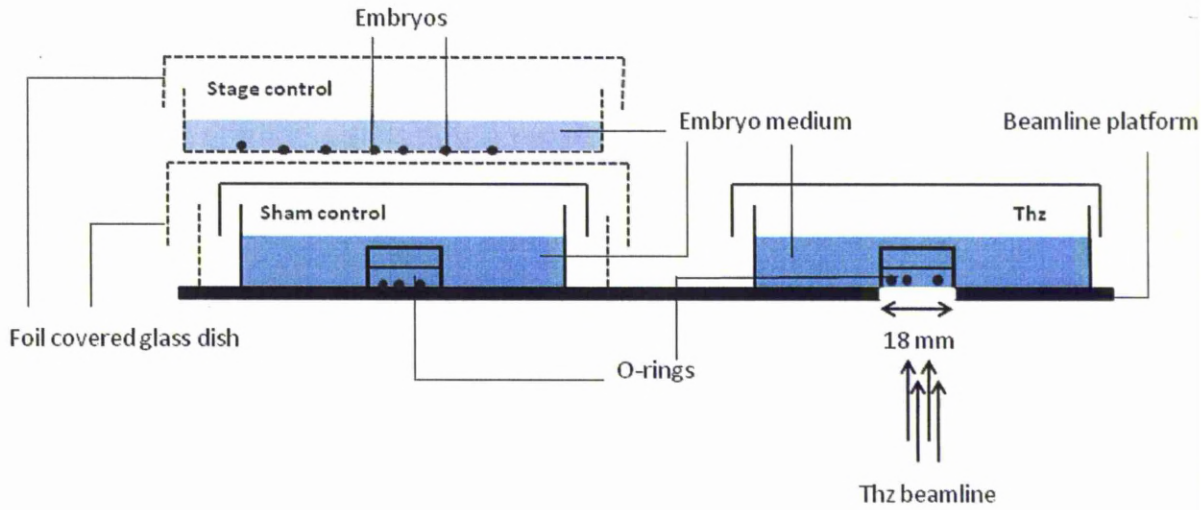

Figure 5.7. The set up of dishes in the incubator showing the exposure sample, sham control, and the stage control.

Once all the samples were returned to the University of Liverpool they were monitored by Dr Catherine Turner and placed in the incubator at 26 ± 1°C and 12hrs:12hrs light/dark photoperiod for up to 96 hpf with removal and monitoring at specific times.

The experiments designed to take place in the accelerator hall are simple exposure experiments. This was always planned to be the initial experiment to understand the effect of THz radiation, however complex analytical assays are not possible to be performed due to the conditions available during the study (the requirement to perform the exposures in the accelerator hall).

5.3.1 Additional Studies to Accompany Cell Work

The experiments were originally planned to take place in the TCF, which was specifically designed for the cell experiments. Performing the experiments in the accelerator hall causes a number of issues, some mentioned previously. Firstly, the experiments performed have to be simplified so that they can be performed safely in the accelerator hall, unmanned. An incubator was sourced and adapted to allow THz radiation to enter it. However the way in which it enters is not ideal. A hole had to be drilled through the back and left open to allow a pipe to be inserted in. Although all care was taken with this, the incubator is not as stable as the one in the tissue culture facility due to this. Issues with the stability of the incubator where emphasised by the temperatures in the accelerator hall. The temperature of the TCF environment can be controlled through the air conditioning, however the warm atmospheric temperature in the accelerator hall means there is a danger that the heat could rise above 26°C. There are many components in the accelerator hall that are constantly on, generating heat. In addition the rotary mechanism of the mirror motor placed inside the incubator does create heat. Unfortunately the incubators do not possess a facility to cool, therefore, a number of tests were performed to ensure that the temperature did not reach a temperature that could cause damaging effects to the Zebra fish embryos. Experiments also took place at the University of Liverpool monitoring temperature effects on separate Zebra fish samples to gain an understanding of what might be observed.

Further experiments were performed to ensure there was no temperature effect from the THz radiation in order to ensure any effects seen from any of the cell experiments were due to the THz radiation rather than any thermal variation effect from the THz. A basic theoretical calculation suggested that the maximum temperature increase of 2°C would be seen, assuming that all of the THz generated is absorbed in the first 50 μm and then using a high value for the waters thermal capacity. However this would be a worst possible case scenario. An explanation of the calculation now follows.

The calculation assumes an average power of the THz radiation of 16 mW. This is taken from the theoretical values in table 4.1.

$$\text{Energy per pulse} = 16\text{mW}/(8125 \times 20) = 9.84 \times 10^{-8}\text{J} \qquad \{4.1\}$$

8125 is the number of bunches per train and 20 is the number of trains per second. The next step is to calculate the mass of the water being heated. As mentioned it is assumed that all the THz radiation is absorbed in the first 50 μm. Therefore it is important to understand the pulse footprint with an aperture of 1 cm radius.

$$\text{Pulse Footprint} = \pi r^2 = \pi \times 0.01^2 = 3.14 \times 10^{-4} \text{m}^2 \quad \{4.2\}$$

$$\text{Slice volume} = 3.14 \times 10^{-4} \times 5 \times 10^{-5} = 1.57 \times 10^{-8} \text{m}^3 \quad \{4.3\}$$

$$\text{Slice mass} = 1.57 \times 10^{-2} \text{g} \quad \{4.4\}$$

The slice mass is calculated as water has a density of 1000 Kg/m^3. It is now possible to calculate the temperature change per pulse using equation 4.5.

$$Q = cm\Delta T \quad \{4.5\}$$

Where Q is the heat added in Joules, c is the specific heat capacity of water (4.18 J/g°C) and T is temperature in °C. Rearranged for temperature change gives you equation 4.6. This is the temperature change per pulse.

$$\Delta T = \frac{Q}{cm} = \frac{9.84 \times 10^{-8}}{4.18 \times 1.57 \times 10^{-2}} = 1.5 \times 10^{-6} °\text{C} \quad \{4.6\}$$

Therefore if there was no heat loss the total heat increase per second, 8125 pulses, 20 times a second, would result in a temperature increase of 0.2 °C. This would be in an insulated system where there was no temperature loss, with all the THz absorbed in the first slice. If the thermal convection of water (500 W/mK) is considered to be the only way the heat can be dissipated, this would disspiate the heat in such a manner that the maximum temperature increase possible over a 10 hour exposure would be 2°C. This considers that THz radiation is the maximum possible generated from accelerator conditions at a maximum, which are yet to be achieved.

The experiment to clarify any temperature effects used a thermocouple device that measured the temperature every 10 seconds. Figure 5.8 shows a control

experiment that was performed to measure the effect with no THz. This was to understand the effect of the incubator in the accelerator hall, with the switch mirror motor on. This would indicate any positional difference with the THz sample being closer to the mirror motor, as shown in figure 5.4 and 5.7 previously.

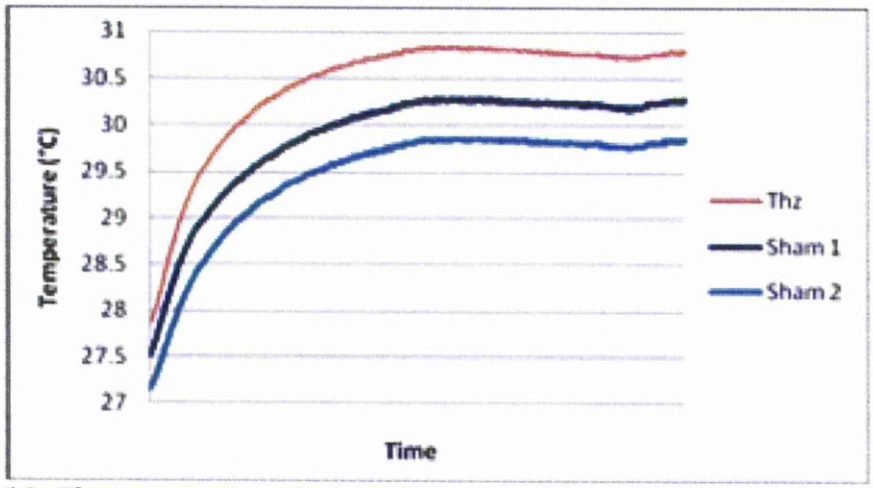

Figure 5.8. The temperature change of embryo medium in THz and sham control containers over a 3 hour period with no THz radiation. There are two thermocouples in each, however one of the THz containers thermocouples failed.

The results in figure 5.8 show a sharp increase in temperature initially. This is due to the placement of the sample in the accelerator hall incubator. The temperature of the incubator was known to be closer to 30°C than the preferred 27°C, due to the inability of the incubator to cool as previously mentioned. The accuracy of the equipment is reported to be 0.2°C, with a reading error of 0.5°C. Therefore the difference between the two sham control thermocouples is considered negligible with only a small difference between the sham control and the THz exposure position, a maximum of roughly 1°C.

Figure 5.9 shows the effect of the THz radiation on the temperature. The monitoring of the temperature took place during study 12. The initial increase is due to the stabilization of the samples as they are placed in the incubator, as in the dummy run in figure 5.8. The sham control actually shows the highest temperature, but as discussed before when taking the errors into account there is little or no difference (0.5°C max). The rapid drop off at the end is once the thermocouples have been removed from the containers at the end of the experiment. This indicates that there is no heating effect of the THz radiation, nor is there a consistent temperature difference due to the switch mirror motor. In study 12 the accelerator settings were

changed resulting in a different timing structure, ~40 MHz bunches, instead of 81.25 MHz. This results in half the peak power, however the bunch charge was changed from 40 pC to 70 pC. It has been discussed in previous experiments that the THz is quadratically dependant on bunch charge, this means that the peak power will be larger, without having a large effect on the average power. Even if the peak power were doubled, the average power would be the same.

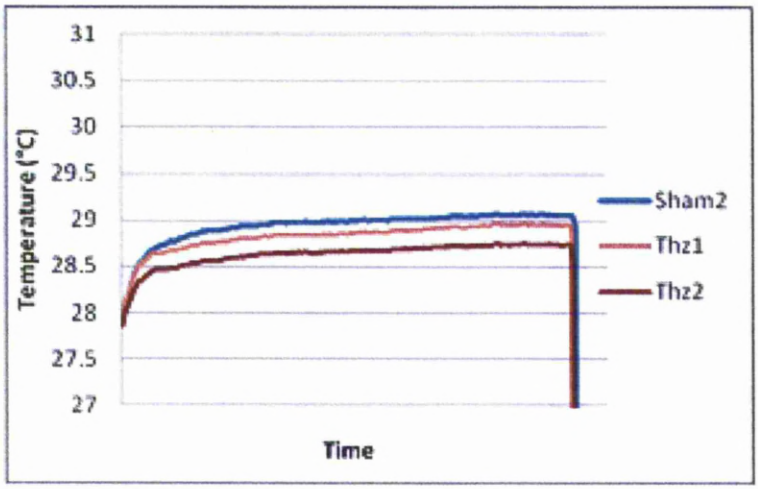

Figure 5.9. shows the temperature study of the THz and sham control samples in the incubator while there is THz exposure of 10 hours. One of the sham control sample thermocouple's was not working.

However as previously mentioned temperature issues are not only linked with THz, although THz is the only independent heating difference between the THz and the sham control. The incubator struggles to maintain the ideal temperature for Zebra fish embryos, especially on hot days.

The second issue in performing the experiments in the accelerator hall is the possibility of ionizing radiation. The accelerator is in a controlled radiation area, which is monitored by a number of radmon detectors around the accelerator hall, and in surrounding areas, including the tissue culture facility. All radiation detectors are linked to a hard routed personal safety system that trips the accelerator if the ionizing radiation levels become higher than what is considered safe, in areas that people can be located. However in the accelerator hall the radiation levels can get higher than what is considered safe, which is why the access is controlled by the personal safety system.

The sources of radiation are from the linac and from beam losses, which produce bremsstrahlung X-rays when the electron beam strikes the side of the beam pipe. It is also possible that some X-rays are generated by back scattering of the electron beam from the dipole upstream of the linac, which would be diverted towards the area where the FEL, diamond window and incubator are located.

In an attempt to minimize ionizing radiation extra lead shielding around the incubator was installed, as discussed earlier. A radmon detector is positioned next to the incubator, and the data from the detector is automatically collected during each exposure, giving a value in μSv/hr. A Sievert (Sv) is the SI undits of dose equivalent radiation evaluating the biological affects of radiation. During later exposures a more detailed X-ray study was performed. This involved locating a number of thermoluminescent dosimeters (TLD's) in and around the incubator. Two were placed next to the cell samples, the control and the exposure, with an array of detectors at the door of the incubator, and a number of others placed on the beam pipe and in strategic positions close to the incubator. These dosimeters are usually placed in a polythene modulator to calibrate the TLD's. However due to the size limitations in the incubator and the design of the array this is not possible. Therefore two detectors are used as a calibration, one strapped to the outside of a polythene modulator and one inside. The TLD's are then processed by the health science department at Daresbury and a cumulative dose value is given which can be compared with the radmon readings by taking into account the time of exposure.

The annual dose limits specified by the Ionising Radiations Regulations 1999 for employees aged 18 and over is 20 mSv for the whole body effective dose. The equivalent doses to the lens of the eye is 150 mSv, to the skin, averaged over 1 cm^2, is 500 mSv. The whole body effective dose limit of 20 mSv per year is what should be compared to the radmon readings [7].

During each study radmon readings were taken. Typically the ionizing radiation levels never went above 60 μSv/hr, with a usual range of 40-60 μSv/hr. However there were some instability issues during studies 4 and 5 that saw large spikes of radiation up to 250 μSv/hr, though only lasting less than a second. This could be due to a number of things, including a sudden beam loss due to an unexpected beam load on the bunch (an unusual energy distribution along the bunch train, resulting in losses in the chicane).

In study 7 the radiation levels were slightly higher, 50-100 μSv/hr, with very high levels monitored during study 9 of 100-200 μSv/hr. In this study there were a large percentage of effected embryos (high mortality rates) in both the THz and Sham control. The TLD readings are shown in table 5.1. (The TLD's were placed on the top of the sample containers.)

Table 5.1. TLD readings for the THz and sham control samples in the incubator.

Treatment	Study 9		Study 11		Study 12	
	(μSv)	(μSv h^{-1})	(μSv)	(μSv h^{-1})	(μSv)	(μSv h^{-1})
THz	4523	476.11	1178	124.00	1327	132.70
Sham control	6338	667.16	914	96.21	985	98.50

Despite the high values seen, these values are still lower than levels required to effect Zebra fish embryos according to Geiger *et al.* [8]. The levels seen are also lower than the safety levels for human exposure, discussed earlier. It should be noted, that the TLD readings are not 100 % accurate. TLD's are usually used in polythene moderators, which act as a way of them being calibrated, however this is not possible in the incubator due to space restrictions, as mentioned previously. Therefore the values should be used as a rough guide.

To understand the radiation in the incubator further a TLD array was prepared and used in studies 11 and 12. This was placed at the back of the incubator and produced a spatial distribution of radiation to the incubator, which will give more understanding of the effect of the shield wall and where the THz is coming from. The results of the array are shown in table 5.2.

Table 5.2. TLD readings for the array placed at the back of the incubator in the accelerator hall, it is shielded by the lead. Units are in μSv.

Study 11

Top left			Top right
1890	2139	2022	2491
1429	1817	2022	1693
1191	1429	1360	1898
1300	1358	1410	2073
841	1030	1025	1322

Study 12

Top left			Top right
2871	3654	3640	2491
1773	2088	2542	1693
1751	2110	1934	1898
1364	1883	2242	2073
1154	1256	1971	1322

The results in table 5.2 show there is a positional dependence on the amount of X-ray radiation observed, as do the experiments that show the difference between the sham and THz exposure samples in table 5.1. The difference inside the incubator is the most concerning. As has been mentioned, for studies 11 and 12 the radiation levels for both the sham control and the THz exposure samples are well below the human and Zebra fish safety levels, though there is a difference between the two. This difference was about 30 μSv/hr and it alternated between the two for each experiment (200 μSv/hr in study 9). It is important to ensure that during the accelerator set up the ionization levels on the radmons are kept to a minimum and machine stability is maintained.

5.4 Zebra Fish Embryo Results

The specific details of all the Zebra fish embryo THz radiation exposure experiments are shown in table 5.3. Black dates on the table show experiments that were not performed, due to accelerator issues. Blue dates show the experiments that were performed in the evening/overnight shifts. The red dates indicate exposures that took place during the daytime. The duration is the total number of hours of THz exposure (on some occasions the THz was shut off for a short period due to accelerator issues, and then the exposure continued). The chorionated indicates whether the chorion has

been removed (dechorionated is the removal of the chorion). The "No of treatment", is the number of embryos that are radiated by the THz. The "replicates" is the number of dishes the embryos are transferred into post exposure. THz voltage is the THz signal seen on the pyroelectric detector in the incubator during the exposure. 1 V = 13 μJ, however, the pyroelectric detector begins to saturate at 8 V and above so values above this may actually be larger. The embryo age is the age respective to birth (hpf). The fertilization rate is the estimated percentage of fertilized embryos of those collected, greater than 50 % is considered good. Parental stock is the stock number from where the eggs are collected. The additional studies section show other experiments that were performed, over and above the THz exposure, *i.e.* temperature and ionization studies. Studies 12 and 13, which both have a *, indicate that they were experiments where the accelerator conditions were changed. The accelerator conditions were changed to allow a higher peak power, with a similar average power. This is due to the timing structure and has been discussed earlier.

The difference between the THz treated embryos and the control treatments were assessed on the observations made at 96 hpf. Affected embryos (those that had died) where given a score of 1, with the embryos observed as normal behavior scored 0. A statistical package was used (R Development Core team, 2008) [9]. If the statistical analysis returns a P-value of < 0.05 the result is considered significant. A 10 % effect rate in control treatments is considered acceptable due to spontaneous and genetic abnormalities, (they would see effects naturally). This is used in many zebra fish embryo studies, however this rate is greater than that normally seen within the control groups (average death rate THz 17.37 %, Liv control 7.77 %, sham control 12 % and pronase control 2.36 %).

Table 5.4 shows each of the studies with the percentage of effected embryos and the respective P-values from the Wilcoxon Rank Sum test [10]. This statistical analysis is a non parametric or distribution free test. This means it is not based on any underlying assumptions. It can be used to test the null hypothesis that the median of a distribution is equal to a chosen value. Needs more explanation. A flaw with this type of test is that if it is used a lot of times it can inflate your chances of obtaining a statistically significant result. Due to this, further statistical analysis is required but due to time, has not been covered in this thesis.

The values in table 5.4 will now be briefly explained. The study number corresponds to the relevant study performed with the details shown in table 5.3 and

discussed below. The arrest time is the amount of time in total the embryos have been considered to be in developmental arrest. This is the anoxic response, and is calculated by comparing the arrested embryos with those that have not, noting the difference in their development. Zebra fish embryos have a long studied and well documented developmental cycle and these measurements can be made with an accuracy of within 1 hour. The THz, Liv control, sham control and Pronase control values are all taken as the percentage of dead embryos at the end of the 72 hpf study. Any extra differences between experiments are also explained as well as any issues found with the experiments. The p values indicate the significance of the result between each control and that of the THz exposed sample.

Studies 2-5 all had $\leq$ 5 hrs of THz exposure, and in each there were no significant differences observed between the THz exposure and control treatment embryos.

For the THz exposure experiments where the exposure time was greater than 9 hours, 6 out of the 8 studies had significant differences between at least one of the controls and the THz exposure. During the longer studies it was observed that the embryos went into a developmental arrest/suspension state. This will be discussed further later.

In the studies where the exposure was under 5 hours no major changes where observed. Study 3 did present results suggesting 17.5 % of the exposed embryos were affected, however due to the small sample size this could not be considered significant (3 out of 17). In study 5 the Liverpool control showed a high level of affected embryos which is thought to be due to the embryos being transferred to the replicate plates immediately after de-chorionation. At this point, immediately after de-chorionation, it is difficult to select good embryos, which may result in selecting embryos that are likely to have poor survival rates prior to THz radiation, and therefore in later studies the selection process was done at a later stage. It should be noted that the embryos selected for ALICE THz and control samples are chosen prior to exposure, at Daresbury, rather than immediately after de-chorionation.

Study No.	Date	Duration	Chorionated?	No. per treatment	Replicates	Thz voltage	Thz	Sham control	Liv control	Pro control	Stage control	Embryo age	Fertilization rate	Parent stock	Additional studies
		(h)				min- max (V)						(hpf)	(%)		
1	14/05/2010	-	NOT RUN	-	-	NOT RUN						NOT RUN	-	-	
2	25/05/2010	3	chorionated	60	2	7.8 - 8.5	•	•	•			11.5 - 15	80	133	
3	02/06/2010	4.5	both	20	2	6.5 - 9	•	•	•			10 - 14.5	90	133	
4	10/07/2010	5	chorionated	60	4	6.5 - 9	•	•	•			3 - 8.5	-	133	
5	31/07/2010	4	de-chorionated	40	4	4.5 - 6.9	•	•	•			4 - 8.5	-	133	
6	08/08/2010	10	de-chorionated	40	4	3 - 7.8	•	•	•			4 -14.5	-	133	
7	16-17/08/10	10	de-chorionated	75	4	3.3 - 6.5	•	•	•			13.5 - 23.5	90	133	
8	04/09/2010	10	de-chorionated	40	4	8.5 - 9.5	•	•	•	•		3.5 - 13.5	80	133	
9	11/09/2010	9.5	de-chorionated	40	4	9.1 - 9.4	•	•	•	•	•	4 - 13.5	85	133&134	TLD's (samples)
10a	19/09/2010	-	NOT RUN	-	-	NOT RUN						NOT RUN	-	-	
10b	22-23/09/10	10	de-chorionated	60	4	6.2 - 7.0	•	•	•	•	•	12 - 22.5	90	134	
11	16-17/10/10	9.5	de-chorionated	110	4	7.3-9.0	•	•	•	•	•	14.5 - 24	90	134	TLD's (samples and array)
12*	27-28/10/10	10	de-chorionated	80	4	8.3 - 10.2	•	•	•	•	•	13 - 23	80	134	Thermocouples and TLD's (samples, array, moderators)
13*	29-30/10/10	10	de-chorionated	80	2	9.4-10	•	•	•	•	•	12.5 - 22.5	70	134	TLD's (samples and moderators)

Table 5.3. Specific details for each Zebra fish embryo THz exposure experiment.

During the studies 2-5 there were no malformations observed which would have been formed from any spontaneous deformations. However in study 3 there was a developmental difference between the THz exposed embryos and the sham control. This at first was considered to be a possible THz effect however it was more likely to be due to a temperature difference between the two samples. During studies 2 and 3 it is possible that there was a temperature gradient in the incubator due to the issues discussed previously. In studies 2 and 3 the control sample was kept on the floor of the incubator, while the THz exposure sample was near the roof of the incubator on the mirror assembly stage. This would allow for a temperature variation between the two samples that would be a likely reason for the difference in developmental rate, as this increase has not been seen in further experiments when the setup is like that in figure 5.4, with the control sample next to the THz exposure sample. Work by Kimmel *et al.* [3] and Schirone and Gross [11] has proven that the rate at which Zebra fish embryos develop is temperature dependent. They were able to show that increasing the temperature caused an increase in developmental rate.

As previously mentioned 6 out of 8 long exposure studies (>9 hrs) showed a difference between the THz exposed embryos and a control. These will be discussed in detail now. Out of the 6 studies with a THz exposure of in excess of 9 hours, studies 6 and 7 provided the most convincing results that would suggest THz radiation may adversely affect Zebra fish embryos. In both studies the control treatments effected levels are at an acceptable level with no significant differences between the two control treatments, and a significantly greater number of affected embryos in the THz treated sample. In this study, 6, the THz exposed embryos were observed to be in a much earlier developmental state than the controls, sham control and Liverpool control, suggesting the THz possibly delaying development. This is the opposite effect to what could well have been expected if the THz modes caused a heating effect as any temperature increase would see a developmental rate increase. As mentioned previously it is known that THz radiation could have a warming effect, however due to the ALICE timing structure (low average power) this has been disproved in a later study, mentioned previously, and theoretically calculated. It was considered that the reason for this developmental rate delay could be due to the embryos becoming anoxic (absent of oxygen) which then results in the embryo entering a state of developmental arrest. The reason for the anoxia was believed to be due to a large number of embryos (40+) being crowded into a small water volume for

a substantial period of time. The small water volume they are placed in is due to the o-ring in the cell container that ensures the embryos lie in the path of the THz in the exposure sample. The same set up is performed for the sham control in order to replicate this condition.

Padilla and Roth [12] have shown that Zebra fish embryos can survive in a suspended developmental state for up to 24 hours without seeing any permanent effects and will return to normal once conditions have suitably improved (*e.g.* plated out into replica dishes or replacement of media) [12]. It was thought that in the process of shielding the sham control from THz by wrapping the cell dish in foil could well have displaced some of the embryos from the o-ring, which meant that those embryos would be less crowded and not reach anoxic conditions.

To clarify that the anoxic effect was due to the crowding of Zebra fish embryos and not a THz effect, extra care was taken, from study 7 onwards, to ensure the embryos remained in the o-ring in both the sham control and the THz sample.

In study 7 both the sham control and the THz exposure showed a severe delay in development, while the sham control embryos recovered and developed normally, almost half of the THz exposed embryos died. The fact that both the THz exposed and the sham control embryos went into developmental arrest, suggests that the anoxic effect was solely due to the overcrowding rather than a THz effect, however it also suggested that if the embryos are in developmental arrest this may possibly aid the effects of THz radiation.

Study 8 attempted to perform a long THz exposure without the embryos going into developmental arrest by exposing the embryos to a larger embryo medium volume. This will not affect the level of THz radiation the Zebra fish embyros see, as they will settle at the bottom of the flask. This proved quite successful with most of the embryos showing no delay, with the odd embryo showing a maximum of 1 hr delay. This study showed no difference between the THz and control treatments leading to a new hypothesis to be formed.

The new hypothesis, deduced following the results of the first three long exposure experiments, studies 6, 7 and 8 suggests that the developmental arrest state is vital to see any effect by THz exposure. It is known that when a Zebra fish embryo enters developmental arrest due to anoxia the cell cycle is halted and therefore there is no mechanism active for DNA repair [13]. Bock *et al.* suggest THz radiation will affect DNA. They theoretically propose that a THz energy could create spatially

localized openings with linear instability leading to dynamic dimerization [14]. This is discussed further in chapter 6 where the THz effects on DNA are explored. Therefore it was proposed that if the Zebra fish embryos are in good health when irradiated with THz, they have the ability to self repair their damaged DNA. However, if the Zebra fish embryos are in a developmental arrested state, any damage done during a THz exposure, is not repaired, and once favorable conditions return (through placing in replication plates, or replacement of embryo medium) it may not be possible for the embryo to repair itself resulting in death. Studies 6 and 7 demonstrated a large percentage mortality rate in the THz exposed embryos with normal development resuming in the sham controls. Sadly the results seen in these two studies have not been possible to replicate, so more work is required.

In study 9 there were a great number of affected embryos in the sham control as well as the THz exposure embryos. The X-ray data was assessed and large levels were observed, which would offer an explanation for the high number of affected embryos, and was therefore not possible to make any conclusions in regard to THz effect.

Study 10a was cancelled due to a number of accelerator problems that meant a stable THz exposure was not possible. Studies 10b and 11 saw both sham control and THz embryos go into developmental delay for between 6-8 hours (delay is measured against the control embryos development), however there were no observed differences between the THz exposure and THz sham control samples. Both THz exposed and sham control recovered and developed normally once placed in the replicate dishes.

Study 12 and 13 were the final studies possible prior to the shutdown of the ALICE accelerator in 2010. In study 12 the percentage of effected embryos were significantly greater in the THz treatment than either of the controls, however there was also a significant difference between the two controls themselves. Therefore it is possible the de-chorionation and transportation to ALICE from the University of Liverpool could have caused the effects and even with the larger THz exposure damage, it is not possible to confirm only THz radiation effects. Study 13 had a high effect in the sham control and none in the THz samples. Currently there is no understanding for this, however further care will be taken in future experiments in an attempt to eradicate the potential issues with the controls.

Table 5.4. Results summary of all THz exposure studies.

Arrest is estimated based on max time diff between stage control and sham control/THz exposure [#] No Stage control used in study. Arrest estimate was taken using stage of Liverpool control embryos instead. * Only observed till 72 hpf. [+] Only in Thz treatment, no arrest in Sham control. Significant test result (P-value < 0.05). Larger than ≈ 10 % (baseline rate in controls). Pro = Pronase control, Liv = Liverpool control.

Study No.	Arrest	Effected embryos and P-value compared to Thz treatment							Other significant differences (P-value)	Issues
	(h)	Thz	Liv control		Sham control		Pronase control			
		(%)	(%)	P-value	(%)	P-value	(%)	P-value		
1	n/a	n/a	n/a	n/a	n/a	n/a	n/a	n/a		
2*	none	0.00	1.67	0.34	0.00	1.00	n/a	n/a		Difficulty in keeping embryos over beamline. o-ring stuck down in subsequent studies
3*	none	17.65	0.00	0.06	0.00	0.06	n/a	n/a		Developmental stage difference between Sham control and Thz due to height in incubator
4	none	8.33	3.33	0.25	4.44	0.44	n/a	n/a		Radmon un-stability. Mostly at 25 uSv/h but periods up to 100 uSv/h
5	none	5.00	17.05	0.07	10.00	0.40	n/a	n/a		High Liv control mortality. Plated out too early. Hard to tell quality at this stage
6	< 4[#+]	27.50	5.00	0.0069	7.69	0.02	n/a	n/a		Arrest only in Thz, Sham control ones probably not within o-ring.
7	< 7[#]	49.33	11.25	2.37×10^{-7}	10.67	2.64×10^{-7}	n/a	n/a		Arrest in Thz and Sham. Both had embryos within o-ring. Slightly raised radmon readings.
8	< 1	21.05	12.50	0.40	23.33	0.86	2.50	0.02	Pro + Sham (0.0073)	Embryos sticking badly to plastic exposure dish in Sham control.
9	< 5	28.26	10.00	0.04	40.00	0.29	5.00	4.9×10^{-3}	Liv + sham (0.003), Pro + Sham (3.0×10^{-4})	High ionising radiation levels. Poor Sham control survival. Use of stage control introduced to study design.
10a	n/a	n/a	n/a	n/a	n/a	n/a	n/a	n/a		
10b	< 6	0.00	3.39	0.14	3.17	0.16	1.67	0.31		
11	< 8	6.36	1.25	0.08	8.11	0.62	5.00	0.69	Sham + Liv (0.037)	More arrest in Sham control than Thz embryos
12	< 7	42.50	26.58	0.04	8.75	1.11×10^{-6}	0.00	0.01	Sham + Liv (0.003), Liv + Pro (8.16 x10-7), Sham + Pro (0.007)	Thermocouples may cause damage to Thz embryos
13	< 11	2.50	1.25	0.57	31.25	1.32×10^{-6}	0.00	0.16	Sham + Pro (5.8×10^{-8}), Sham + Liv (3.0×10^{-7})	

5.5 Conclusion and Suggested Future Work – Zebra Fish Embryos

The THz exposure of Zebra fish embryos have offered some interesting results. However despite some positive results that suggest that THz radiation may exert a detrimental effect on Zebra fish embryos, the evidence is not considered reliable at this time due to a lack of reproducibility, nor is it possible to state that THz radiation does not cause detrimental effects. With this in mind a number of conclusions and recommendations are made.

Due to the experimental constraints of performing the experiments in the accelerator hall it could be argued that there were a number of uncontrollable variables that must be overcome in future experiments to clarify the effect of the THz radiation.

The temperature effect of the THz radiation has been proven to be minimal if at all, it was not detected, nor did it cause an increased rate of development, as would be expected based on literature. However temperatures in the incubator must be closely monitored due to environmental effects of the accelerator hall and the inability. Ionizing radiation is a concern, however it can be monitored and when maintained at the lower levels, does not cause an effect in either the THz exposed embryos or the controls placed in the incubator.

One concern with the current set up is the requirement for de-chorionation, transportation and crowding into a small exposure spaced for a period of time. This results in the embryo being placed at the limits of survivability, which would explain the high effect rates in some of the control embryos on some of the longer studies. Although Zebra fish embryos are considered robust, when the embryos are placed at the limit of their survivability it is possible that even very small differences (other than THz) between controls and THz samples can result in significant differences between treatments. Despite not being able to make any firm conclusions from the data the experiments have highlighted some important issues, while solving some, they have given the experience to ensure future experiments can be planned to accommodate any variables not previously controlled.

The dechorionation of embryos less than 10 hpf can result in the embryos sticking to the plastic dish where they will disintegrate. This can create problems with the study of THz results. The embryos that stick to the plastic surface can usually be accounted for and removed from statistical analysis, however this is not

always possible. This made day time exposures far more difficult, with the selection of good embryos far more difficult. In future experiments it would be more suitable to use z cut quartz dishes, which the embryos would not stick to, and the z quartz does not attenuate THz radiation.

One other concern is the position of the embryos during the exposure. When embryos are placed in a dish they will sink to the bottom of the media, however it is not possible to ensure how they position themselves as they sink to the bottom. Figure 5.3 shows the embryos, if the embryo sinks to the bottom with the yolk facing downwards it is possible that the embryo cell mass will not be exposed to THz as the cell yolk absorbs it. This may make replication difficult. Also ensuring equal spacing of embryos within the o-ring is very difficult, almost uncontrollable and therefore may provide an explanation for the differing results between exposures.

One possible positive to come with the restrictive experimental design has been the possible effect of THz radiation on Zebra fish embryos that have entered an arrested state of development. To place Zebra fish embryos in this arrested state conditions have to be set for oxygen depletion in the embryo medium. The current method for this is very crude, and there is no way to control the age at which the embryos enter arrest or the length of time they are arrested for. The development of a controlled method that could control this view would allow for a far better understanding and a proper test of the proposed hypothesis.

Another important issue that must be resolved is an experimental result of the THz spectra. A theoretical one is known, however baring in mind so many theoretical studies suggest that biological systems are only be effected by THz of specific frequencies, no full result can be made until the spectrum is known. One point of concern would be the effect of accelerator changes on the THz spectra. In the later experiments changes were made with the timing structure and bunch charge of ALICE resulting in double the peak power, and the same average power, however if this shifts the spectrum away from a specific frequency that had previously created the effects seen in studies 6 and 7, then the results gained in the later studies could be explained.

In conclusion, it has not possible to conclusively determine the effects of THz exposure on Zebra fish embryos. Further studies are required with an improved experimental design and test system that evolves from the lessons learnt in this study. More complex analysis may be key, work performed by Bock *et al.* [13] suggests

that low power THz radiation with its main intensity at 10 THz effects the rate of gene expression. They show that 6 % of genes expression is increased, with 6 % of gene expression decreasing, while the remaining is unaffected. Work to look at gene expression and protein development may be key. These experiments and many more will be easily possible once it is possible to perform the exposure experiments in the tissue culture facility.

The hypothesis developed that the THz may effect cells in an arrested state due to their inability to repair DNA damage, does require further investigation with a more controllable test system. There are cell culture techniques that exist where cells can be placed into an arrested state and in a more controllable manner, which would remove a number of variables that have hampered this study. This would be certainly a good avenue for future research.

5.6 Other Suggested Future Work

Further statistical analysis of the data produced in this chapter is required as it may allow for further analysis of the data, which may allow more significant outcomes to be drawn, allowing the opportunity to design more specific experiments in the future. This is yet to be performed. It may be suitable to use a Kruskall-Wallis test, which is similar to the test used, but adaptable to allow for multiple groups. This may create more significant statistical analysis, especially considering the low effect rates in many of the control experiments.

There have been THz absorption studies performed on human epithelial cells and stem cells, however the results of these studies are inconclusive. There is a need for further experiments to be performed with more complex analysis, which will only be possible in the TCF. As mentioned in the previous chapter, THz radiation has been detected in the TCF and therefore a number of experiments on the Zebra fish cells and the other cells can now be performed which will allow a far more thorough study that was not possible previously.

Finally the spectral information of ALICE is vital in interpreting results. The understanding of the way changes in accelerator settings effect the spectrum could help understand past results and allow better design for future experiments.

5.7 References

[1] T. Braunbeck, M. Bottcher, H. Hollert, T. Kosmehl, E. Lammer, E. Leist, M. Rudolf and N. Seitz, *Altex-Alternativen zu Tierexperimenten.* **22**, 87 (2005).

[2] C.A.E. Turner, *Ph.D thesis*, University of Liverpool (2009).

[3] C.B. Kimmel, W.W. Ballard, S.R. Kimmel, B. Ullmann and T.F. Schilling, *Developmental Dynamics.* **203**, 253 (1995).

[4] DIN. (2003) German standard methods for the examination of water, waste water and sludge. Sub-animal testing (group T). Part 6: Determination of the effect of nonacute toxicity of waste water on the development of fish eggs. *DIN 38415-6.*

[5] OECD. (1992) Fish Acute Toxicity Test. *OECD Guidelines for Testing of Chemicals:* 203, (pp9).Organisation for Economic Co-operation and Development. Paris, France.

[6] OECD. (2006) Fish Embryo Toxicity (FET) Test. *OECD Guideline for the Testing of Chemicals: Draft version,* (pp11). Organisation for Economic Co-operation and Development. Paris, France.

[7] L. Nicolson. Verbal communication (October 2010)

[8] G.A. Geiger, S.E. Parker, A.P. Beothy, A.J. Tucker, M.C. Mullins and G.D. Kao, *Cancer Research.* **66**, 8172 (2006).

[9] R Development Core Team. (2008) R: A language and environment for statistical computing. R Foundation for Statistical Computing, Vienna, Austria.

[10] R. Shie, (2004) Statistics 2.2 The Wilcoxon signed rank sum test. "online" http://mlsc.lboro.ac.uk/resources/statistics/wsrt.pdf (12/11/10).

[11] R.C. Schirone and L. Gross, *Brachydanio rerio. Journal of Experimental Zoology.* **169**, 43 (1968).

[12] P.A. Padilla and M.B. Roth, *Proceedings of the National Academy of Sciences of the United States of America.* **98**, 7331 (2001).

[13] J. Bock, Y. Fukuyo, S. Kang, L. Phipps, B.L. Alexandrov, *PLoS ONE.* **5**, 15806 (2010).

[14] B.S. Alexandrov, V. Gelev, A.R. Bishop, A. Usheva and K. Rasmussen, K. *Physics Letters A.* **374**, 1214 (2010).

Chapter 6. Heparin

This chapter describes the comprehensive study of heparin, a model compound for heparan sulfate, which is found in the extracellular matrix (ECM).

All higher organisms are made of many cells, (the human body has an estimated 50 trillion cells). These cells are surrounded by a number of different complex materials, which are collectively named as the extra-cellular matrix (ECM). This is the region in which complex signaling events, which lie at the heart of coordinating responses required during growth, responses to disease and the natural processes of ageing are coordinated and many of these involve glycosaminoglycans (GAG) and Heparan Sulfate (HS) polysaccharides, in particular. HS is an important member of a family of linear anionic polysaccharides, the GAG's. They are covalently attached to proteins to form proteoglycans, which occur on the surfaces of almost all mammalian cells and in the ECM between cells. HS is the dominant molecule of the cell surface and has chain lengths of ~50 – 100 nm, and a concentration of greater than 10^6 HS chains per cell [1]. One important challenge is to understand the conformational and sequence characteristics of this class of molecule, which ultimately determine its roles in biological processes.

6.1 Heparan Sulfate and Heparin

HS regulates many aspects of cellular development, biochemistry and physiology due to its ability to interact with a vast array of regulatory proteins [2]. In a recent study, 435 proteins were identified as interacting with HS [3]. While HS has emerged as a key GAG polysaccharide, the study of the relationship between its sequence, physical properties and consequent biological activities has not been simple to address. Such understanding of the properties of these molecules is a prerequisite to developing the necessary capabilities to treat the panopoly of conditions and diseases to which HS is relevant, which include neurodegenerative disorders, wound healing, cancer and ageing processes, to name but a few. The potential sequence diversity of HS has led some authors to propose it as a reservoir of enormous information content [2-4]. Others have suggested that a high level of redundancy exists between substitution pattern and conformational and charge properties [5], demonstrating that it is possible to reproduce biologically active conformations using both modified GAGs and non-GAG polysaccharide analogues of HS. These were also able to induce similar structural changes and stabilisation in proteins [6], as well as provide their biological activities [7]

suggesting that it will be possible to mimic some of the activities of HS using these analogues.

Despite its ubiquity, HS is relatively difficult to isolate in the quantities required for many physical investigations of its properties. Consequently, many studies have employed its close structural analogue, heparin. HS and heparin share a common underlying structure, based on alternating disaccharide repeating units comprising a 1,4 linked uronic acid (either D-glucuronate or L-iduronate) and glucosamine residues containing a range of N-and O-sulfate substitutions. An important feature common to both is the ability to bind cations, on account of both the carboxylic acid groups of the uronate residues and the N- and O-sulfates. A key difference between HS and heparin is the existence of a higher-order domain structure in HS, which heparin, the more highly charged of the two, lacks. It has proven possible to extract many general characteristics of HS by using heparin and its systematically modified derivatives as a model compound [8].

Heparin is composed of polydisperse chains with molecular weights between ~10 and 20 kDa corresponding to ~ 20-40 disaccharides. A disaccharide unit is ~1 nm in length and heparin forms extended, semi-flexible chains with high solubility in aqueous medium, greater than 100 mg/ml. It has recently been shown that the interaction of heparan sulfate chains with cations can result in greatly altered conformational properties and biological activities [9-11]. Furthermore, the binding of particular cations altered motional properties inferred through NMR (Nuclear Magnetic Resonance) T_2 relaxation times [12,13]. The treatment of interactions of heparin and cations, according to a number of theories [14] has largely been derived by analogy from studies of the more homogeneous polyelectrolyte DNA. However, heparin does not behave as a simple polyelectrolyte, because it has the capacity to bind cations with some selectivity [15-18].

Given their extended, semi-rigid and charged nature, heparin polysaccharide chains might be expected to adopt self-ordered structures [19]. This has not, as far as I am aware, been explored in detail. There are countless instances of biological macromolecules forming liquid crystalline phases or adopting some degree of preferential ordering in solution or in solids [20-22]. The possibility that the polysaccharide chains of heparin and so heparan sulfate are subject to a form of self-

ordering would offer the interesting possibility of introducing localised directionality to the cell surface environment. This might serve a number of roles, one of which would be to restrict the distribution of proteins along particular routes as they alternately bind and dissociate. The thermodynamic consequences of this kind of movement restriction, now not only constrained in the plane of the cell surface, but also in particular directions within that plane, could also drastically alter binding, mobility and thermodynamics.

In this chapter, experiments will be discussed that were designed to determine whether these molecules have any inherent propensity to form self-ordered structures and to investigate the effects of changing cation identity. The approach relies on applying several complementary spectroscopic techniques allied to polarised optical microscopy. If these molecules undertake some form of ordering, then anisotropic spectral characteristics would be expected; several of these techniques are sensitive to features arising from processes over widely varying energies and distances. These complementary spectroscopic techniques comprise UV-Vis spectrometry and Reflection Anisotropy Spectroscopy (RAS), polarised light microscopy (PLM) and linearly polarised terahertz (THz) radiation; FTIR at the SRS at Daresbury Laboratories and ANKA in Karlsruhe Germany. THz spectroscopy was employed to explore the characteristics of spectral features in the THz range 1-16 THz, whose fundamental modes are in the regime of naturally occurring thermal conformational changes in macromolecules.

6.2 History of Heparins

HS is involved in a number of critical biological processes, which include cell growth and division, embryogenisis, development and homeostasis. These biological processes are made possible by the way in which heparans interact with various proteins, which is dependant on their structure. They are therefore vitally important in all research into developmental biology, cancer, wound healing, infectious diseases, inflammatory processes and neurite outgrowth [9,23].

Heparin has been studied continually, since its discovery in 1916, using a number of biological, chemical and physical techniques [24]. Heparin has revealed a high number of biological activities that include anticoagulants, antithrombic agents, as well as antilipemic and antimetastic activity, and generally heparin shows activities where HS

is active. Since 1935 heparin has been used clinically as an anticoagulant and insulin is the only more commonly used natural therapeutic agent. These diverse biological activities are due to heparin's ability to bind proteins, and one of the most thoroughly characterized of these interactions is with antithrombin [12].

In the last 30-40 years a vast literature concerning heparin and HS has been produced with many key ideas that have increased the understanding with dedicated efforts from biochemists, glycobiologists, cell and structural biologists. The realisation of the complexity of their structure has emerged but, despite best efforts, elucidating the detailed structure remains one of the most challenging aspects of heparin research. Not only is the initial structure an issue, once this is understood, research into understanding the dynamic manipulations and tweaking of the structure, which plays a vital role in a number of key interactions, can begin [3, 9].

Within the last 20 years, research into the interaction between heparin and cations has increased with a number of new methods being applied to provide greater scientific understanding. There is strong evidence that the chemical structure of heparins plays an important part in their biological activities, by affecting their interactions with proteins. These interactions are dependent on the substitution pattern of the O-, N-sulfates, N-acetyl groups and the uronic acid content, but the relationship between substitution pattern and conformation is not fully understood. It is very difficult to monitor the relationship between conformation, substitution pattern and activity experimentally as subtle changes could produce substantial effects on activity. At present, relatively little is known about what these changes do to the conformation of the molecule [9].

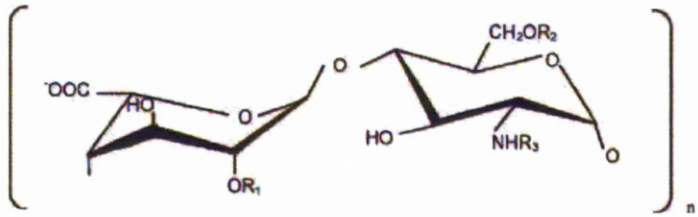

Figure 6.1. The generalised repeating unit of heparin and its derivatives [9].

There are a number of techniques that have been used to characterise heparin, these include paper chromatography, gel filtration, X-ray crystallography, NMR, iosthermal titration calorimetry, computational docking, enzyme-linked immunosrobant assay (ELISA), X-ray Photoelectron Spectroscopy (XPS), optical rotary dispersion (ORD), Photoelectron spectroscopy (PES), quartz crystal microbalance dissipation (QCM-D), synchrotron radiation circular dichroism (SRCD), electron paramagnetic resonance spectroscopy (EPR), FTIR and polarimetry [9,18,25–29]. However there has been limited work performed in an attempt to understand the conformation and orientation of the molecule. RAS will provide information on the anisotropy of the heparins in a dried film, The THz spectra could also potentially provide information on the long range ordering of the heparin cation films and any differences between them. There are other techniques that can provide this information such as Fluorescence Resonance Energy Transfer (FRET) however this, like other techniques, requires labeling of the molecule, which has the potential to create changes in the structure.

6.3 Heparin Cation Derivative Studies

HS has considerable biological importance and great effort has been depleted attempting to advance the understanding of its biological function and link that to its structure and conformation. This has included monitoring a number of model compounds which are modified heparin derivatives including the Na^{+}, Ca^{2+}, Mg^{2+}, Zn^{2+}, NH_4^{+}, Cu^{2+}, Fe^{3+}, Mg^{2+} and K^{+} cation forms. Heparin is a highly polyanionic molecule, one of the most negatively charged biological molecules known. This not only allows their interaction with counterions, but makes the interaction necessary [9,18]. These interactions change the structure and conformation of heparin affecting the activity. This can affect the way they react in processes; in some functions the heparin molecules bind to and release the metal cations when required. There has also been considerable debate as to whether these cations bind at specific localized sites along the linear chain, or in a delocalized, non-specific fashion [29].

Linking the substitution patterns of heparin derivatives, with their conformation and activity has been very difficult experimentally. These substitution patterns can sometimes be rather subtle, however, can have great effects on the activity and conformation. This has therefore in the past been overlooked by many scientists when

looking at the biological activity of the heparins due to the difficulty of monitoring them even when used in the more well-known, well-defined, biological processes [9].

One technique that has been used to probe structural changes in the presence of various cations in the past is NMR, with qualified success. Circular Dichroism (CD) and in more recent years synchrotron radiation CD (SRCD) has been used to look at the conformational changes of GAGs including heparin. This has brought to light that the conformational differences of different heparins can be considered to have a major effect on chain flexibility although further work is required to understand the different derivatives [9]. The possibility of linking CD and SRCD with techniques such as PLM and RAS could increase the understanding of the conformation and molecular organisation of heparin derivatives. It is also thought that THz radiation could play a crucial role in understanding the long-range effects of the heparin compounds, due to its ability to probe long-range modes at energies equivalent to those available at room temperature.

SRCD has proven useful in heparin research due to its high sensitivity to uronic acid conformation. The reason for this sensitivity is due to the technique being able to monitor the chiral environment of the carbonyl groups of the uronic acids, which is not detectable by other techniques. Results proved that all the heparin derivatives tested provided different spectra, which would imply they are all structurally different. However, this is still not fully understood and further work is needed before conclusions can be made on the structural reasons for their different spectra, as it is still not possible to define the structure and conformation, and their different reactions with proteins [9].

In 1976 Chung and Ellerton [30] showed that the interaction between Cu^{2+} heparin and other uni- and bi-valent metal cations heparin forms are specifically different, suggesting that chelation (the binding of, or complexation of, bi/or multidentate ligands) may occur, and felt the carboxylate group played a vital part in this interaction. Grant *et al.* studied this work closely before performing their own experiments with polarimetry. The conclusions they drew supported the idea of a further complexity of the Cu^{2+} heparin, they suggested that there may be a number of complexes, with one not binding as would be expected from previous work [29].

It is known that the reaction between heparin and Cu^{2+} reduces the optical rotation,

however it has not been possible to establish the reason why. It has been suggested that this decrease in optical rotation could be due to the copper chromophore, or a particular change in conformation or hydration within the heparin chain. However, it has been confirmed experimentally that there are rotation changes when varying the cations with heparin, with the maximum changes being directly linked with the association constants for the interactions between a number of cations that include Cu^{2+} [29]. These rotational experiments are considered to be an opportunity to monitor the heparin cation derivatives as they are simple, none destructive methods that can be performed quickly.

Cu^{2+} ions show paramagnetic activity, due to them having an unpaired electron in the d^9 outer shell. This allows further experiments to be performed that cannot easily be done on other heparin derivatives. NMR can detect the location of the coordination of the Cu^{2+} ions by the line broadening of the atoms near to it, and EPR to detect the changes in the environment of the Cu^{2+} ion itself. However, owing to the effects of paramagnatism, it rules out NMR as a comparison tool to other molecules as the Cu^{2+} ions affect the coupling constants and relaxation times. However, when linked with FTIR it does have the potential to add further conformational change information. Thus, the nature of the binding and the structure of specific sites where initial actions take place could be identified [18].

FTIR has been used to look at Cu^{2+} heparin by monitoring the changes in C=O and N-H stretches. EPR was also used to monitor the initial binding phase of the heparin resulting in the understanding that the initial binding phase is completed once 15-20 Cu^{2+} ions are bound to each chain, however, after this phase the binding reverts to being non-specific. It is understood that the C=O is vital in the bonding with the Cu^{2+} ions however precise understanding of the full affect on structure of the interactions is still unknown. Work by Rudd *et al.* detailed the specific disaccharide that binds to the Cu^{2+} ions and that it forms a distorted 4 fold geometry [18].

Heparin studies have to be performed very carefully, as changes in temperature, presence of divalent cations, variations in pH and variations in ionic strength can all lead to conformational and structural changes that can invalidate results. For example, work has been done to confirm that changes in pH, temperature and the presence of divalent cations can all influence the position of chemical shifts in NMR experiments [25].

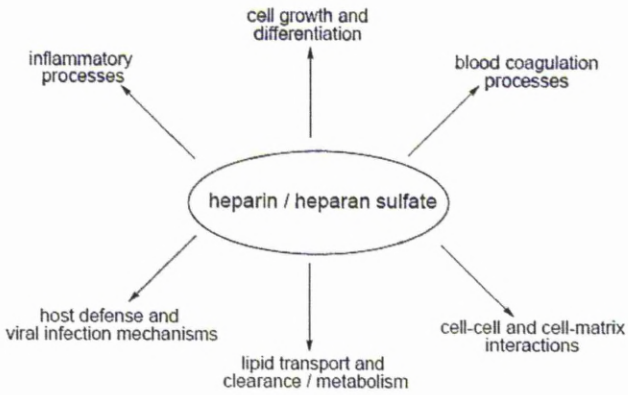

Figure 6.2. The Involvement of heparin and HS in physiological processes [10].

6.4 Experimental Methodology

This section explains the experimental methodology of the various experiments used in this study. More thorough descriptions of the two main techniques, FTIR and RAS can be found in the experimental section, chapter 2.

6.4.1 Heparin Sample Preparation

Porcine mucosal heparin obtained from Celsus Laboratories, Cincinnati, USA, was dissolved at a concentration of 100 mg/ml in HPLC grade water. The heparin was supplied predominantly in the Na^+ form. The cation associated with the heparin was exchanged to saturation by treating a solution of heparin (100 mg/ml) with excess of cation exchange resin (Dowex W-50) in the required form, which had been prepared previously by treating the resin (H^+ form) with excess aqueous solution of the respective chloride salt (0.5 M; Na^+, K^+, Ca^{2+}, Mg^{2+}, Cu^{2+} and Zn^{2+}). UV-visible and FTIR experiments were performed on liquid specimens (~ 5 mg/ml solution) while solid-state specimens for PLM and RAS were formed by air-drying for 36 hours at room temperature 100 µl of the heparin solution (100 mg/ml) on a clean glass microscope slide. The dried slide consisted of an approximately circular disc of ~ 0.1-0.08 mm. For the THz experiments, the dried films were carefully removed from the slide and mounted in card holders and the experiments were performed in transmission.

6.4.2 UV-Visible Experiments

The heparin solutions were prepared as described above and then diluted to low concentrations (5 mg/ml) and recorded in quartz curvettes on a GENESYS 10-S UV spectrophotometer and recorded in absorbance mode between 190-1100 nm with reference to a water blank. The heparin derivatives tested where, Na^{+}, K^{+}, Ca^{2+}, Mg^{2+}, Cu^{2+} and Zn^{2+}.

6.4.3 Polarising Light Microscopy (PLM)

The PLM measurements were performed on 100 mg/ml heparin cation forms in both solid, dried film, and liquid forms on glass slides. The experiments were performed on an Olympus BX51 Series Optical Microscope.

6.4.4 RAS methodology

ADRAS measurements were made at 15° intervals from 0° to 90° on the Na^{+}, Mg^{2+}, Ca^{2+} and Cu^{2+} specimens. For the Zn^{2+} specimens ADRAS measurements were made at 0°, 45° and 90° in order to obtain an indication of the size of the optical anisotropy. The RAS technique is discussed in chapter 2.

6.4.5 THz FTIR Experiments

The initial THz measurements were performed using an FTIR instrument on the synchrotron radiation source (SRS) at the Daresbury Laboratory on beam line 13.3. A background signal was taken with a sample holder in place but no sample. The sample area was purged with N_2 gas for 15 minutes prior to any data being taken in order to remove any moisture. The FTIR data was taken in transmission between 1-20 THz (~ 30-600cm^{-1}) on six different heparin cation forms, Na^{+}, Mg^{2+}, K^{+}, Cu^{2+}, Zn^{2+} and Ca^{2+}. Subsequent experiments investigating the temperature dependence of the THz response of the heparin films were performed with a Bruker IFS66vs spectrometer on beam line IR2 at ANKA using a custom built cryostat. The temperature was monitored with a thermocouple. The ANKA experiments made use of radially polarised edge radiation from the synchrotron. Edge radiation has far less vertical divergence than conventional synchrotron radiation and provides an increased intensity at low THz. Further angular experiments were performed on the heparin forms using a polariser. The FTIR technique is discussed further in chapter 2.

6.5 Experimental Results

The aim of this research is to obtain some insight into the properties of heparin derivatives. It is known that cations interact with heparin and modify its physical properties and biological activity. Since heparan sulfate and heparin cannot be studied in physiological conditions, experiments were performed on thin film specimens of heparin complexes with different cations in order to investigate the effect of cations on the structure and dynamic properties of heparin and, by analogy, of heparan sulfate. An important issue is to establish whether the cations influence the directional properties of heparin since this could offer clues as to the function of heparan sulfate in the extra cellular matrix and in particular if it has a role in the directional characteristics of biological processes. The range of cations chosen includes the four common cations, Na^+, K^+, Ca^{2+} and Mg^{2+}, which are prevalent in biology but, also two transition metal ions, Cu^{2+} and Zn^{2+} which, while existing in low concentrations, nevertheless play crucial roles in many biological processes. For instance, Cu^{2+} ions have been implicated in angiogenesis; the creation of new blood vessels associated with tumour growth, as well as with GAGs, including HS, in the early stages of amyloid fibril formation, which is a key molecular process at the heart of several neurodegenerative and age-related disorders [31]. A key question relates to the behaviour of these materials in bulk and whether they adopt any ordered arrangements. Although largely unexplored, such a property could have a significant impact on the behaviour of HS at the cell surface and influence the thermodynamics of interactions with proteins, hence the complex cell-signalling events upon which growth, development and disease depend.

The comparison of the UV-Visible spectra in the range of 1030-190 nm (~ 1.2-6.5 eV) of the materials in solution (figure 6.3) gives information on the electronic structure and optical modes in the heparin solution. Fig 6.3 shows that the Na^+, Mg^{2+} and Ca^{2+} forms have very similar spectra, the spectrum of the Cu^{2+} form is broader and that of the Zn^{2+} form narrower than those of the simple metals (Na^+, Mg^{2+} and Ca^{2+}). The spectra peak at ~ 225 nm and those of the Na^+, K^+, Ca^{2+} and Mg^{2+} forms have very similar profiles. The Cu^{2+} and Zn^{2+} forms differ from the simple metal systems and from each other: the Cu^{2+} system showing a broader and the Zn^{2+} system a narrower spectral

profile. In addition the Cu^{2+} system differs from the others in showing the presence of a weak feature at ~ 650-1050 nm, which is shown in figure 6.4.

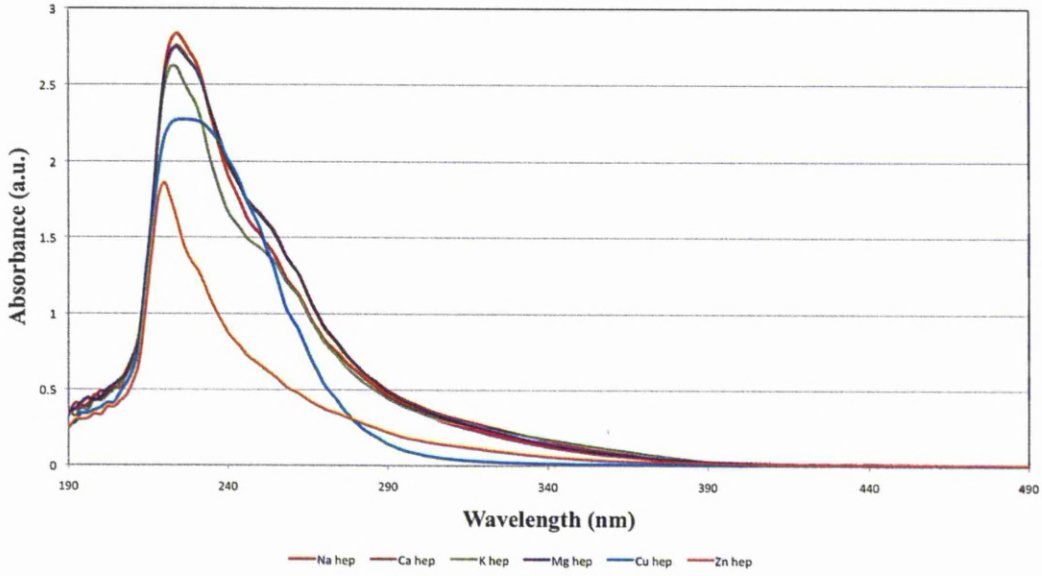

Figure 6.3. The UV Vis spectra of heparin cation solutions between 490-190 nm (~2.5-6.5 eV).

These differences probably arise from the influence on the optical transitions of the 3d levels of Cu^{2+} and Zn^{2+}. The less tightly bound 3d electronic arrangement of Cu^{2+} broadens the optical response, while the more tightly bound 3d electrons of Zn^{2+} narrow the energy spread of valence electrons and of the optical spectrum through more efficient screening of the atomic core.

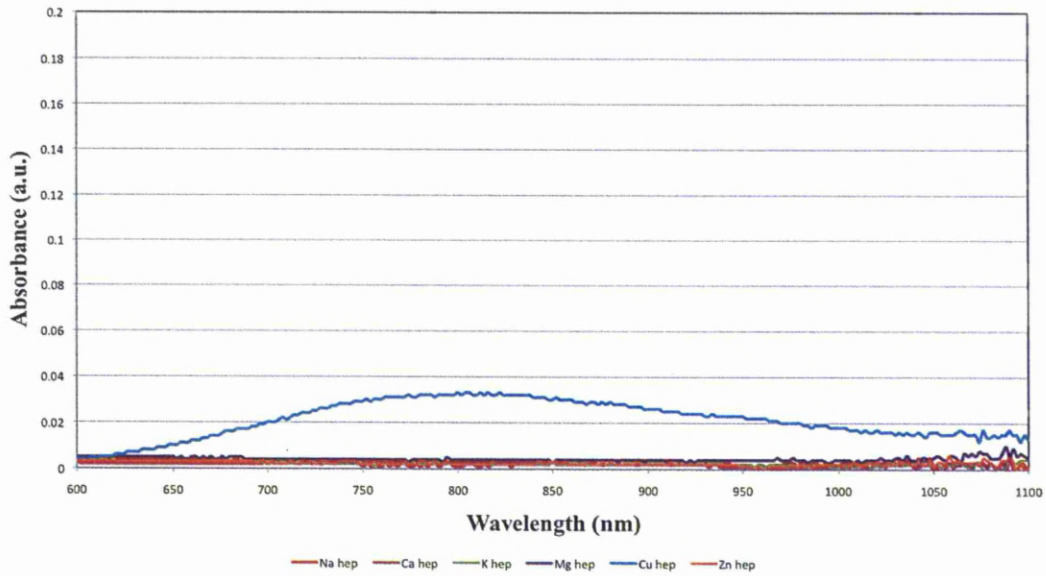

Figure 6.4. The UV Vis spectra of the heparin cation solutions showing the weak Cu peak between 1100-600 nm (~1.1-2.1 eV). Note the change of scale from figure 6.3.

Heparin polysaccharide is a linear polyanionic material, which, in solution, is thought to adopt extended, semi-flexible chains. It is conceivable that some general preferential orientation of the linear polymers occurs in the freezing of the solution to form the thin film specimens. This view is supported by the PLM and RAS results. The PLM data suggests strong anisotropic signals in some of the solid cation forms, the Na^{+}, Ca^{2+} and Mg^{2+} dried film specimens with signal intensity decreasing in the order Ca^{2+}, Na^{+}, Mg^{2+}. The Cu^{2+} and Zn^{2+} specimens showed no anisotropy in PLM images. When the PLM was performed on the liquid films there was no anisotropy seen in any of the cation forms. The RAS data indicates that there is some anisotropy in the ordering of the cation centres in the bulk of the material (solid film) since truly amorphous material gives a zero RAS signal unless there are ordered structures on the surface. However, X-ray diffraction studies establish that none of the solid specimens were crystalline though this lack of crystalline order does not mean that the films do not have local order and local anisotropy.

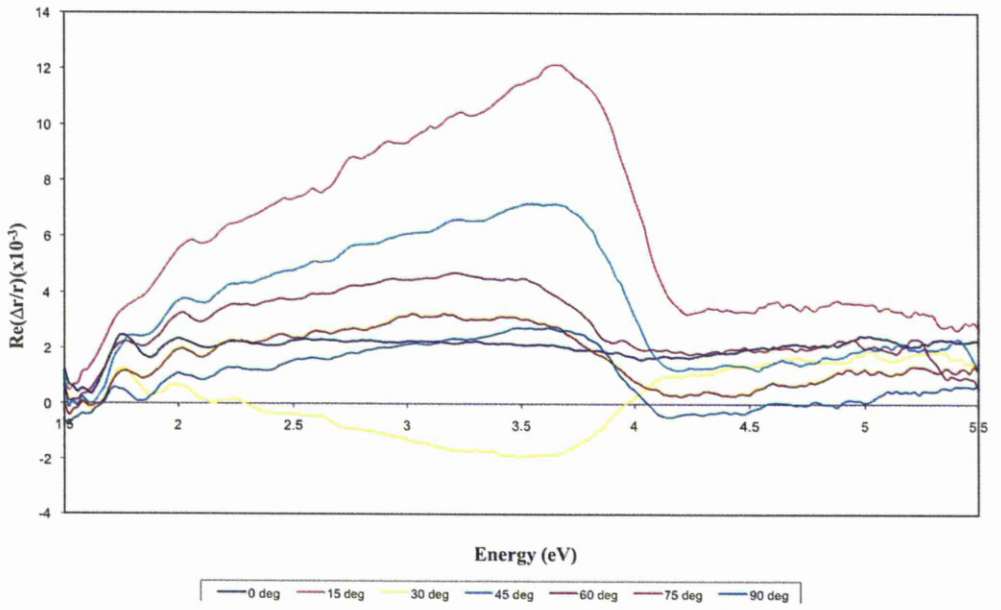

Figure 6.5. RA spectra of the Na^+ heparin film on a glass slide with angular variation.

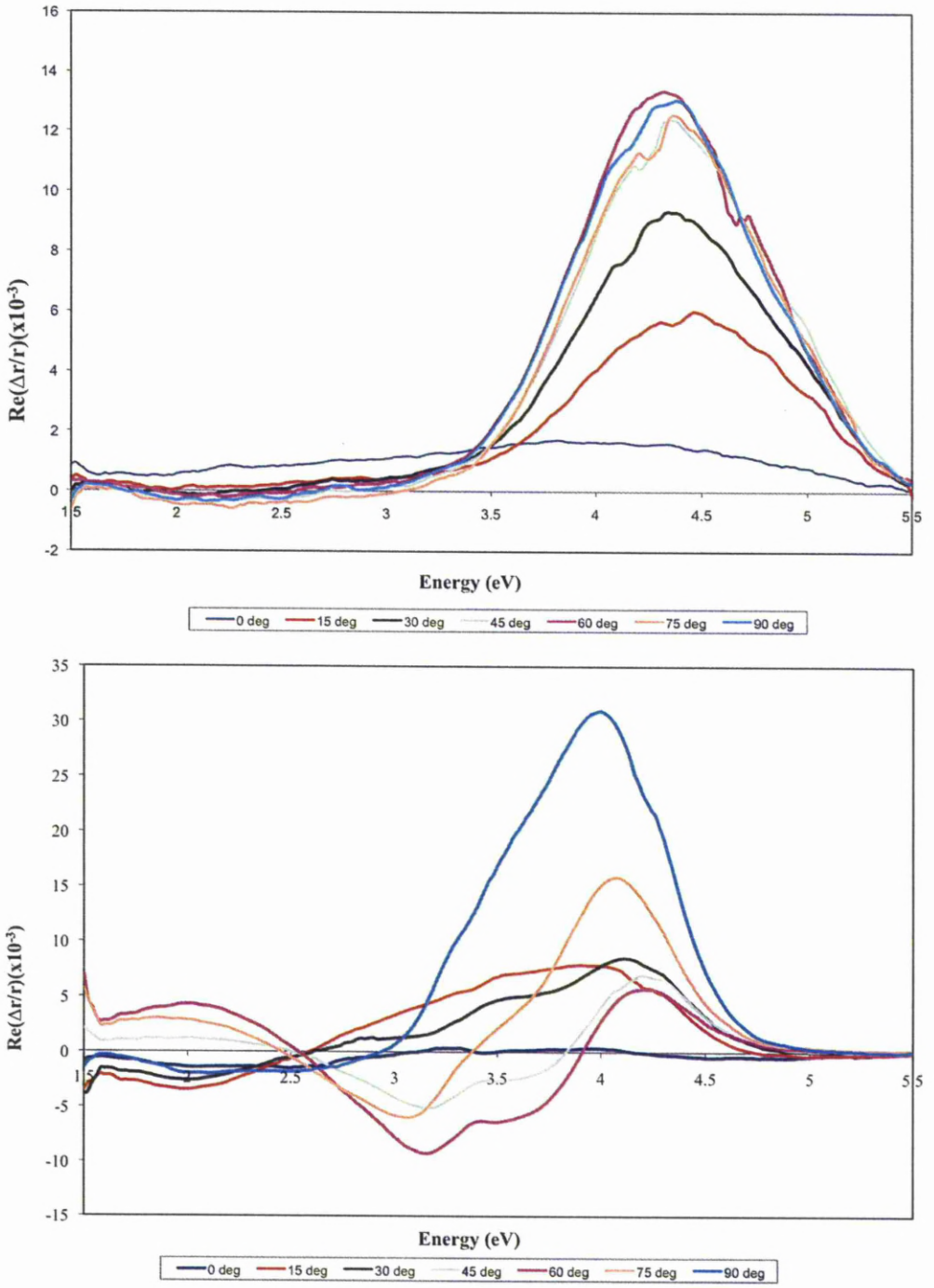

Figure 6.6. The above spectra are for the Mg^{2+} and Ca^{2+} heparin films on glass slides from top to bottom respectively.

There are significant differences in the maximum optical anisotropy observed at the peak of the optical response from the different forms. For the Na^{+}, Mg^{2+} and Ca^{2+} forms the maximum anisotropy reached values of 12 x 10^{-3}, 13 x 10^{-3} and 30 x 10^{-3} RAS units respectively. The spectra are presented in figure 6.5 and 6.6. These values are significantly larger than those observed from the RAS of molecules adsorbed on metal and semiconductor surfaces [32-36] and suggest that the signals are arising from the bulk of the material. The corresponding results for the maximum anisotropy of the Cu^{2+} and Zn^{2+} forms did not exceed 1.8 x 10^{-3} and are did not increase substantially when measured at other angles. These are shown in figure 6.7 and 6.8.

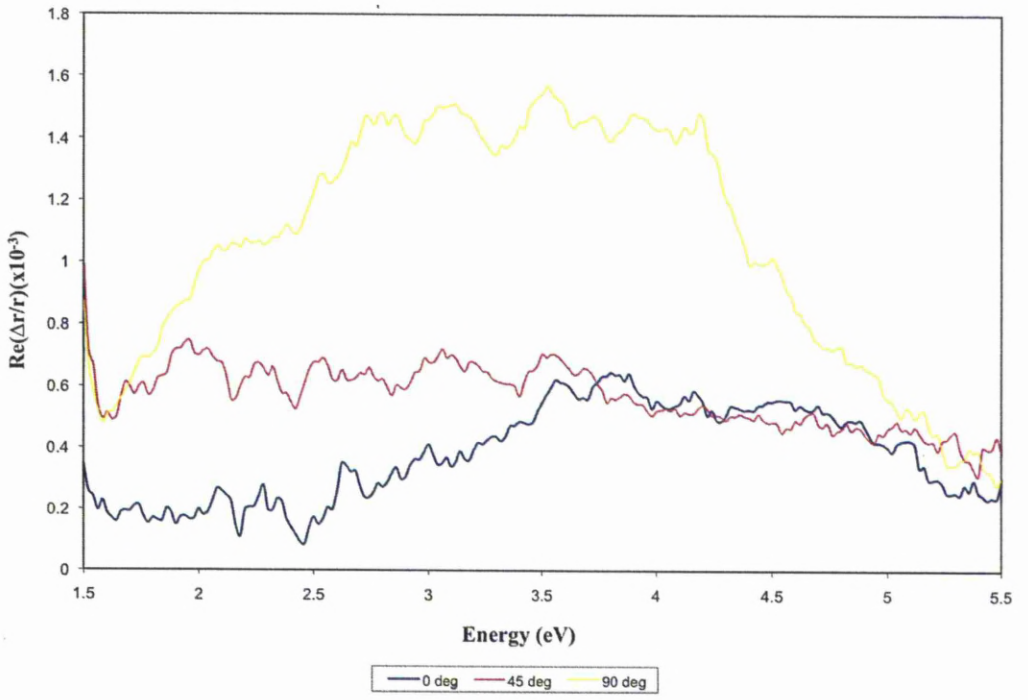

Figure 6.7. The RA spectra of the Cu^{2+} heparin film on a glass slide.

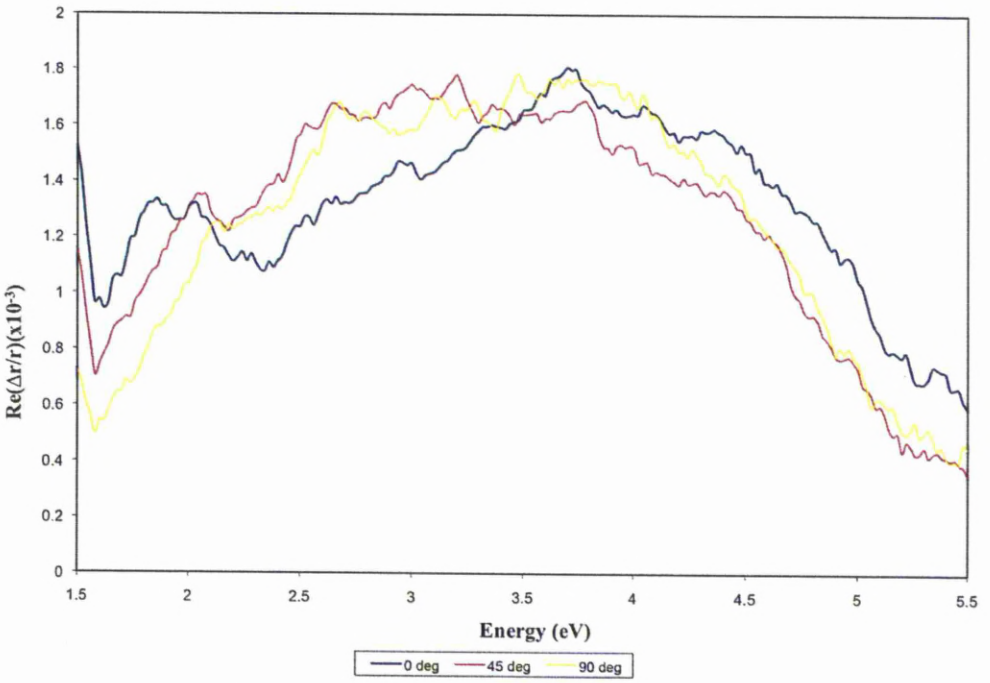

Figure 6.8. The RA spectra Zn^{2+} heparin forms on a glass slide.

The RAS results for these films, Na^{+}, Ca^{2+} and Mg^{2+} (in figures 6.5 and 6.6) suggest, that the optical response of the structural units associated with each of the cations, is anisotropic and that these structural units are not orientated randomly but are ordered on a macroscopic scale in the films. The observation that there are angles for all three forms at which the optical anisotropy across the whole spectral range is very small, (Na^{+} peak amplitude is 12, with an amplitude of 2 on the flat spectra, Ca^{2+} max at 30 RAS units, min close to 0, 90 degree difference, Mg^{2+}, peak signal is 13, flat line max 1.7), indicates that if, as expected, the optical response arises from several transitions with dipoles orientated in different directions with respect to the local structure then these dipoles adopt a roughly planar orientation, with the planes at right angles to the surface of the films. These results are consistent with the films consisting of a disordered arrangement of roughly linear polymers with the cation centres distributed along the length of the polymer and with the cation centres adopting essentially the same orientation in the films.

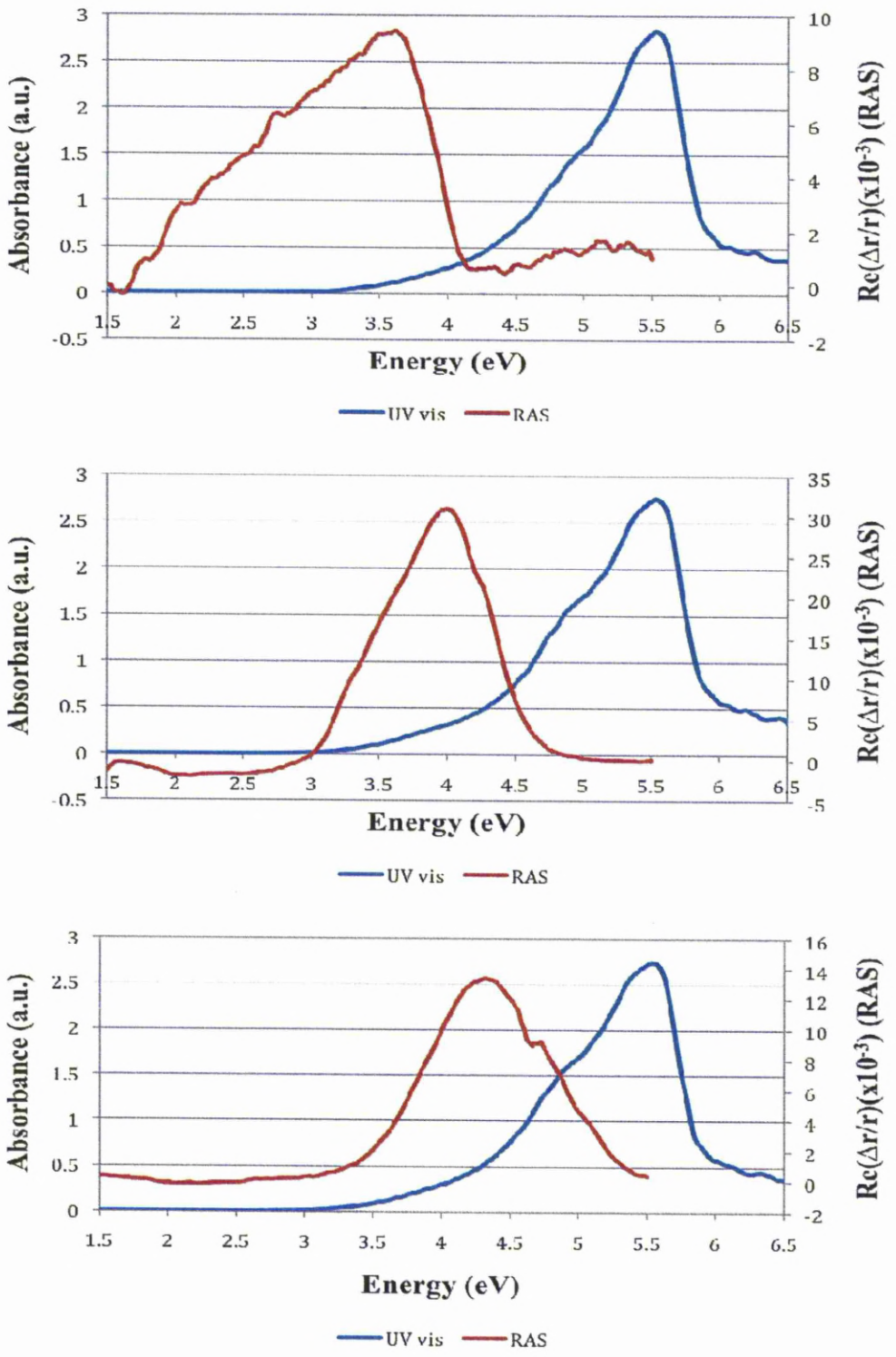

Figure 6.9. A comparison between UV Vis data in blue and RAS data in red for the Na^{+}, Ca^{2+} and Mg^{2+} heparin films from top to bottom respectively.

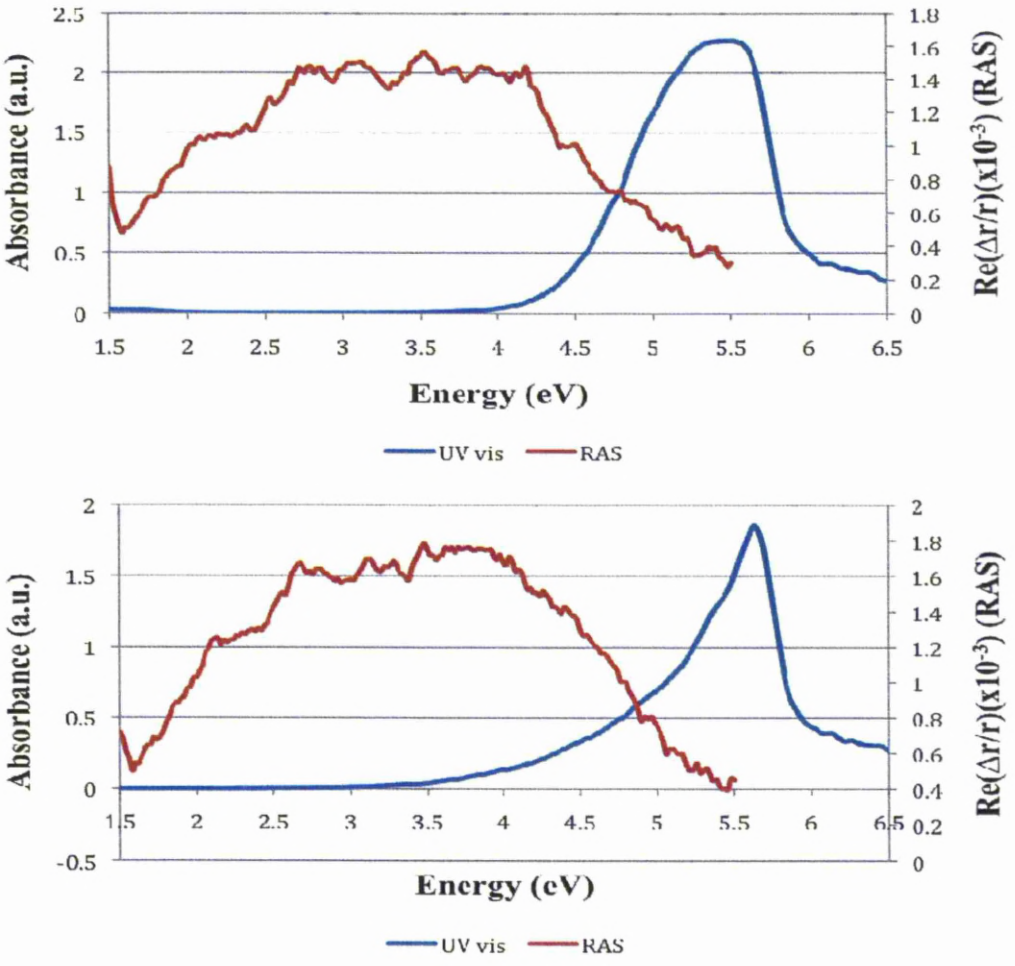

Figure 6.10. A comparison between UV Vis data in blue and RAS data in red for the Cu^{2+} and Zn^{2+} heparin films from top to bottom respectively.

It is more difficult to deduce useful information about the nature of the films formed from the Cu^{2+} and Zn^{2+} forms from the RAS results. There is a more significant broadening of the RAS signal in these forms on going from the solution to the film than was found for the simple metals as shown in figure 6.9. This could be a solid state effect arising from the overlap of the 3d derived molecular orbital structure of different cation centres though this would imply a greater concentration or a stronger clustering of cation sites in the Cu^{2+} and Zn^{2+} forms (shown in figure 6.10), than in those of the simple metals. Alternatively it could arise from a greater anisotropy in the spectra with the RA

signal of each cation centre coupled with more macroscopic disorder in the orientations of the cation centres than found for the simple metal forms. A comparison of the RAS results with the optical (UV vis) absorption spectra of each of the specimens in solution (figures 6.9 and 6.10) shows that the formation of the films has a significant effect on the optical properties of the material and that this varies with the ionic composition. For all the materials the optical response is shifted to lower energies and is broader in the films than in solution. These changes are expected on the formation of a solid. However there are significant differences between the different forms. The shift to lower energy of the high energy cut off of the optical response is 1.9 eV, 1.2 eV, 1.6 eV, 1.3 eV and 1.0 eV for the Na^{+}, Mg^{2+}, Ca^{2+}, Cu^{2+} and Zn^{2+} forms respectively. The change in the width of the optical response also varies with composition with the full widths half maxima (FWHM) increasing from 0.8 eV to 1.2 eV, 0.8 eV to 1.1 eV, 0.8 eV to 0.9 eV, 0.9 eV to ~ 2.5 eV and 0.6 eV to ~ 2 eV for the Na^{+}, Mg^{2+}, Ca^{2+}, Cu^{2+} and Zn^{2+} forms respectively.

The Cu^{2+} and Zn^{2+} forms show little anisotropy in their RAS signals and an orientation has been captured for which the anisotropy across the whole spectral range is very small for the Cu^{2+} form though not for the Zn^{2+} form. All that can be said is that if these specimens have the same degree of macroscopic order as those formed from the simple metals then the anisotropy in the intensity of the local optical signal is small though the anisotropy in the width of the optical response may be greater. This might reflect the tighter binding of the Cu^{2+} ion to the heparin structure [18] itself lacking strong molecular alignment, which prevents alignment of the dipoles. Alternatively, significant local anisotropy may be cancelled in these specimens by a much reduced macroscopic order from those of the simple metals. In the absence of information on the origins of the optical response, such as the number and energy of transitions and their directions with respect to the physical structure of the optically active elements, it is not possible to interpret the results of the angular variation of the optical anisotropy in detail. In the event that information on the optical structure of components of the material becomes available, perhaps from theoretical work, then more detailed ADRAS studies could be more fruitful.

It is known that cations interact with the heparin polysaccharide through carboxylic acid groups, and N- and O-sulfates, and this is known to alter both the

flexibility and conformation of the material. The results presented above suggest that films formed from complexes with the simple metal ions lead to essentially linear systems with the polyanionic chains in roughly parallel orientations and with little variation in the local orientation of the cation complexes. However, films formed from complexes with Cu^{2+} and Zn^{2+} may have a more disordered structure that could arise from greater deviations from linearity of the polyanionic chains.

6.5 THz Exposure Results

6.5.1 Heparin Cation Derivatives

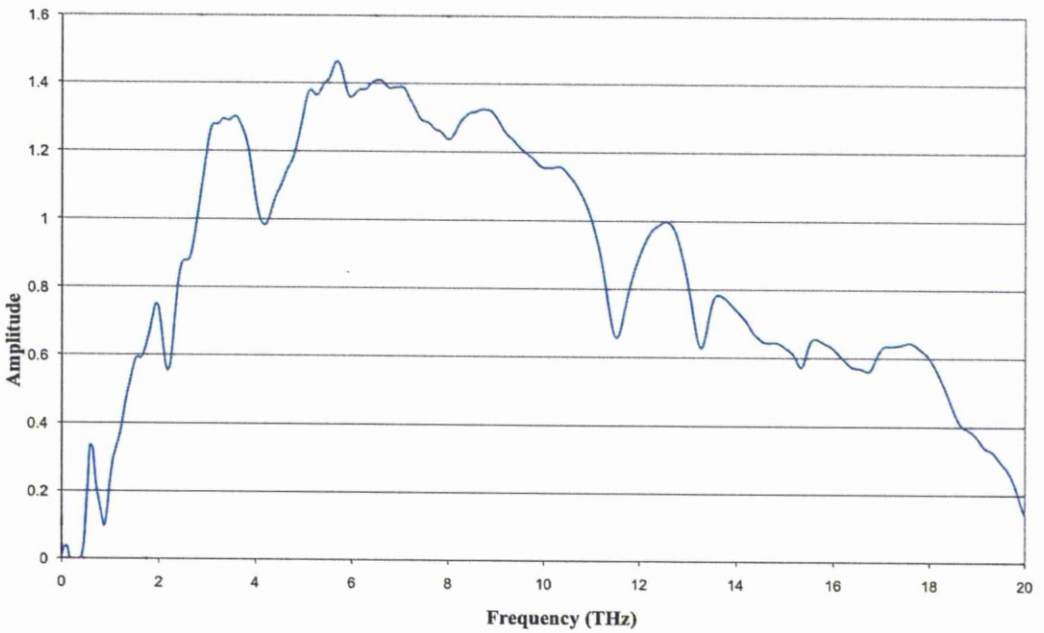

Figure 6.11. The spectra above shows the ANKA instrument response, this is the spectral region of the ANKA beam line.

The region of 0.1 to 9 THz (2-300 cm^{-1}) has been described as showing spectral features that are due to poorly localised low frequency molecular internal vibration of the weakest bonds or non bonded interactions, *e.g.* Van-der-Waals forces, dispersion forces and H-bonding [37]. So phonon modes could be an important feature of the heparin structure. The region that the ANKA accelerator can examine is shown in figure 6.11, this is the spectral output with a polariser inserted to allow angular rotation, with the

maximum polariser angle chosen, as the ANKA synchrotron does have a slight preferential polarisation. The region between 1-15 THz is chosen as it is the most stable region of the THz spectrum in the non-coherent set up. The region between 5-10 THz (230-330 cm^{-1}) seems to be the region where the most difference in cation forms of heparin is seen. All the cation forms show a similar shape of an increasing absorption with frequency on which is imposed a broad dip in intensity between 8 and 10 THz. This is shown in figure 6.12.

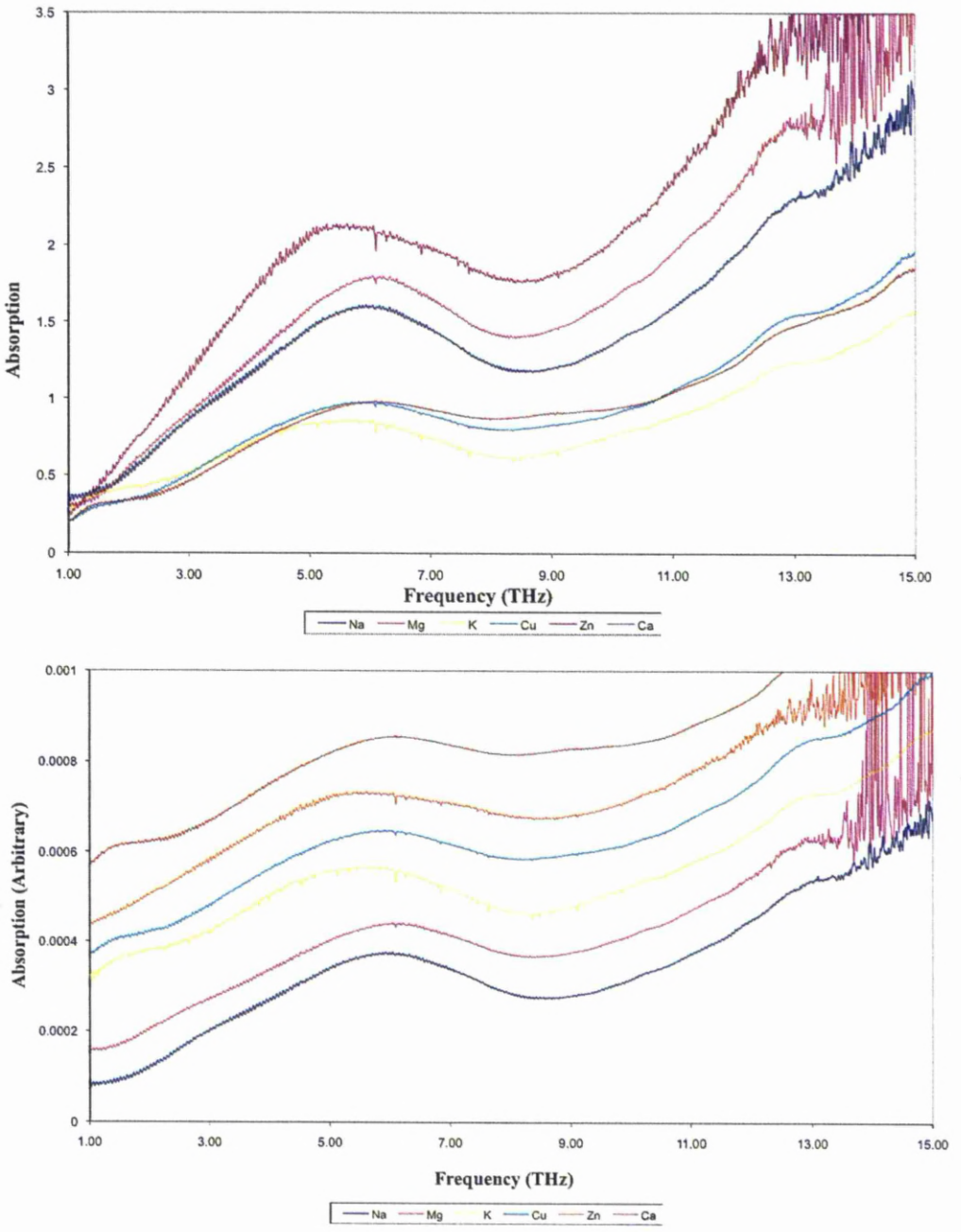

Figure 6.12. THz Spectra of heparin derivatives performed at the ANKA synchrotron. The second spectra shows the same cation forms separately, they have been normalised to show the peak shape, and offset.

The THz spectra of the specimens will arise from a convolution of the density of states of the occupied modes of vibration in the materials with the density of unoccupied modes mediated by the instrument function. Solid specimens formed from concentrated molecular assemblies such as these are expected to have a continuous distribution of low energy, long wavelength, modes of vibration arising from poorly localised low frequency molecular internal vibration of the weakest bonds, or non bonded interactions, which at room temperature will be occupied up to ~ 6 THz. The density of such modes is expected to increase rapidly with frequency at low frequency and then increase more slowly at higher frequencies as shown for proteins [38] where a distribution roughly following the square root of the frequency is observed. The spectra of figure 6.12 are consistent with such a distribution of modes apart from the pronounced broad dip in the spectra between ~ 7 THz and 10 THz. While all the specimens show a similar THz spectrum there are significant differences in detail in the positions of the first peak and the centre of the broad dip in the spectra. The difference in intensity between the peak and the dip is also slightly lower for the Cu^{2+}, Zn^{2+} and Ca^{2+} forms than for the Na^{+}, K^{+} and Mg^{2+} forms. These differences in profile establish that the ionic composition of the heparins has an influence on the long wavelength low energy modes of vibration. Evidence from NMR T_2 relaxation times [13] demonstrate that divalent cations are known to bind heparin and increase the stiffness of the chain. The THz data for heparin in the solid state also follow this trend. The absorption maxima for the divalent cations; Ca^{2+} and Mg^{2+} indicate higher energy transitions than those of the monovalent cation forms of Na^{2+} and K^{2+}. In simple terms, this can be rationalised as the divalent cations binding two points in the heparin structure, increasing the energy of molecular deformations. Interestingly, the cations do not show identical absorbance profiles, in keeping with the findings of subtle differences in their binding modes [13,39]. It is known that certain cations, for example Cu^{2+} exhibits an unusually specific structural specificity for binding [18]. We have no clear explanation for the broad dip in the THz spectra but it may arise from the frequency gap between the long wavelength low energy acoustic modes and the shorter wavelength optical modes [40,41]. The combination of positive ions and negative sugars in the heparins is expected to give rise to strong optical modes. Alternatively the dip could arise from Umklapp processes in the essentially one

dimensional heparins [42] or from a Lyddane-Sachs-Teller (LST) relation which produces a forbidden gap in the dielectric response caused by the contrary motions of ions [42].

The results for the position of the low energy peak in absorption and the centre of the broad dip in intensity are summarised for the different cation forms in table 6.1. The data does show some allowance for possible errors. These errors arise from the spectral resolution of the spectrometer, which is less than 0.01 THz (0.1 cm^{-1}~ 0.003 THz) and the method of attaining the value, which is via finding the maximum and minimum within the data files. This results in an error of ± 0.05 THz due to the broadness of the peaks. These are both random errors, however they are minimised by the spectrometer measuring a number of scans for each measurement (normally 256) and by monitoring the peak position on a number of different samples (experimental repeats).

Table 6.1. Displays the peak position and trough position for each of the heparin cations. The figure in brackets is a result that has also been seen within the data during repeats, but not regularly. The Zn^{2+} form is from experiments performed at Daresbury, spectra is not shown. The error on the data is ±0.05 THz.

Heparin	peak position (THz)	Trough position (THz)
Na^+	5.9	8.6 (8.9)
Mg^{2+}	6.2	8.4 (8.3)
K^+	5.7	8.4 (8.3)
Ca^{2+}	6.1	8.1 (9.1)
Cu^{2+}	6.0	8.4 (9.85)
Zn^{2+}	5.4	8.5

The absorption intensity differs due to thickness, and therefore cannot be considered as a valid method to distinguish between differing heparin cation derivatives, however the peak positions are different in differing heparin cation derivatives and has proven to be reproducible. The variation in intensity, observed in early experiments at Daresbury's SRS were expected to be due to an angular affect but as can be seen from the angular variation work performed at ANKA in figure 6.13 the angular variation of the heparin cation derivatives Na^+ and Ca^{2+} the variation in signal is only very small,

where as changes in thickness that were monitored at Daresbury's SRS show a greater change in signal.

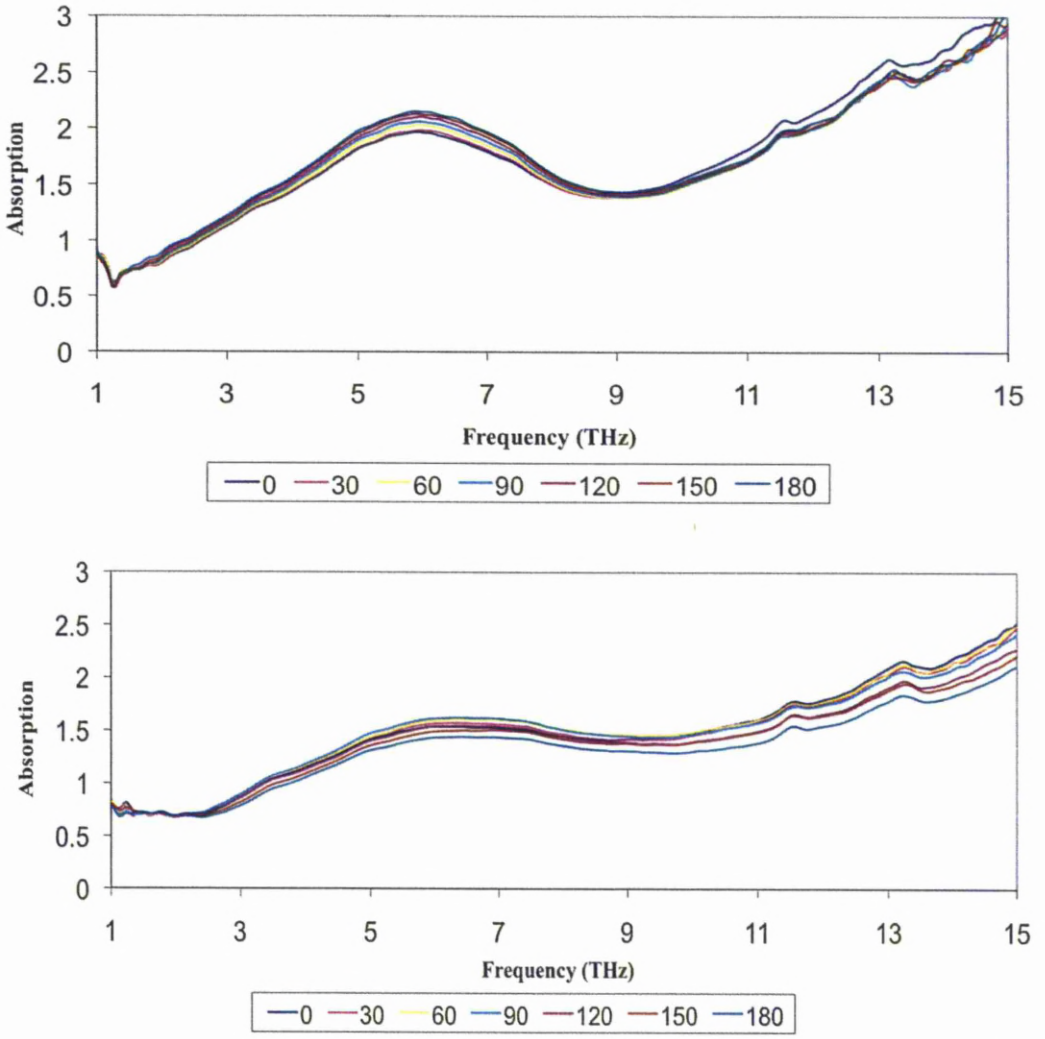

Figure 6.13. The angular dependant THz spectra of Na^+ heparin in the above graph and Ca^{2+} in the graph below. Values shown in legend are angles in degrees.

In an attempt to further understand the origin of the THz spectra, temperature dependant measurements were performed on the heparin derivative films using a custom made cryostat. The results for the Na^+ and Cu^{2+} film are shown in figure 6.14. There are no significant changes in the spectral profiles as the temperature falls but the overall intensity decreases smoothly with reducing temperatures. The spectra revert to the initial results upon warming up to room temperature showing that there are no permanent

changes in the heparin films during the cooling to liquid nitrogen temperatures. The temperature dependence of the THz spectra of the Cu^{2+} and Na^{+} forms probably arises from the thermal variation in the occupation of initial states and shows that the position of the dip in the spectrum is independent of temperature.

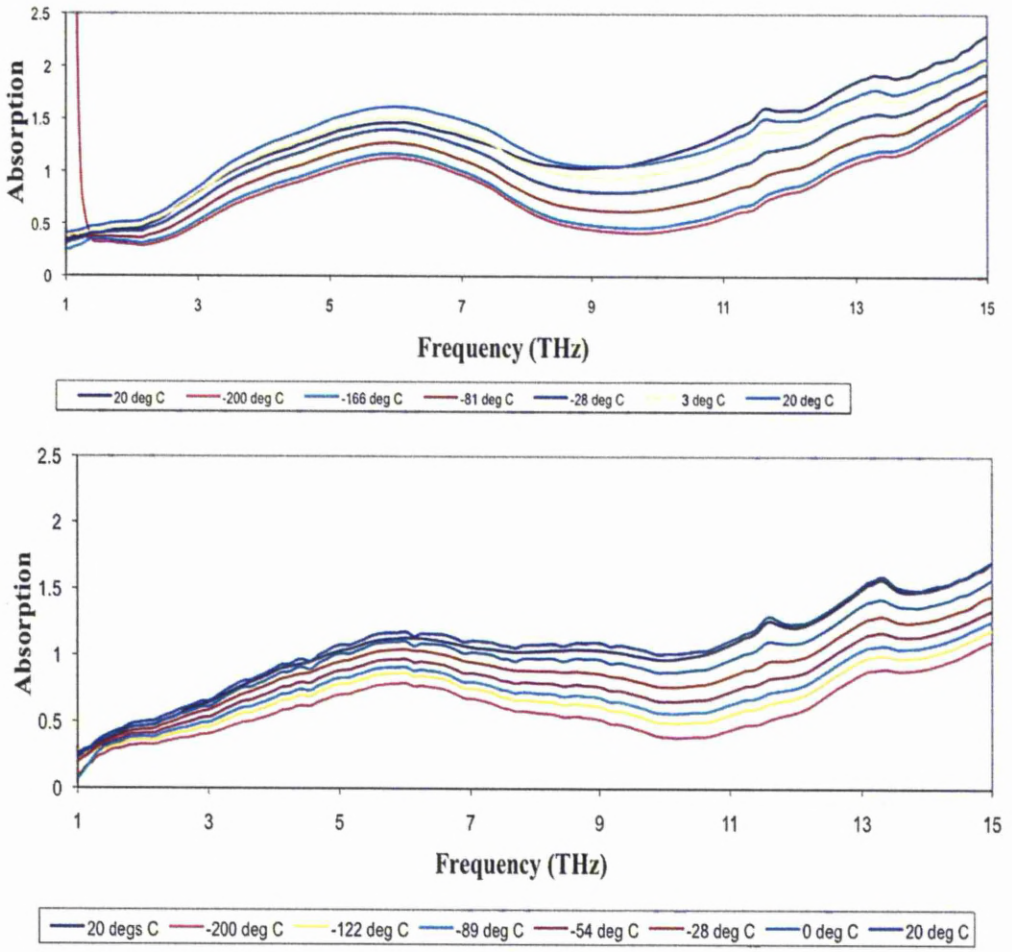

Figure 6.14. The THz spectra showing the temperature dependence of Na^{+} and Cu^{2+} heparin.

The drop in intensity seems directly related to the drop in temperature, and the fact that the initial room temperature result is the same as the final room temperature result (once the film has warmed to room temperature from the liquid nitrogen sample), shows that there is no permanent damage to the heparin film and therefore not a change of state or structure during the cooling.

6.5.2 Dextrans

To further understanding of the THz spectra of heparin derivatives previously discussed, it was decided to perform the experiments on Dextrans. Dextrans are glucose polymers which have been used clinically for over 50 years in a number of applications including plasma volume expanders, antithrombic agents and in drug delivery systems. They are structurally made up of α-1,6-glucosidic links with some degree of branching, that can vary from 0.5-60 % depending on their source. They can be produced by bacteria from sucrose or through specific chemical synthesis. The later results in a high level of customisation possible with branching and molecular weight [43]. The degree of branching and the molecular weight affect physiochemical properties of the polymer. Dextrans with branching that exceeds 43 % are insoluble in water, while most commercially available dextrans only contain 0.5 % branching resulting in them being highly water soluble. This makes them an ideal compound to use in comparison with the heparins, as they are both water soluble, they are both linear compounds with small degrees of branching and it is possible to compare similar molecular weights. However the major difference is the charge. Heparins, as mentioned previous are anionic and therefore have cation binding sites, while dextrans are neutral in charge. It is thought that by comparing the spectra of the heparins to the polymeric sugars it will provide insight into the origin of subtle spectral features.

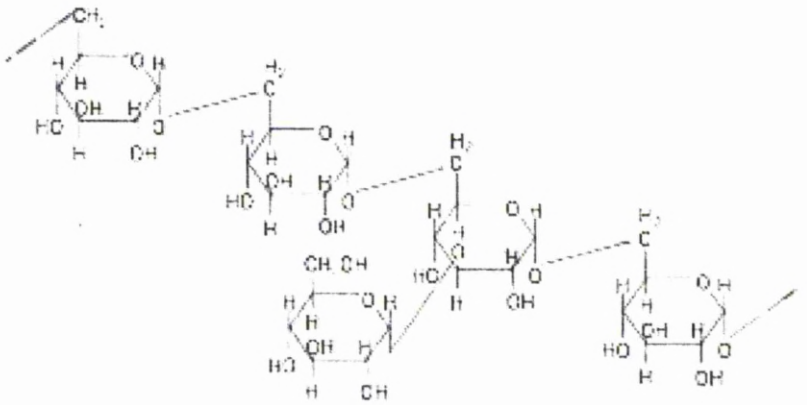

Figure 6.15. The structure of a dextran molecule fragment [44].

The dextrans used in this study were provided by Pharmocosmos in Denmark. They are a α-D-1,6-glucose-linked glucan with side chains 1-3 linked to the backbone

units of the dextran biopolymer. The degree of branching is roughly 5 % with most the branches being 1 or 2 glucose units long. Figure 6.15 shows the common structure of the dextrans [44]. The films were produced in the same manner as the heparins (100 mg/ml of dextran in water was dried to leave a film), however due to the inability to remove them from the glass slides, they were placed on a Polyethylene film (PE), which is almost 100 % transparent at these wavelengths, however a spectra of the PE was taken. A number of the heparins were also prepared on the PE film to ensure that there was no change in spectra, potentially from a change in orientation driven by the different substrate.

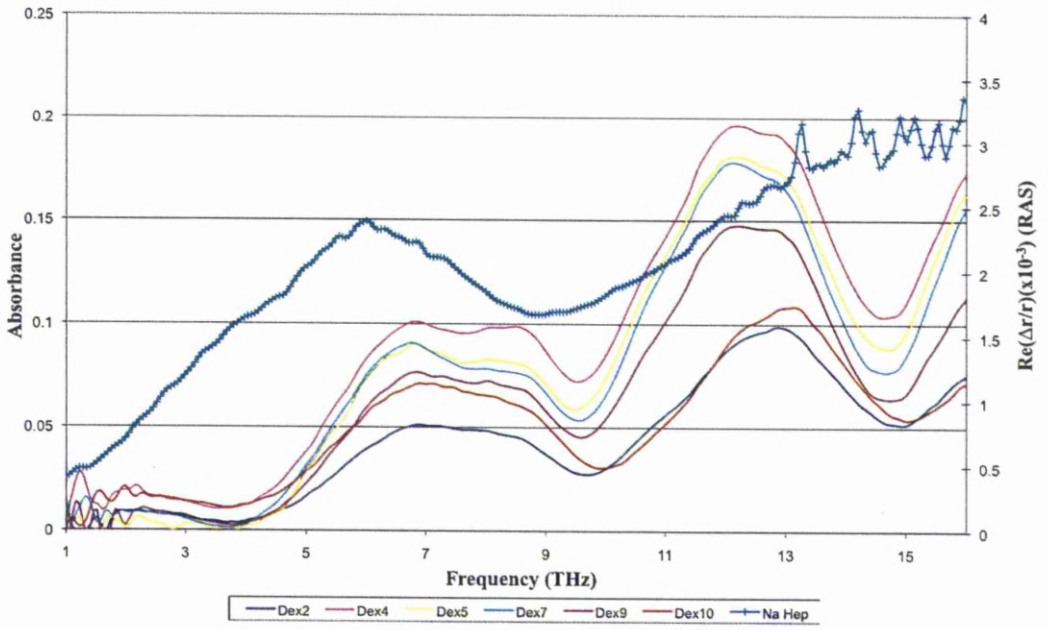

Figure 6.16. This shows the absorbance spectra of the 6 different dextrans and the Na^+ heparin on the PE film, note that the heparin has far greater absorbance and is on the right *y* axis.

Figure 6.16 shows the absorbance spectra of the 6 different dextrans tested and the Na^+ heparin all on PE films with the background, including the PE film, removed. The dextrans have a far smaller absorbance than the heparin sample (the *y* axis of which is on the right hand side of the chart) and there is a second feature in the dextran spectras. The dextrans vary in molecular weight and are described in table 6.2.

Table 6.2. The dextrans used for this study and their molecular weights.

Dextran	Molecular weight (Da)
2	4440
3	9890
5	43500
7	123600
9	276500
10	401300

The Na^+ heparin form in figure 6.16 shows the same features of those performed in the past after having been removed from a glass slide. This gives confidence to the methodology used for the dextran design. The peak and trough positions are very similar to those seen previously with a similar absorbance, with a transmission of between ~ 5-10 % through the sample. The dextrans however have a far lesser absorbance, between ~ 0-5 % in this spectra region, a transmission of between 95-100 %. An interesting result was that despite an increase in molecular weight and therefore chain length there is no change in position of the spectral features. The second feature observed in the dextrans is not seen in the heparins, and although there is a very small change in peak position it is likely to be due to thickness. As mentioned the peak and trough positions do not change, they are, position A (all positions shown on figure 6.17) at start of the increase of absorption at 4.4 THz, position B is the initial peak at 6.5 THz, the end of the first peak is position C at 8.3-8.8 THz, the dip, position D, at 9.7 THz, the start of the second peak, position E, at 12.1 THz and the position before the absorbance drops, position F, at 13 THz.

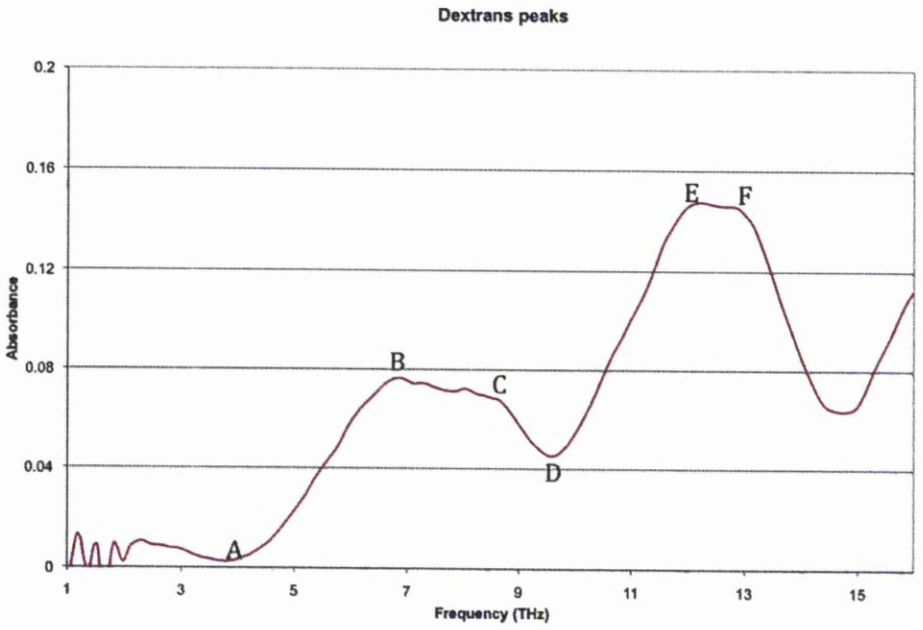

Figure 6.17. The spectra above shows dextran 9, and the positions of potential interest in the Dextrans.

Angular variation of the samples shows that there is little or no specific angular variation in this region, and the likely variation seen is due to a slight change in thickness as it was not possible to ensure the films were universally the same thickness.

6.6 Conclusion

Cation forms of heparin, as models of the naturally occurring cell surface polysaccharide heparan sulfate, have varying but complex structures that are difficult to probe using conventional techniques but, which are capable of altering dramatically their biological activities [9,11]. Novel techniques that are capable of identifying hitherto unexplored structural features and characteristics are therefore required. Here, the first THz spectra of these heparin derivatives, which are related to fundamental modes of molecular motion have been explored, in combination with several complementary methods, in the search for details of behavior in terms of their propensity to self-order and their fundamental properties. Results have shown that Na^{+}, Ca^{2+} and Mg^{2+} heparin cation derivatives show very strong anisotropy and form reproducible structures when in the

solid state. The features observed demonstrate that there is ordering in these structures. The other cation derivatives tested do not seem to possess this characteristic.

The RAS results on the films suggest that in the solid state, dipoles are aligned, but the linearly polarised THz spectra indicate that alignment of molecules is only weak in the solid state. It would be interesting to examine the properties in aqueous solution, which would provide a more realistic description of the natural situation on cell surfaces and in the ECM. Differences in molecular mobility for GAGs which are already constrained essentially in two-dimensions on the cell surface could have implications for their ability to search for binding partners and might suggest a more static role (and possibly, involving the alignment of dipoles). These polysaccharides may rely on charge and shape compatibity [7] rather than an ability to search large volumes of space to identify an exquisite specific binding site, such as might be the case for the more extended and flexible N-linked glycans and their binding partners, for example, lectins. Another possibility is that dipole alignment may drive movement, or binding of proteins, even though the molecules themselves are not strongly aligned.

Heparin shows vibrational modes in the THz region of the spectrum that reveal differences between different cation forms, each giving slightly different peak and trough positions. The possibility that this could be due to different occupancy of the density of states within the molecule has been tested by conducting temperature dependant studies. THz spectra exhibit broad peaks and troughs, which could be due to displacement of charges, causing destructive interference at particular frequencies. A full understanding of the shape of the curve is not yet available, but the dip in the spectra could be due to the LST effect, which involves the position and vibration of cations in a compound. However the similar early shape of the dextrans, which are uncharged would suggest that the THz spectra in the heparin samples was not due to the LST effect. There is also a second peak in the dextran spectra that is not observed in the heparins.

The experimental techniques employed here combine those able to examine order in aqueous solution, such as PLM and RAS, which is able to examine the environment of the cation dipoles, polarised FTIR, with which order in polysaccharide films can be investigated and THz spectroscopy, which can examine fundamental vibrational modes. Obviously, the physical situation in the ECM is not precisely

replicated during any of these experiments; the ECM is a complex environment with high concentrations of charged polysaccharides and proteins, as well as high levels of water. Some of the techniques, however, such as THz spectroscopy are not currently possible in the presence of large quantities of water and a compromise has to be made to access information regarding the properties of these materials which, otherwise, would remain unexplored. The high levels of water present in the ECM provide a medium in which thermal energy can be efficiently transferred throughout the environment and, presumably, the anionic polysaccharides of the ECM, evidently largely occupying initial modes in the solid state will be *more* flexible in the ECM but, still remain relatively immobile. These properties could have consequences in relation to protein binding and hence biochemical activities, and this initial investigation will provide the basis for further work in this area.

6.7 References

[1] D.G. Fernig, J.A. Smith and P.S. Rudland, *Journal of Cellular Physiology*. **142**, 108 (1990).

[2] A. Ori, M.C. Wilkinson and D.G. Fernig, *Frontiers in Biosciences*, **13**, 4309 (2008).

[3] A. Ori, M.C Wilkinson and D.G. Fernig, *J Biol Chem.* Mar 30. [Epub ahead of print] (2011)

[4] D. G. Fernig, J.A. Smith, P.S. Rudland, *J.Cell.Physiol.* **142**, 108 (1990).

[5] T.R. Rudd, D. Gaudesi, M.A Skidmore, M. Ferro, M. Guerrini, B. Mulloy, G. Torri and E.A.Yates *Analyst,* **136**, 1380 (2011).

[6] K.A. Uniewicz, A. Ori, R. Xu, Y. Ahmed, M.C. Wilkinson, D.G Fernig and E.A. Yates. *Anal Chem.* **82,** 3796 (2010)

[7] T.R. Rudd, K.A. Uniewicz, A. Ori, S.E. Guimond, M.A. Skidmore D. Gaudesi, R. Xu, J.E. Turnbull, M. Guerrini, G. Torri, G. Siligardi M.C. Wilkinson, D.G. Fernig, E.A. Yates, *Organic and Biomolecular Chemistry,* **8**, *5390 (2010).*

[8] S.E. Guimond, T.M. Puvirajesinghe, M.A. Skidmore, I. Kalus, T. Dierks, E.A. Yates, *J Biol Chem*, **284**, 25714 (2009).

[9] T.R. Rudd, S.E. Guimond, M.A. Skidmore, L. Duchesne, M. Guerrini, G. Torri, C. Cosentino, A. Brown, D.T. Clarke, G.E. Turnbull, D.G. Fernig and E.A. Yates, *Glycobiology* (2007) **17**, 983.

[10]. T.R Rudd, M.A Skidmore, S.E Guimond, C. Cosentino, L. Duchesne, G. Torri, D.G Fernig, R.M Lauder, M. Guerrini and E.A. Yates, *Glycobiology.* **19**, 52 (2009).

[11]. S.E. Guimond, T.R. Rudd, M.A. Skidmore, A. Ori, D. Gaudesi, C. Cosentino, M. Guerrini, R. Edge, D. Collison, E. McInnes, G. Torri, J.E. Turnbull, D.G Fernig and E.A Yates *Biochemistry*, **48**, 4772 (2009).

[12] D.L. Rabenstein, *Nat. Prod. Rep.* **19**, 312 (2002).

[13] T.R. Rudd, S.E. Guimond, M.A. Skidmore, L. Duchesne, M. Guerrini, G. Torri, C. Cosentino, A. Brown, D.T Clarke, J.E. Turnbull, D.G Fernig, E.A. and Yates, Glycobiology, **17**, 983 (2007).

[14] D. Stigter, *J. Phys.Chem.* **82**, 1603-1606 (1978).

[15] F. Chevalier, L. Ricardo, A. Jesús, M. Martin-Lomas and M. Nieto, *Carbohydrate Research, 339, 975 (2004).*

[16] D. Grant, W.F. Long, C.F. Moffat, and F.B. Williamson, *Biochem.J.* **282,** 601.

[17] N.R Rej, K.R. Holme and Arthur S. Perlin, *Carbohydrate Research.* 207, 143 (1990).

[18] T.R. Rudd, M.A. Skidmore, S.E. Guimond, M. Guerrini, C. Cosentino, R. Edge, A. Brown, D.T. Clarke, G. Torri, J.E. Turnbull, R.J. Nichols, D.G Fernig and E.A. Yates *Carbohydrate Research.* **343,** 2184 (2008).

[19] A.K. Powell, E.A. Yates, D.G. Fernig, and J.E. Turnbull, *Glycobiology.* **14,** 17 (2004).

[20]. R. Mezzenga, M. Grigorov, Z.D Zhang, C. Servais, L. Sagalowicz, A.L. romoscanu, V. Khanna and C. Meyer, *Langmuir.* **21,** 6165(2005).

[21]. S. Gaemers and A. Bax, *J. Am. Chem. Soc.* **123,** 12343 (2001).

[22]. A. Annila and P. Permi, *Concepts In Magnetic Resonance Part A.* **23,** 22 (2004).

[23] R.J. Linhardt and I. Capila, *Angew. Chem. Int. Ed.* **41,** 390 (2002).

[24] V.P. Panov and A. Ovsepyan, *Khimiko-Farmatsevteskii Zhurnal.* **13,** 72 (1979).

[25] E.A. Yates, A. Santini, F. Guerrini, M. Naggi, A. Torri and B. Casu, *Carbohydrate Research.* **294,** 15 (1996).

[26] D.J. Mahoney, J.D. Whittle, C.M. Milner, S.J Clarke, B. Mulloy, D. Buttle, G.C. Jones, J.A.Day, R.D. Short, *Anal. Biochem.* **330,** 123 (2004).

[27] J. Park and B. Chakrabarti, *Biochem. and Biophys. Res. Comm.* **78,** 604 (1977).

[28] E.M. Kristensen, H. Rensmo, R. Larsson, H. and Siegbahn, (2003) *Biomaterials* **24,** 4153.

[29] D. Grant, W. Long, C. Moffat and F. Williamson, *Biochem. J.* **283,** 243 (1992).

[30] M.C. Chung and N.F. Ellerton *Biopolymers.* **15,** 1409 (1976).

[31] J,V. Horssen, P. Wesseling, L. Heuval, R. Waal, and M.M. Verbeek, *The Lancet Neurolog.* **2,** 482. (2003).

[32] P. Weightman, G.J. Dolan, C.I. Smith, M.C. Cuquerella, N.J. Almond, T. Farrell, D.G. Fernig, C. Edwards and D.S. Martin D.S, *Phys. Rev. Lett.* **96,** 086102 (2006).

[33] B.G. Frederick, R.J. Cole, J.R. Power, C.C. Perry, Q. Chen, N.V. Richardson, P. Weightman, C. Verdozzi, D.R. Jennison, P.A. Schultz and M.P. Sears. *Phys. Rev. B.* **58**, 10883 (1998).

[34] B.G. Frederick, J.R. Power, R.J. Cole, C.C Perry, Chen, S. Haq, T.H. Bertrams, N.V. Richardson and P. Weightman. *Phys. Rev. Lett.* **80**, 4490 (1998).

[35] C.I. Smith, A. Bowfield, G.J Dolan, M.C. Cuquerella, C.P. Mansley, D.G. Fernig, C. Edwards, and P. Weightman, *J. Chem. Phys.* **130,** 044702 (2009).

[36] C.P. Mansley, C.I. Smith, A. Bowfield, D.G. Fernig, C. Edwards and P. Weightman, *J. Chem. Phys.* **132,** 214708 (2010)

[37] T. Globus, M. Bykhovskaia, D. Woolard and B. Gelmont. *Sub Journal of Physics D: Applied Physics.* **36**, 1341 (2003).

[38] A. Markelz, S. Whitmire, J. Hillebrecht and R. Birge. *Phys. Med. Biol.* **2**, 3797 (2002)

[39] L. Rabenstein, J.M. Robert, and S. Hari, *FEBS Letters.* **376**, 216 (1995).

[40] Z. Barnes, *Physik,* **75**, 723 (1932).

[41] T. Nakayama and E. Kaneshita, *Cond-mat matrl-sc.* **38**, 1(2011).

[42] C. Kittell, *Introduction to solid state physics, 4th Edition.* John Wiley, New York (1971).

[43] R. Mehvar, *J. Controlled Release.* **69**, 25 (2000).

[44] Pharmacosmos. (2007) Dextran Structure "online" (2007).
http://www.dextran.net/dextran-structure.html (7/02/2011).

Chapter 7. Conclusions

The conclusions drawn from this thesis are summarised and the possible direction of future work is also discussed

7.1 Summary of Findings

The key outcomes of the work covered in this thesis are outlined in the section below.

7.1.1 ALICE THz beam line

The commissioning of the THz beam line has proven to be quite difficult. A number of key issues have been highlighted; these mostly involve the direction in which the THz radiation propagates from the diamond window. THz radiation studies have provided a vital diagnostic tool for the accelerator scientists allowing them a further understanding of accelerator conditions. Beam profile studies clarified the suggestion, from theoretical data, that THz radiation may be being generated from more than one source position in the chicane. The new front end design that was commissioned in the first quarter of 2011 will allow a number of the issues discovered to be resolved and will allow for maximum THz radiation transport efficiency through to the TCF. The new front end has been instrumental in the successful transport of THz to the TCF where it was first measured in early April 2011.

7.1.2 Zebra Fish Embryo Study

Understanding the affect of THz radiation on tissues is vitally important as the development of THz radiation based security detectors increase. The Zebra fish embryo study was the first major study performed at the ALICE THz beam line and was chosen as there has been a lot of work performed previously on zebra fish embryos and they are a model system. The experiments were performed in the accelerator hall due to difficulties, at the time, of transporting the THz radiation to the TCF. This resulted in a number of subsidiary studies to ensure any effects observed in the zebra fish embryos was due to the THz radiation rather than other factors. Although the results were not conclusive, the study has resulted in a number of changes to the experimental method. At this point it is not possible to say with any certainty whether THz affect the development of Zebra fish embryos, however some of the experiments did suggest that this was taking place. Results also suggested the importance of the embryos entering an arrested state. In this arrested state the embryo basically shuts down due to a loss of favourable conditions. This is not a terminal condition and the cells can recover, however during this time any damage done to the embryo by the THz radiation would

not be fixed between pulses. Experiments must be designed to test this hypothesis further. It is also important that future studies allow more accurate analysis of any changes to be performed, including monitoring changes to protein synthesis, which have not been possible so far. An important experiment testing the affect of the THz radiation at ALICE on heating of samples was performed and proved there was no measurable change. This is very positive as it clarifies that experiments on ALICE, due to the timing structure, will be able to probe the effects of THz radiation without worry of any thermal effects.

7.1.3 Heparin Study

The conformational stucture of heparin cation derivatives have been monitored using a number of complementary spectroscopic techniques to understand if they have a propensity to self-order. Na^{+}, Cu^{2+} and Mg^{2+} cation forms show a strong anisotropy forming reproducible structures in the solid state. However the other forms tested showed little or no anisotropy. The results from the THz studies reveal differences between cation forms, with each having the same general shape, but with the maximum and minimum of the peaks and troughs at different frequencies. It is thought the general spectral shape would be due to the occupancy of the Density of States with slight changes within cation forms. This was tested with a temperature study where the intensity of absorption decreasing when temperature decreased.

A reason for the overall shape of the THz heparin spectra is not yet known, however it is considered it could be due to the the Umklapp process or the Lyddane-Sachs-Teller (LST) effect. However the similar appearance in the dextrans which are uncharged (though they have weaker signals) have a similar shape, with two peaks with the second at a higher frequency. This would rule out the shape of the spectra being due to the LST effect. There is no angular effect in the THz spectra.

These properties could have great consequences in the relation to protein binding and therefore biochemical activity. Both RAS and THz spectroscopy show great potential in this region, however further work is required.

7.2 Future Work

The majority of the work performed in this thesis involves the THz beam line at ALICE. The THz beam line has successfully transported THz radiation from the diamond window (exit of the ALICE accelerator) to the diagnostics room and TCF. Further work is required to understand the accelerator conditions and generate the maximum THz radiation signal close to the diamond window, while maintaining a beam profile that will allow a successful transportation of the radiation to the TCF. The new front end design discussed in this thesis and commissioned in the first quarter of 2011 will allow this to be performed without the need to enter through limited access. Once this is achieved a the spectral properties should be measured in the Martin Puplett spectrometer in the diagnostics room, and the dependence on accelerator conditions on this spectrum should be experimentally calculated. Once this is completed a number of further experiments can be performed to test the Frohlich hypothesis and confirm whether THz modes play a crucial role in biological organisation.

The cell studies performed so far should be repeated in the TCF allowing closer and more explorative analysis to take place. The development of the experimental hutch located directly below the TCF should allow a number of different experiments to be performed. This will allow potential THz pump photon probe experiments to be performed on systems already characterised to monitor any changes caused by THz radiation. The Liverpool group have, through a collaboration with Martyn Chamberlain of Durham University, sourced a microfluidic cell which will allow a number of THz exposure experiments of biological molecules in liquids. This cell negates the "water problem" of THz experiments by creating a very small volume that still allows molecules to align normally, while keeping H-bonding absorbance to a minimum. This will allow the effects of THz radiation on a number of biological systems to be performed including protein folding experiments, mentioned in the introduction section.

The TCF and experimental hutch at ALICE will allow the Liverpool group to work at the forefront of THz research into biological systems and is likely to produce research that will have massive global interest.

7.3 Publications

7.3.1 ALICE

- "The terahertz beamline and tissue culture facility on the ALICE accelerator at the Daresbury laboratory" P. Weightman, G. Holder, A. Schofield, R.L. Williams, P. Harrison, A. Bowfield and M. Surman. Vestnick Novosibirsk State University, Ser. Physics **5** 28-31 (2010) Invited Plenary Lecture: International Symposium: Terahertz Radiation: Generation and Application (Novosibirsk, Russia, July 2010)
- "Progress on the commissioning of ALICE, the energy recovery linac-based light source at Daresbury Laboratory" J. Alexander, P. Atkinson, R. Bate, C. Beard, N. Bliss, M. Bowler, I. Burrows, R. Buckley, S. Buckley, J. Clarke, P. Corlett, G. Cox, P. Dickenson, M. Dufau, D. Dunning, B. Fell, A. Gallagher, K. Gleave, P. Goudket, S. Griffiths, A. Goulden, J. Herbert, C. Hill, S. Hill, P. Hindley, F. Jackson, S. Jamison, J. Jones, L. Jones, A. Kalinin, N. Marks, B. Martlew, P. Mc Intosh, J. Mc Kenzie, K. Middleman, B. Militsyn, A. Moss, I. Mullacrane, B. Muratori, A. Oates, J. Orrett, P. Phillips, M. Poole, S. Pattlwar, G. Priebe, P. Quinn, R. Rotheroe, Y. Saveliev, D. Scott, B. Shepherd, R. Smith, S. Smith, J. Strachan, G. Stokes, M. Surman, N. Thompson, B. Todd, P. Warburton, T. Weston, A. Wheelhouse, P. Williams, C. White, G. Hirst, P. Huggrad, W. Flavell, E. Seddon, P. Weightman, P. Harrison, D. Holder, G. Holder, K. Harada, G. Neil, K. Jordan, F. Hannon, C. Hernandez, F. Gabriel, P. vom Stein, C. Gerth. IEEE Particle Accelerator Conference (2009).
- "Recent developments on ALICE (Accelerators and Lasers in Combined Ecperiments) at Daresbury Laboratory" Y. Saveliev, B. Bate, R. Buckley, S. Buckley, J. Clarke, P. Corlett, D. Dunning, A. Goulden, S. Hill, F. Jackson, S. Jamison, J. Jones, L. Jones, J. Orrett, D. Laundy, S. Leonard, P. McIntosh, J. Mckenzie, K. Middleman, B. Militsyn, A. Moss, B. Muratori, S. Pattalwar, J. Phillips, G. Priebe, D. Scott, E. Seddon, B. Shepherd, S. Smith, M. Surman, N. Thompson, A. Wheelhouse, P. Williams (STFC, Daresbury Laboratory, UK), P. Harrison, D. Holder, G. Holder, A. Schofield, P. Weightman, R. Williams (The

University of Liverpool, UK), T. Powers (JLab, USA). TUPE096 Proceedings of IPAC'10, Kyoto, Japan.

- "The THz beamline on ALICE at Daresbury – current status and application to Biological systems" G. Holder. Presentation at EuroFEL 2010.

7.3.2 Heparin

- "Micro- and macroscopic characteristics of polysaccharide components of the extracellular matrix probed using complementary optical and spectroscopic techniques." G. Holder, A. Bowfield, M. Surman, M. Suepfle, D. Moss, E.A. Yates, T.R. Rudd, D.G. Fernig and P. Weightman. (in preparation)